Investigation of the stress corrosion cracking resistance of SAF2205 and AISI304 weldments for the marine environment application

Student name: M. Matjee

Student number: MTJMAP003

Supervisor: Prof. R. Knutsen

PLAGIARISM DECLARATION

I understand what plagiarism is and the consequences of such acts. I declare that the content covered in this thesis is my own work. It is not copied from any other sources. The inspiration of some topics covered in the thesis is drawn from other sources and they are referenced in the text and the bibliography accordingly. The work covered in this thesis is submitted towards attaining a Master's degree in Materials Science at the University of Cape Town, Faculty of Engineering and the Built Environment. The work covered was not used to attain any other qualification from any other universities.

Signed by candidate

Signature

ABSTRACT

Stainless steels are used for many industrial applications because of their strength and fabrication characteristics. Stainless steel grades of SAF2205 and AISI304 can readily meet a wide range of design criteria of service life, maintenance, load and corrosion resistance. The SAF2205 and AISI304 are Fe-Ni-Cr alloys, whereby SAF2205 consists of austenite-γ and ferrite-δ microstructure and AISI304 is monophasic comprising of an austenite-γ microstructure. Welding is frequently used in the manufacturing process of stainless steel products and it alters the base metal microstructure by introducing secondary phases or causing sensitisation in the Heat Affected Zones (HAZ) when it is not carried out correctly. The synergistic effects of the chloride environment and residual stress has a potential to increase susceptibility of the weldments due to precipitation of the deleterious intermetallic phases, which can be worsened by a Post Weld Heat Treatment (PWHT). An investigation to determine SAF2205 and AISI304 weldment susceptibility to SCC and intergranular attack for marine environment application has been conducted. The purpose of the investigation is to characterise the microstructure of a PWHT of SAF2205 and AISI304 weldments by comparing the welded material in the conditions of as-weld, as-received and PWHT. The tested materials will be evaluated for their corrosion performance specifically at the weldments when they are exposed to the marine environment. Thin rectangular specimens were sectioned such that the weldments are maintained at the centreline, followed by PWHT at 500℃ for 3 hours and 800℃ for 2 hours and then air cooled. The PWHT was completed to exaggerate the intermetallic formation in SAF2205 and sensitisation of AISI304 HAZ. Tensile tests were performed to determine the elastic limit of SAF2205 and ASIS304, so that specimens are fixed in the holder without plastic deforming, but they maintain a yield stress level at the bend specimen apex or weld just below the yield stress. The mounted specimens were exposed to Cyclic Corrosion Testing (CCT-1) in a salt chamber. The exposure conditions included application of 5wt.%NaCl fog at 35℃ for 4 hours, 100% humidity at 50℃ for 2 hours and drying at 60℃ for 2 hours and at 40℃ for 30 minutes. After 10 months of corrosion exposure, AISI304 specimens showed corrosion pits and rust at the apex of the bend specimens whereas SAF2205 specimens were defect free, and thus unaffected by the testing conditions. Additionally, the Strauss test was completed to determine the intergranular attack susceptibility for the tested material, at the Fusion Zone (FZ), BM (Base Material) and HAZ at the conditions of as-weld and PWHT at 800℃ for 2 hours and 500℃ for 3 hours. The SAF2205 specimen, PWHT at 800℃ for 2 hours, cracked during the material qualification bend test, particularly at the HAZ and FZ. These regions were further analysed using Scanning Electron Microscopy (SEM: BSE and EDS). The EDS analysis on the HAZ revealed the presence of Mo-rich precipitates of chi (χ)-phase and Cr-rich precipitates of sigma (σ)-phase at the grain boundaries and triple points growing into the ferrite-δ, making these regions to become brittle. The FZ revealed brittle sigma (σ)-phase at the grain boundaries with no chi (χ)-phase detected. The AISI304 exposed to similar conditions did not suffer intergranular attack but demonstrated full ductility during the bend test.

ACKNOWLEDGEMENTS

I would like to express my gratitude to my academic mentor, Prof. Robert Knutsen, for guidance and having faith in me during challenging times. I would also like to extend my gratitude to the following:

Dr Richard Curry for the teachings on the know-how towards mechanical analysis and safety operations of the machines.
My Industrial mentor, Kobus Smit, for imparting the industry knowledge towards my research studies.

My employer, Eskom, for giving me the opportunity to complete my research studies towards obtaining my master's degree in materials science through the Eskom Power Plant Engineering Institute (EPPEI) programme.

Centre for Materials Engineering (CME) personnel, Mrs Penny Louw and Miss Soraya Von Willingh, for their support throughout my academic journey.

Centre for imaging and analysis (EMU) staff, specifically Mrs Miranda Waldron and Mrs Natsheeta Hanief for their assistance in SEM sample coating and operation of the Electron Microscope Unit.

University of Cape Town (UCT)-Mechanical engineering workshop personnel, Mr Pierre Smit and Mr Heidrich Christians, for their patience and working with me tirelessly until the work was done.

Lastly, I want to extend my special thank you to my daughter Paledi Matjee and my life partner, Hans-Gerd Behet, for the love and support that they have shown me. This also extends to my amazing family and friends for their continued support and encouragement.

TABLE OF CONTENTS

LIST OF ACRONYMS AND ABBREVIATIONS

Acronyms

ASTM International – Formerly known as American Society for Testing and Materials

AISI – American Iron and Steel Institute

ASCC – Atmospheric Stress Corrosion Cracking

BM – Base Material

BCC – Body Centred Cubic Structure

BCT – Body Centered Tetragonal structure

CCT-1 – Cyclic Corrosion Testing

CME – Centre for Materials Engineering

CSCC – Chloride Stress Corrosion Cracking

DC – Direct Current

DSS – Duplex Stainless Steel

ECC – Equivalent Chromium Content

EDS/EDX – Energy Dispersive X-ray Spectroscopy

BSE –Backscattered Electron

FCC – Face Centred Cubic Structure

FOV – Field of View

FL – Fusion Line

FZ – Fusion Zone

FCAW – Flux Cored Arc Welding

GCP – Geometrically Close Packed

GTAW – Gas Tungsten Arc Welding

GMAW – Gas Metal Arc Welding

HAZ – Heat affected Zone

ICDD – International Centre for Diffraction Data

IGC – Intergranular Corrosion

IGSCC – Intergranular Stress Corrosion Cracking

MDS – Material Data Sheet

MTC – Material Test Certificate

OEM – Original Equipment Manufacturer

PAW – Plasma Arc Welding

PWHT – Post Weld Heat Treatment

PVC – Polyvinyl Chloride

PQR – Procedure Qualification Records

REDOX – Reduction Oxidation Reaction

RO – Reverse Osmosis unit

SEM – Scanning Electron Microscopy

SAF2205 – Sandvik SAF2205/ ferritic-austenitic

SS – Stainless Steel

SMAW – Shielded Metal Arc Welding

SAW – Submerged Arc Welding

CSCC – Chloride Stress Corrosion Cracking

TCP – Topologically Close Packed

TDS – Technical Data Sheet

TIG – Tungsten Inert Gas

TTT – Time-Temperature- Transformation diagram

UTS – Ultimate Tensile Strength

UCT – University of Cape Town

VM – Virgin Material

WPS – Welding Procedure Specifications

YS – Yield strength

Chemical symbols

Cu – Cupper chips

$CuSO_4$ – Copper (II) sulphate

C – Carbon

Cr – Chromium

$Cl^-_{(aq)}$ – Ions of chloride in aqueous solution

$Cr_{23}C_6$ – Chromium carbides

Cr_2O_3 – Chromium (III) oxide

$Cr(OH)_3$ – Chromium (III) hydroxide

Cr_2N/CrN – Chromium nitrides

H^+ – Hydrogen ions

HCl – Hydrochloric acid

H_2SO_4 – Sulphuric acid

HNO_3 – Nitric acid

Mn – Manganese

Mo – Molybdenum

N – Nitrogen

$NaCl_{(s)}$ – Sodium chloride salt fine granules

NbC – Niobium carbide

$Na^+_{(aq)}$ – Ions of sodium in aqueous solution

NaOH – Sodium hydroxide

$NaCl_{(aq)}$ – Sodium chloride in aqueous solution

Nb – Niobium

Ni – Nickel

O_2 – Oxygen

Pt – Platinum metal

SiC – Silicon carbide

Ta – Tantalum

TaC – Tantalum carbide

Ti – Titanium

TiC – Titanium carbide

Abbreviations

Ave. – Average

Std. Dev. – Standard deviation

%EL – Percentage elongation

%RA – Percentage Reduction of/in Area

Symbols

E – Modulus of elasticity

L_o – Original length

ε_y – Yield strain

σ_y – Yield stress

T – Thickness of specimen

y – Maximum deflection (between outer supports)

H – Sample holder span

θ – Maximum slope of the specimen when loaded to the holder

δ – Ferritic phase

γ – Austenitic phase

γ_2 – Secondary austenite phase

σ – Sigma phase

χ – Chi phase

η – Laves phase

μ – Mu

γ’ – Gamma prime

γ’’ – Double prime

α' – Alpha prime

τ – Tau phase

LIST OF FIGURES

LIST OF TABLES

CHAPTER 1 INTRODUCTION

Stainless steels are often the material of choice when designing and manufacturing tanks for storing neutral and mildly aggressive liquids, where tanks themselves are exposed to harsh conditions. Large capacity storage tanks are fabricated by means of multiple weldments to join the pre-formed stainless steel sheets or parts to produce tanks of cylindrical design. Consequently, the choice of stainless steel and the welding technique must not only provide adequate corrosion resistance for the application, but also account for internal and external environmental conditions. Stainless steel of choice need to consist of properties such as the following: weldability, excellent mechanical properties viz. formability, machinability, tensile strength and exceptional corrosion resistance, for the asset to maintain its integrity especially at the weld joints during its lifespan, without deteriorating or having premature defects or catastrophic failures that can be very costly or even lead to fatality. Stainless steel grades of AISI304 and SAF2205 are commonly used as they have good metallurgical properties viz. equiaxed grain size, alloying elements and both grades can be welded and formed at ease while maintaining excellent mechanical and corrosion properties. Although the studied stainless steel grades have good welding properties, caution is necessary when conducting welding operations as it exposes the material to high thermal cycles that could affect the properties of the associated HAZ negatively. Manufacturing of the tanks by means of fusion welding can cause the development of the substantial residual stresses and the precipitation of deleterious intermetallic phases associated with welding operations. Since it is not practical in most instances when fabricating using these materials to conduct post-weld heat treatment (PWHT) to reduce or even to eliminate the residual stress, the presence of these potential dangers needs to be factored into the component life cycle management. Hence, enough insight into the influence of welding and the associated effects of residual stress of the studied materials' susceptibility to SCC is necessary.

1.1 Rationale for the study

Components such as storage tanks and pipelines are constructed to store and convey fluids for the use in various industries that are located near coastal regions. Several factors can negatively affect the integrity of tanks and pipes, depending on the marine environmental influence on the exposed surfaces. Components such as tanks, vessels, canisters and pipelines. when subjected to marine environment, whereby condensation of fog and humidity are inevitable, can lead to excessive chloride build-up on the component surfaces if left unnoticed. The saturated chloride ions (Cl^-) condensate can interact with iron ions (Fe^{2+}) within the steel structure by means of electrochemical reaction producing corrosion products that will eventually weaken the material. While stainless steels of grades, AISI304 and SAF2205 may have enough resistance to atmospheric corrosion attack, the synergistic effects of the chloride environment and residual stress might increase the susceptibility of the weldments (Fusion Zone) and the associated heat affected zones (HAZ) to Stress Corrosion Cracking (SCC). It is possible in these circumstances that either of these stainless steel grades will outclass each other in providing the desired corrosion properties. Thus, it is imperative to understand the performance of these engineering materials used to construct components such as tanks, pipes and canisters used in industries located in or near coastal environments e.g. power generation plants, petrochemical plants and food industries. Austenitic stainless steels represent the largest group of stainless steels in use and Duplex stainless steels are used to an increasing extent in the environment that are discussed.

1.2 Research Aim

The aim of the research study is to investigate the resistance of SAF2205 and AISI304 stainless steels grades to Stress Corrosion Cracking (SCC) at the weldment regions of Fusion Zone (FZ), Heat Affected Zone (HAZ) and Base Material (BM) in the conditions of as-received, as-weld and Post Weld Heat Treated (PWHT).

1.3 Research objectives

1.3.1 To analyse and compare the SCC susceptibility of AISI304 and SAF2205 grades under laboratory conditions that simulate the marine environment.

1.3.2 To evaluate the susceptibility to intergranular attack of AISI304 and SAF2205 stainless steel grades at the weld regions (FZ, HAZ and BM) that are in the following conditions: as-received, as-weld and post weld heat treated.

1.3.3 To characterise the weldment regions of the studied materials (AISI304 and SAF2205) grades by analysing the evolved microstructure and elemental compositions in the as-weld and PWHT conditions.

1.3.4 To develop the heat treatment to purposefully introduce detrimental microstructures in the weldment of SAF2205 and AISI304 to exacerbate susceptibility to corrosion.

1.4 Research questions

1.4.1 Which of the investigated stainless steel grades of SAF2205 and AISI304 has greater resistance to stress corrosion cracking when exposed to laboratory accelerated corrosion?

1.4.2 How do the stainless steel grades of SAF2205 and AISI304 compare when exposed to intergranular attack laboratory conditions in the tested regions of FZ, HAZ and BM?

1.4.3 Which heat treatment can cause the investigated materials (SAF2205 and AISI304) to develop microstructure that are not corrosion resistance?

CHAPTER 2 : LITERATURE REVIEW

2.1 Background

To ensure safety and uninterrupted operation in various plants namely power plants, chemical plants such as those of food processing, refineries/ petrochemical plants and many other engineering applications, the availability and reliability of components, equipments and the structural integrity of pipelines, tanks and supports are of paramount importance. These components, tanks, pipes etc. are joined to form safety systems or else they integrate with safety functions of the plant that when they become unexpectedly defective, they can lead to catastrophic failures or consequences. Additionally, the components such as tanks, silos and canisters are designed to contain products, waste and raw materials fed or extracted from the plant for the life of the plant. It is vital to understand the effects of the material used to construct the important components, especially the influence of the environment that they are meant to operate in, relative to their corrosion properties at prolonged operational durations. The understanding of the material used for the fabrication and its behaviour in sour conditions will benefit in planning their maintenance routine, that there are no operational disruptions and or unplanned maintenance on the affected components.

The stainless steel grades of SAF2205 and AISI304 have been recognised as suitable for fabrication of components operating in harsh corrosive conditions because of their good corrosion resistance and excellent mechanical properties with good weldability and formability. However, there are some shortfalls associated with manufacturing of the components by welding of these steels due to excessive thermal cycles exposure introduced by the weld metal. Table 1 provides a summary underlining the benefits and shortfalls of the investigated materials suggesting that they not meet the design constrains particularly when they are welded to be utilised in various applications near coastal regions. Consequently, there was a need to study the evolution of these welded stainless steels and the effect of the extended exposure to the marine conditions regarding susceptibility to the Stress Corrosion Cracking (SCC). The current study is also intended to validate the material that can withstand the harsh environment without premature failures, which can be catastrophic and very costly when left undetected. Various studies have been completed in the field of Atmospheric Stress Corrosion Cracking (ASCC), and the present research study will incorporate the previous work done such as the available theories, experimental techniques and procedures or standards completed on SAF2205 and AISI304 relevant to the research matter to assess their performance under the controlled exposure conditions.

The scope of this research study will be limited to SCC and intergranular attack effect of the welded joint or Fusion Zone (FZ), the adjacent Heat affected Zone (HAZ) and the Base Metal (BM) of the investigated steels, that are in the as-weld, as-received and Post Weld Heat Treatment (PWHT) state.

The AISI304 grade are used extensively in corrosive environments due to their resistance to corrosion owing to the material's passivation ability to form chromium (III) oxide (Cr_2O_3) in the presence of oxygen (O_2). These add to the stainless steel's attractive mechanical properties such as ductility and toughness. A major drawback of these steels is their susceptibility to chloride induced SCC. The AISI304 grades retains its aesthetic appearance in most atmospheres, except those within 20km of the coastline or in severely polluted environments.

With the appropriate dose of the alloying elements and feasible thermo-mechanical processing, it is possible to produce stainless steels that have dual phase structure consisting of austenite-γ and ferrite-δ microstructure. The duplex stainless steels (SAF2205) offer certain advantages over single phase grades, including higher yield strengths and greater resistance to SCC under specific operating conditions. The stainless steel of SAF2205 grade is second generation duplex stainless steel that are nitrogen (N) alloyed with high chromium (Cr) and low nickel (Ni) contents. These stainless steels have increased mechanical properties, with the yield strength double that of austenitic grades. As a result it is widely used in the marine and other high chloride environments competing with the austenitic grades. The limitations and benefits of the studied stainless steels of SAF2205 and AISI304 grades are highlighted in Table 1 below [1].

Table 1: Limitations and benefits of stainless steel grades of AISI304 and SAF2205.

Type	**Grade**	**Benefits**	**Limitations**
Austenitic grades	AISI304	• Mostly available • Good general corrosion resistance • Good toughness • Excellence weldability and formability	• Work hardening can limit machinability and formability. • Limited resistance to SCC
Type	**Grade**	**Benefits**	**Limitations**

Duplex grades	SAF2205	• Good SCC resistance • Good mechanical strength in annealed condition	• Application temperature range more restricted than austenitic. • More expensive and less widely available

2.2 Duplex stainless steel (SAF2205)

Duplex stainless steels consist of dual phases of ferrite-δ and austenite-γ microstructure, having a phase balance of approximately 50% ferrite-δ and 50% austenite-γ (%volume). These steels are intermediate grades between ferritic and austenitic stainless steel incorporating both steel properties, shown by the Schaeffler Delong diagram (Figure 2-1); hence it is also referred to as duplex stainless steel. The duplex microstructure benefit from the properties of austenitic and ferritic microstructures, thus when it is compared to ferritic steel grades it exhibits adequate ferromagnetic behaviour with enough thermal conductivity and possesses lower thermal expansion coefficients than the austenitic steel grades. The material exceeds the ductility and toughness of ferritic grades although they are not as tough as austenitic grades. The duplex structure has good ductility and exhibit strong work hardening properties.

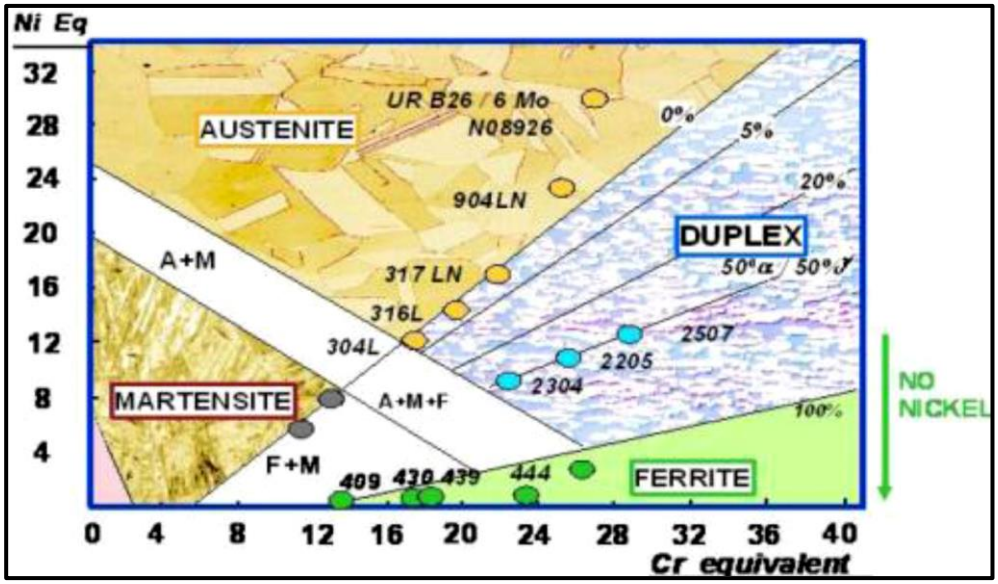

Figure 2-1: Schaeffler Delong diagram – Cr and Ni equivalent compositions for ferrite, austenite, duplex, and martensitic stainless steels **[2]**.

The SAF2205 grade contains nominal elemental compositions of 22wt.%Cr, 5wt.%Ni and 3wt.%Mo, regarded as standard duplex stainless steel which has very good general and pitting corrosion resistance. The SAF2205 grade is also considered as more suitable for application in the most aggressive marine environments except for seawater immersion [3].

2.2.1 Phase ratio of austenite/ferrite (γ/δ) and their effects on duplex stainless steel properties

As cited in the previous sections, the duplex stainless steels are mainly characterized by the duplex-phase structure with approximately equal proportions of austenite-γ (Face Centred Cubic –FCC) and ferrite-δ (Body Centred Cubic–BCC). The volume fractions (γ/δ) can range from 60/40% to 40/60%. The (γ/δ) phase ratio can vary between 40% and 60% or even between 30% and 70% interchangeably. The balance ratio of the two phases (γ/δ) plays a significant role in defining the properties of duplex structure of stainless steel even though the phase can vary with temperature and compositions, restricting its use to a maximum temperature of 300℃ and minimum temperature of -50℃. At high temperature the dual structure becomes more ferritic-δ, with less Ni-element and more Cr-element equivalents [4]. At elevated temperatures this structure maintains considerably good toughness, high strength and appreciable ductility [5]. The duplex grades are not hardenable by heat treatment but are stronger than either ferritic or austenitic stainless steel in the annealed condition, having almost double the yield strength of austenitic grades. Like the ferritic stainless steels, they are ferromagnetic, but they have good formability and weldability of austenitic stainless steel, even though higher forces are required for forming due to the strength the material possesses. Duplex stainless steels have lower thermal expansion and higher heat conductivity than austenitic stainless steels [6].

2.2.1.1 The ferrite (δ)-phase in duplex stainless steel

The presence of ferrite (δ)-phase in the duplex stainless steel structure is vital, as it contributes to the steels' good mechanical properties as well as corrosion properties and weldability. The ferrite content of approximately 40% to 65% is ideal to promote or maintain the attractive properties of austenite-ferrite structure [7]. The ferrite (δ)-phase is susceptible to severe embrittlement when exposed at 475 °C. This aging embrittlement is comparable with that of the ferritic stainless steels, and it poses a risk of the material deteriorating prematurely. Duplex stainless steel with more ferrite-δ content could cause the steel to perform like ferritic stainless steels. Consequently, the ferrite-δ limits should be held within a reasonable range so the duplex stainless steel properties can be maintained. Duplex stainless steel mechanical properties at low temperature are essential; thus, the

ferrite-δ content should be controlled. Ferrite (δ)-phase that is more than 60% volume can lead to noticeable decline in the ductility and reduced pitting resistance within the duplex stainless steel. In addition the ferrite-δ levels that are lower than 35% may also have a negative effect on material's ductile behaviour, and reduced SCC resistance because of the solidification mode that causes segregation [8].

2.2.1.2 The austenite (γ)-phase in duplex stainless steel

The presence of the austenite (γ)-phase enhances ductility. During solidification, duplex stainless steel solidifies completely as ferrite-δ and undergoes solid state phase transformation into austenite-γ. This is a reversable process and as a result, any large increase in temperature (>1000℃) lead to an increase in ferrite-δ and also a reduction in the partitioning of substitutional elements between phase, which can be the case during welding activities [8]. The coexistence of the two phases of austenite-γ and ferrite-δ in the duplex structure not only provides an improved intergranular corrosion resistance, but it also improves SCC resistance when it is compared to fully austenitic stainless steels. The degree to which any of these alloys is resistance to any form of corrosion or stress corrosion depends its upon composition and microstructure [7].

2.2.2 Alloying elements of duplex stainless steels: SAF2205

Duplex stainless steels grades are often identified by four digits: the first two digits denote the weight percent of chromium (wt.%Cr), and the second two digits represent the weight percent of nickel (wt.%Ni). In the case of SAF2205 grades, the first two digits denotes that there is 22wt.%Cr, with the last two digits indicating that there is 5wt.%Ni present in the metal alloy [9]. The chemical composition of the alloying elements has a major influence on the steel's metallurgical structure, mechanical properties and corrosion resistance. In duplex grades, the interaction of the major alloying elements such as chromium (Cr), molybdenum (Mo), nitrogen (N) and nickel (Ni) are said to be complex but beneficial [2]. Table 2 below highlight the chemical compositions of typical alloying elements in SAF2205 grades.

Table 2: Elemental compositions for duplex stainless steels (SAF2205 grade) **[10]**

Duplex stainless steel – SAF2205 grade						
UNS no.	**Carbon: C (wt.%C)**	**Chromium: Cr (wt.%Cr)**	**Nickel: Ni (wt.%Ni)**	**Molybdenum: Mo (wt.%Mo)**	**Nitrogen: N (wt.%N)**	**Manganese: Mn (wt.%Mn)**
SAF2205	<0.03	22.0-23.0	4.5-6.5	3.0-3.5	0.14-0.20	1.5

The Cr-element is a ferrite stabiliser, meaning the ferrite-δ fraction within the duplex structure will increase with an increase in Cr-content. The increase in the Cr-element within the metal alloy encourages corrosion resistance by forming a Cr_2O_3 layer on the steel surface when there is O_2 present.

The presence of Ni-element is of importance within this metal alloy as it delays the formation of intermetallic phases. Ni-element is also an austenite former, it stabilises the austenite (γ)-phase whereby the crystal structure from ferrite-δ (BCC) change to austenite-γ (FCC). Furthermore, Mo-element is a ferrite former enhancing pitting corrosion resistance of the material. On the other hand, when Mo-element is too high it increases the tendency to form the intermetallic phases [8]. The interactions of the major alloying elements such as Cr, Mo, N, and Ni is very complex when forming a stable duplex structure that responds well to the fabrication processes such as welding, hence caution should to be practised to obtain the ideal chemical balance when utilising highly alloyed stainless steel such as SAF2205 grade, with chemical compositions as highlighted in Table 2 above.

2.2.3 Welding of duplex stainless steel and the effect of thermal cycle on steel microstructure

The various welding techniques namely; Plasma Arc Welding (PAW), Flux Cored Arc Welding (FCAW), Shielded Metal Arc Welding (SMAW), Submerged Arc Welding (SAW), Gas Metal Arc Welding (GMAW) and Gas Tungsten Arc Welding (GTAW)/ Tungsten Inert Gas (TIG) are frequently employed with success to fuse duplex stainless steel material grades [11]. When such welding operations are carried out incorrectly, they can alter the original microstructure affecting the composition of the steel, which will prompt variations in corrosion resistance and will eventually affect mechanical properties. This can further present residual stresses and physical defects causing additional deterioration of the properties in the welded steel. The duplex steel structure requires regulated and well controlled welding parameters which can be accomplished through good welding practices by the approved welding personnel. The incorrect welding practices can lead to substantial loss of corrosion properties at the FZ and HAZ sometimes extending to the BM depending on the thermal cycles and the temperature that the welded material was exposed to. The duplex stainless steels characteristics can be worsened if the material is exposed to thermal cycles, since the high-temperature decomposition of ferrite causes the formation of detrimental secondary phases [8]. Although these conditions are necessary especially during welding operations, they can also add to the development of coarse-grained weldment deposits, a wider heat affected region (HAZ) and the precipitation of brittle intermetallic phases, which may be followed by an isothermal heat treatment to restore this balanced duplex microstructure. The heat treatment is not often practical when manufacturing big components, hence it is essential to govern welding conditions and welding procedures such that cooling is slow enough for adequate austenite transformation, but fast enough to limit precipitation of secondary phases [8].

PWHT of the fused steel is sometimes mandatory, but not as always when welding the duplex stainless steels. When it becomes obligatory to heat treat the duplex stainless steel to restore phase balance, to reduce residual stresses and to eliminate detrimental precipitates, solution annealing by applying accurate materials annealing temperature is performed. This is achieved by solubilization at 1050-1100℃ and application of the cooling rate specified by the Original Equipment Manufacturer (OEM), standards/procedure and codes to avoid the microstructural modifications of the welded regions [12].

2.2.3.1 Metallurgy of duplex stainless steel weldments

As discussed in the preceding section, the phase balance of the welded duplex stainless steel is vital in order to obtain excellent weld properties of the duplex structure with optimal benefits. This is important because when the ferrite-δ is high it will result in brittleness, whereas lack of ferrite-δ will result in poor SCC resistance of HAZ [13]. In the HAZ the amount of the ferrite ranges from 22% to 70% depending on the closeness to the FZ were high temperatures are introduced.
The austenite (γ)/ferrite (δ) phase balance within the duplex microstructure can be predicted using multi-variable linear regression demonstrated by equations 1, 2 and 3 below.

$$\mathrm{Cr}_{eq} = 1.73\mathrm{Si} + Cr + 0.88\mathrm{Mo} \qquad \text{Equation 1}$$

$$\mathbf{Ni}_{\boldsymbol{eq}} = \mathbf{24.55C} + \mathbf{Ni} + \mathbf{21.75N} + \mathbf{0.4Cu} \qquad \text{Equation 2}$$

$$\%\mathrm{Ferrite} = -20.93 + 4.01\mathrm{Cr}_{eq} - 5.6\mathrm{Ni} + 0.016\mathrm{T} \qquad \text{Equation 3}$$

Where T (°C) is the annealing temperature (1050°C to $\pm$1150°C) and the alloying elemental compositions are measured in weight percent (wt.%).

2.2.3.2 Duplex stainless steel Heat Affected Zone-HAZ

The HAZ is the area of base metal (BM) that has had its microstructure altered by exposure to high temperatures during welding [12]. After the welding operations the HAZ of the duplex stainless steel ought to have corrosion resistance and impact toughness comparable to that of the BM. However due to the higher thermal conductivity of steels and the high heat input during welding operations, Duplex Stainless Steel (DSS) grades exhibit a narrow HAZ when compared to the austenitic stainless steel grades [15]. When the heat input is too low the weld becomes predominantly ferritic and will not have the same characteristics as the BM [5].

2.2.4 Transformations of secondary phases in duplex stainless steel

The highly alloyed duplex grades (Table 2) makes it prone to the formation of inter-metallic phases after extended service at high temperatures or following incorrect welding protocols or inaccurate PWHT. The typical intermetallic phases that can nucleate when the highly alloyed duplex stainless steel is subjected to the temperature of formation are highlighted in Table 3, in conjunction with Figure 2-2 illustrating the time at temperature for formation [15].

Table 3: Temperature at which the Intermetallic phases transform in DSS [12]

Intermetallic phases	**Stoichiometry compounds**	**Elemental Composition (wt.%)**	**Lattice type**	**Temperature range (℃)**
Sigma-σ	Fe-Cr-Mo	Cr: 30 Ni: 4 Mo: 7	BCT	600-1000
Chi-χ	$Fe_{36}Cr_{12}Mo_{10}$	Cr: 25 Ni: 3 Mo: 14	BCCαMn	700-900
Carbides	M_7C_3 $M_{23}C_6$	Cr: 58 Ni: 2.5 Mo: 12	FCC	950-1050 600-950
Laves-R	Fe_2Mo	Cr: 25 Ni: 6 Mo: 35	Trigonal	550-650
Pi-π	$Fe_7Mo_{13}N_4$	Cr: 35 Ni: 3 Mo: 34	Cubic	550-650
Alpha prime-α'	Fe-Cr	Cr: 65 Ni: 2.5 Mo: 13	BCC	300-525
Nitrides	Cr_2N CrN	-	Hexagonal Cubic	700-900

The precipitates of the secondary phases such as the sigma (σ), Chi (χ) phases, carbides ($M_{23}C_6$) and nitrides (Cr_2N) (Table 3), on a microscopic scale, are not ideal as they can negatively affect the material's properties by dropping its toughness [16]. The presence of secondary phases (sigma-σ and Chi-χ) likewise reduces the metal overall corrosion resistance as they are considerably enriched in Cr-element, making the metal alloy more susceptible to localized corrosion attack. The ferrite-δ to austenite-γ volume percentage should be maintained at 50%, whilst balanced by other alloying elements, either during fabrication or during operations. During welding this balance is almost unattainable due to ferritisation at high temperature associated with thermal input from the molten welding consumables. The high ferrite content is not ideal as the material becomes brittle and more prone to pitting attack [16]. During the welding of stainless steels, the cooling rate and heat input are the most important variables that need to be regulated, as these variables influence the ferrite-to-austenite transformation. When holding the material in temperature range of 300-1000°C for extended durations it will promote the precipitation of sigma-σ and Chi-χ phases in the HAZ. In addition, prolonged heating in the temperature range of 350-550°C can cause 475°C temper embrittlement, and for this reason the maximum recommended service temperature for duplex is about 280°C.

The Isothermal precipitation diagram for duplex stainless steels shown in Figure 2-2 below, present the temperature versus time diagram for the formation of secondary and or intermetallic phases. From the C-curve (Figure 2-2) it can be noticed that there are fewer secondary phases that can nucleate with potential of growth at lower temperatures (±300°C). The C-curve also demonstrate another batch of intermetallic phases that precipitate at the high temperatures (±600-1000°C), which are highly probable to nucleate during the welding of high alloyed steels. It is at the temperature of (650-950°C) whereby the ferritic matrix suffers from decomposition process causing precipitation of harmful secondary phases. Thus the balance of the alloying elements, temperature and time need to be determined, as guided by the fabrication standard and codes that are formally translated into the working procedures/ protocols i.e. Welding Procedures Specifications (WPS) and Procedure Qualification Records (PQR) to lessen or eliminate the formation of deleterious phase's and weld defects [6]. During welding the detrimental precipitation reaction can be avoided by minimising the total time at temperature in the "red hot" range rather than managing the heat input for any one pass. Likewise, the deleterious phases can be avoided by allowing the starting material to cool slowly through the 700 to 1000°C range, or by allowing the material to air cool in to this temperature range for a minute or so prior to water quenching.

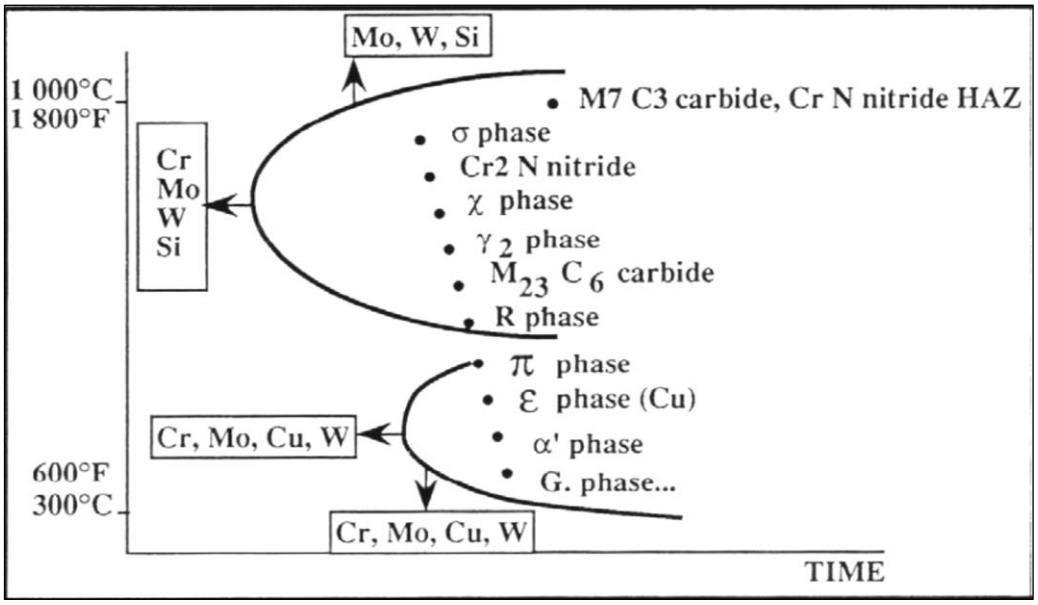

Figure 2-2: C-Curve for the kinetics of precipitation of intermetallic phases as a function of alloy content **[6]**.

When the material is slow cooled after welding the formation of austenite is encouraged on the other hand the precipitation of intermetallic phases could initiate. Hence the level of cooling need to be kept moderately slow to retain the phase balance by missing the nose of C-curve preventing the nucleation of the detrimental secondary phases (Figure 2-2) [16].

2.2.4.1 Precipitation of the sigma (σ)-phase

The σ-phase is rich in Mo-element and Cr-element and the non-magnetic inter-metallic iron, forming at the high temperature of 600-1000℃. The Cr-element diffusion in ferritic matrix of the duplex structure is the most significant thermodynamic process towards transformation of σ-phase. Likewise, elements such as silicon (Si), nickel (Ni) and manganese (Mn) enhances the sigma σ-phase transformation. The phase takes the form of a complex tetragonal crystal structure made of 30 atoms per cell. The eutectoid decomposition of ferrite (δ)-phase to sigma (σ)-phase and secondary austenitic (γ_2)-phase nucleate at a rapid rate at the temperature of 950 to 1210℃ in (Equation 4). The presence of secondary austenitic-γ_2 can be due to two mechanisms, from the existing austenite-γ or within the ferrite-δ [12].

$$\boldsymbol{\delta \rightarrow \gamma_2 + \sigma} \qquad \text{Equation 4}$$

The preferential nucleating site for the σ-phase is at the ferrite/ferrite (δ/δ) and ferrite/austenite (δ/γ) grain boundaries. The grain boundaries are typically the preferential nucleating sites for the new formed secondary phases through heterogeneous nucleation and growth. Grain boundaries and other nucleating sites such as triple points have relatively weak bonding and high interfacial energy for the nucleation and growth of the intermetallic phase when conditions are conducive. The σ-phase preferentially grows into BCC structure of the ferrite (δ)-phase as the diffusion rate is 100 times faster in comparison to the FCC structure of the austenite (γ)-phase [16]. The solid-state phase transformation of σ-phase in tempering heat treatment is high when compared to the quenching heat treatment, which can be attributed to the cooling rate that is below 1*K/s* of the required quenching heat treatment for the formation of σ-phase. The air-cooled welded parts of nominal thickness are generally greater than 1*K/s*, and so the transformation of the σ-phase is not promoted. On the contrary the precipitates of σ-phase is inevitable when thicker parts are welded. When the cooling rate is increased and or chemical composition are modified the σ-phase volume content can be minimised. Therefore, it is vital that the cooling rates are controlled as minor traces of σ-phase are enough to reduce the impact strength in duplex stainless steel. The duplex stainless steel with as low as 1–2% of the σ-phase can reduce the toughness of the grade even though the tensile properties are less affected [17].

2.2.4.2 Secondary austenite (γ_2)-phase

As can be seen in the eutectoid reaction, Equation 4, the ferrite(δ)-phase decomposes to sigma(σ)-phase and secondary austenite (γ_2)-phase, facilitated by rapid diffusion along ferrite/austenite (δ/γ)

grain boundary at a temperature range of 950 to 1210℃ [18]. The (γ_2)-phase comprises of similar compositions as the surrounding ferrite-δ. The phase has varying density within the regions of FZ and HAZ, and it precipitate and grow towards the ferrite phase of the dual structure. There are two distinct forms of secondary austenite-γ_2; one form simply grows off the existing austenite-γ and the other form nucleates within the ferrite (δ)-phase which is associated with previously formed chromium nitrides (Cr_2N). The Cr_2N nucleate initially at the inter-phase interface or in the ferrite (δ)-phase after welding resulting in a local depletion ferrite promoting elements of Mo and Cr. The reduction of these elements then promotes the nucleation of secondary austenite (γ_2)-phase at the interface and the subsequent growth within the ferrite (δ)-matrix [19].

2.2.4.3 The precipitation of chi (χ)-phase

The chi (χ)-phase nucleate prior the sigma (σ)-phase can nucleate at the temperature range of 700–900℃. The χ-phase nucleate at the ferrite/ferrite (δ/δ) interface and grows into the ferrite structure as demonstrated by Figure 2-3 (a)-(d), between the times t_0 to t_3, where $t_3 > t_2 > t_1 > t_0$.

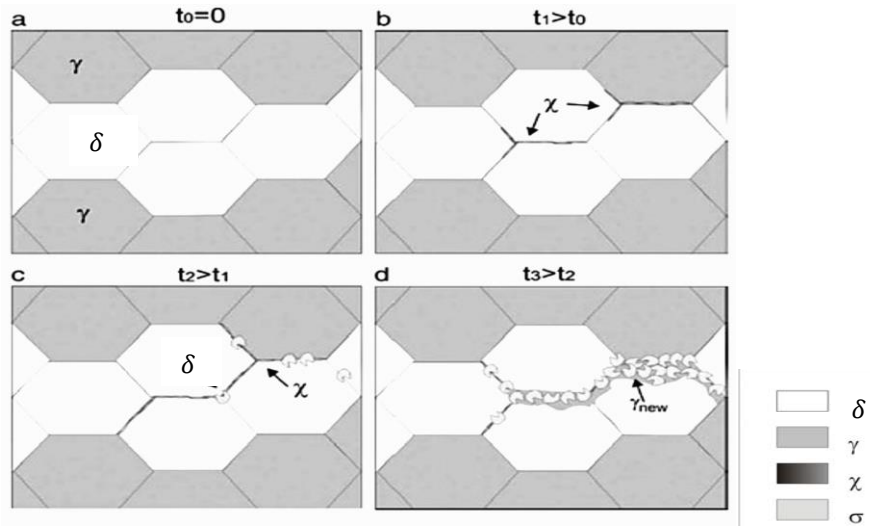

Figure 2-3: Chi (χ)-phase precipitation at ferrite/ferrite grain boundaries [16].

The σ-phase formation takes place at the detriment of χ-phase (Figure 2-3). The χ-phase ($Fe_{36}Cr_{12}Mo_{10}$) is much richer in Mo than the σ-phase (Fe-Cr-Mo). Mo-element is heavier thus making it is plausible to contrast between the two secondary phases (σ and χ) when using magnification tools of Backscattered Electron Microscope (BSE) and Energy Dispersive X-Ray microscopy (EDS) to distinguish these phases. The χ-phase is thermodynamically more unstable

than the σ-phase hence it transforms into σ-phase during ageing. The χ-phase always forms at the early stages of ageing and is consumed by the σ-phase precipitation and growth [17].

2.2.4.4 Precipitation of carbides and nitrides in duplex stainless steel

The precipitation of chromium nitrides (CrN/Cr_2N) generally initiate between the temperatures of 700–900℃, when the rapid cooling is applied from high annealing temperatures due to the saturation of ferrite-δ with nitrogen. The nitrogen segregation increases within ferrite-δ when temperatures are higher and upon cooling the solubility starts to decrease making ferrite-δ to be saturated with N-element, initiating the nitrides (Cr_2N) nucleation at the intra-granular sites. The other form of nitrides that nucleate during welding operations particularly in the HAZ has stoichiometry of CrN in addition to the Cr_2N. The chromium nitrides can lower corrosion resistance of the steel if precipitated in large percentage volume. On contrary the slower cooling through this range will favour austenite-γ and, in some cases, intermetallic precipitates [20].

Although the carbides ($M_{23}C_6$ and M_7C_3) can nucleate at the temperatures of 450–800℃ in SAF2205 grades, they are not generally of a practical concern during welding, as this stainless steel grade contain low carbon level (0.03wt%C), as such the carbides does not prove detrimental factor to the duplex stainless steel weldments. The $M_{23}C_6$ or M_7C_3 can be any metallic carbide where “M” denotes the metallic element [20].

2.2.4.5 Precipitation of other phases - R, η, τ and the alpha prime (α') phase

The R-phase precipitates at early stages of the aging process, as the aging time elapse, they transform into sigma σ-phase at the inter-granular and intra-granular sites at the temperatures range of 550–650℃. The stability of the R-phases increase with Mo-element content hence the phase is Mo-rich compound.

The η-phase transformation takes place at 600℃ during the prolonged aging and isothermal heat treatment durations. This phase is often confused with sigma σ-phase as it is also rich in Mo-element as well as Cr-element. Other secondary phases forming at the at ferrite/ferrite (δ/δ) boundaries of the duplex structure at the same temperature conditions include the tau(τ)-phase which comprise of needle like structure of orthorhombic lattice type.

The alpha prime (α’)-phase has the BCC structure and it transforms at 300–525℃ encouraging the embrittlement of these metal alloy. The embrittlement is triggered by decomposition of ferrite δ-phase into α’-phase also rich in Cr, Fe and Mo elements. At the temperature of 475℃ the rate of

embrittlement is high, and the alpha prime (α')-phase occurrence is also referred to as the 475℃ embrittlement [53].

2.2.5 Weld solidification mechanism

Duplex stainless steel solidifies primarily as ferrite-δ and partially transform to austenite-γ on further cooling to a matrix of ferrite-δ and austenite-γ, depending on several factors such as the alloying constituents, processing temperature, cooling temperature and the cooling rate. When the duplex stainless steel contains more elements of ferrite formers such as Si, Mo, and Cr than those of austenite-γ former such as C, N, Ni and Mn, it will initially solidify as ferrite-δ and then transforms to austenite-γ nucleating and growing at the grain boundaries as the temperature decrease below ferrite solvus-line (Figure 2-4-Pseoudo binary for solidification of duplex stainless steel). The equilibrium composition of the austenite-γ and ferrite-δ will continuously change with temperature and the level of the alloying elements specifically those of Cr-element and Ni-element, as demonstrated by the solvus-lines in Figure 2-4. The diffusion becomes slow as the temperature drops to the final phase composition that exists at lower temperatures. Thus, the necessary phase composition can be retained by quenching at this temperature [21].

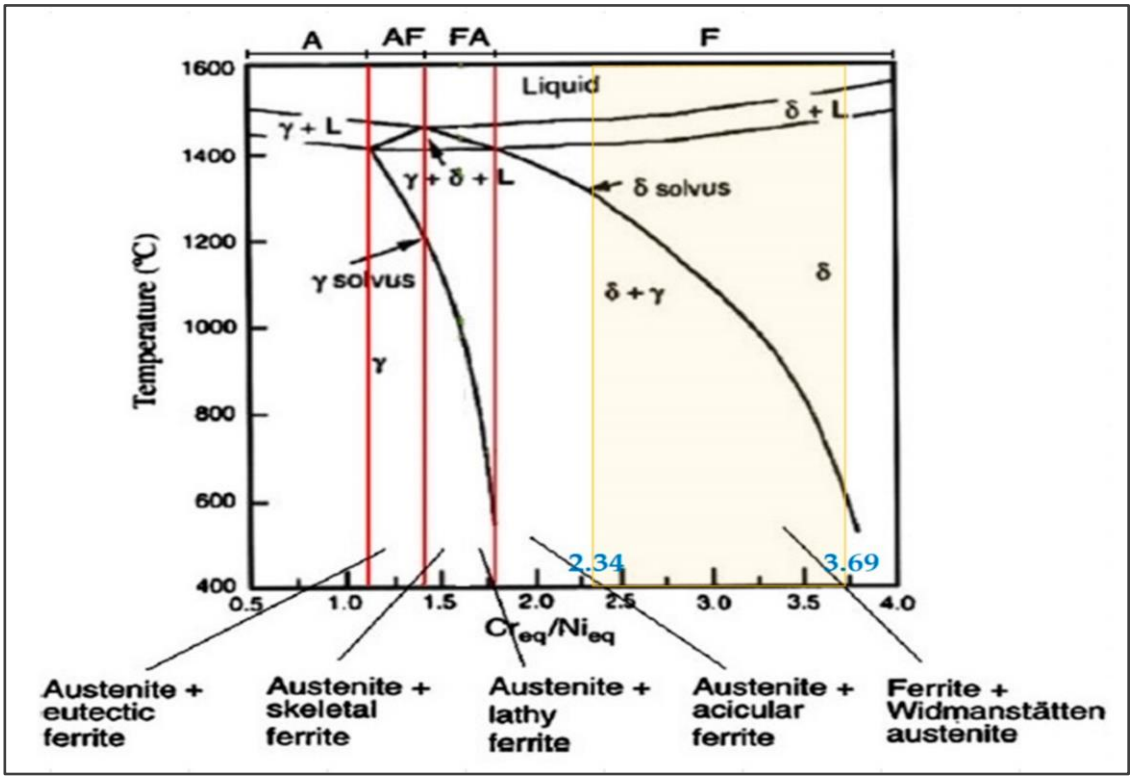

Figure 2-4: Elevated temperature region of pseudo binary phase diagram for the duplex stainless steel [22]

During solidification of the weldments, the metal that solidify initially comprise of high levels of ferrite stabilising elements e.g. Mo-element, Si-element and Cr-element.

2.2.6 Heat treatment of Duplex Stainless Steels (DSS)

The application of heat treatment in DSS is usually not necessary. However, for certain application it is prescribed by technical standards to conduct stress-relieving annealing before use [23]. The duplex stainless steels have high-temperature oxidation resistance, however the SAF2205 grade like other grades of DSS suffer 475℃ embrittlement when held for short durations (approximately 15min) at temperatures above 300℃. The phase balance in SAF2205 obtained through the precise heat treatment is crucial in maintaining the material mechanical properties. The DSS solidifies to ferrite (δ)-phase at a moderate cooling rate during production or welding operations while promoting a favourable phase proportion [23]. The long holding times at temperatures between 300℃ and 1000℃ and slow cooling rates during heat treatments (Figure 2-2) should be avoided as this will promote the precipitation of the brittle inter-metallic and detrimental secondary phases as discussed in the previous sections. Consequently, the annealing temperature must be strictly controlled, and the steel must be quenched rapidly from the annealing temperature to prevent the secondary phase precipitates from growing. If the material is embrittled, the situation can only be rectified by a full-solution annealing treatment such as heat treatment application of the material at $\pm$1035℃ to 1050℃ for five minutes, which will restore the austenite-γ and ferrite-δ microstructure. The grade of SAF2205 can be annealed at 1020℃ to1100℃ followed by rapid cooling. This schedule applies for both solution annealing and stress relieving heat treatment of the DSS. Annealing temperatures that are above 1050℃ often result in an increase of ferrite-δ content of the heat-treated material.

2.2.6.1 Preheat and Inter-pass Temperatures

Preheating of duplex stainless steel to a maximum temperature of 75℃ may be applied when necessary. However, it is preferred not to preheat duplex stainless steel prior to welding as it may negatively affect the cooling rate necessary to attain optimum austenite-γ and ferrite-δ phase balance, because the heat input is a secondary factor relative to weld metal composition in controlling the austenite-γ and ferrite-δ phase balance. Excessive inter-pass temperatures can lead to the SAF2205 grade losing the ductile property to become brittle resulting in low impact values in the root region, thus the welding parameters are maintained at the weld inter-pass temperature of

<250℃, which has the heat input of ±0.5 to 2.5kJ/mm. The base metal should be permitted to cool down to room temperature following welding operations [15].

2.2.6.2 Post Weld Heat Treatment - PWHT

The PWHT in duplex stainless steels is generally not obligatory however it might be crucial once the amounts of deleterious intermetallic phases have formed. The corrosion properties in the post weld heat treated duplex stainless steel are not only associated to the presence of the secondary austenite (γ_2) but also to its morphology that is influenced by the heat treatment parameters. In addition, the secondary austenite (γ_2) with coarse grains encourages superior corrosion properties than the secondary austenite (γ_2) having finer grains. When conditions compel that the induction heat treatment should be carried out, a significant thermal gradient may arise across the thickness of the weld subsequently different corrosion properties may be found across the thickness of the weld joint [24].

2.2.7 Sensitization and Intergranular corrosion on SAF2205

The stainless steel of SAF2205 grade have very good resistant to Intergranular Corrosion (IGC) owed to the two-phase structure of metastable ferrite-δ present within the austenite-γ matrix, and the moderate levels of Nickel (Ni) and a very low Carbon (C) content. Chromium (Cr) diffuses faster from ferrite δ-structure than it is from austenite γ-structure at the typical sensitising temperature between 425℃ to 815℃, upon which the carbides nucleate and grow favourably at the ferrite/austenite (δ/γ) grain boundaries. However, the phenomenon of sensitisation is often not much of the concern in duplex stainless steel as there is less carbon to form the carbides. When the conditions are conducive enough that the chromium carbides forms, the areas that are depleted from Cr-element are widely distributed within the austenite grains adjacent to the δ/γ boundaries and they can be replenished by diffusion during stress relief annealing [25]. The stress relief annealing operation will impair the precipitation of nitrides and carbides at the highly energised grain boundaries.

2.3 Austenitic stainless steel (AISI304L)

The austenitic stainless steels are generally nonmagnetic which are found to be beneficial for various engineering applications. The austenitic stainless steel comprise of Faced Centred Cubic (FCC) structure having excellent formability and outstanding corrosion resistance. The austenitic grades are the most readily formed as they have low yield stress (YS) characterised by strong work hardening. This material can be work hardened by means of cold work to higher strength, but they are not hardened by means of heat treatment. But it can be strengthened by means of solid solution strengthening technique, whereby some level of the alloying elements viz. Chromium (Cr), Nickel (Ni), Carbon (C), Manganese (Mn) etc. are diffused. Contrarily, the detrimental effect of carbon level to corrosion resistance propel that C-element should be minimally used as a strengthening element in the welded austenitic stainless steel. Hence this material is also obtainable with the grades that has varying elemental C-element level, with AISI304 grades having the <0.10wt.%C, and AISI304L grades having lesser (<0.03wt%C) or even without C-element [26].

2.3.1 Austenitic stainless steel phase and the alloying elements

Austenitic stainless steel has a single-phase microstructure having FCC crystal structure that can be stabilised by adding appropriate levels of Ni, Mn and C elements. The AISI304 grades are the most familiar and widely used and they are also referred to as 18/10 and 18/8, with both ratios referring to the nominal composition of 18wt.%Cr and 8%wt.Ni. They are resistance to pitting, crevice and general corrosion which is largely improved by further alloying the austenitic grades with increased amounts of Mo and Cr elements, whereas the increase in Mo and Ni levels are more beneficial to SCC resistance. Table 4 - present some of the major alloying elements in AISI304 grades including their compositions expressed in weight percentage (wt.%). This steel grades can have Cr and Ni alloying elements at various compositions that are anywhere within the austenite region of Schaeffler Delong diagram (Figure 2-1). As Cr and Mo elements are increased to enhance a specific properties usually corrosion resistance, Ni and or other austenite stabilizers should also be added if the austenitic structure is to be preserved [17].

Table 4: Alloying compositions for austenitic stainless steels - AISI304 grade. **[27]**

Stainless steel grade	**Alloying elements for austenitic stainless steel**						
AISI304	**Carbon C (wt.%C)**	**Nitrogen N (wt.%Ni)**	**Chromium Cr (wt.%Cr)**	**Nickel Ni (wt.%Ni)**	**Molybdenum Mo (wt.%Mo)**	**Manganese Mn (wt.%Mn)**	**Silicon Si (wt.%Si)**
	0.02-0.08	0.09	18-20	8-12	0.3	2 (Max)	0.45-1

Austenitic stainless steels have many benefits from a metallurgical point of view, including those highlighted in Table 1. Their FCC structure is very tough and ductile down to temperatures of zero. The least corrosion resistant versions of this steel grade can withstand the normal corrosive attacks of everyday environments, whereas most of corrosion resistant grades can even withstand the extreme corrosive environment such as those of saline conditions. If this alloys were to have any relative weakness it would be that they are less resistant to cyclic oxidation than the ferritic stainless steels, because of the steel greater thermal expansion coefficient tends to cause the protective oxide coating to spall [28].

2.3.2 The influence of thermal cycle on the welded austenitic stainless steel microstructure

Austenitic stainless steels are readily weldable with considerable tolerance for variation in welding conditions. Amongst numerous available welding techniques, the GTAW and SMAW or the TIG are commonly applied to join and or fabricate parts or components from this metal alloy. The TIG welding is considered attractive technique, because it has the lower heat input associated with it when compared to SMAW technique. The lower heat input is beneficial to the austenitic stainless steel weldment as it can be cooled at a rapid rate, subsequently alleviating likelihood of sensitisation in weld region of HAZ. The sensitised HAZ affect the material adversely if not alleviated after welding activities, causing unfavourable conditions to manifest, expounded as follows;

(a) When the HAZ is exposed to high welding temperatures for extended durations the precipitation of $Cr_{23}C_6$ at the grain boundaries and locally lowering the Cr-element content take place, and the preferential corrosive attack and or weld decay proceed.

The precipitation of carbides can be alleviated by means of full solution heat treatment at 1050℃ or annealing at 900℃ to allow chromium to diffuse from bulk into the impoverished zone.

(b) The stress set up from contraction accompanying solidification of weldments of fully austenitic weld metal can produce hot cracking. These conditions can be alleviated by ensuring that the weld metal contains a minimal delta-ferrite.

2.3.3 Austenitic stainless steel weldments metallurgy

Austenitic stainless steels are predominantly prone to the hot cracking that can be mitigated using filler material that contains small percentage of retained ferrite to join the parts or plates. Although suitable filler materials have been developed, it turns to be dilute by high amount of austenite in the parent material especially at the roots of welds. The slower cooling rate at the weld root nugget reduces the amount of retained ferrite and increases the likelihood of hot cracking. While filler materials can compensate for undesired changes in the microstructure of the weld solidified region, they cannot prevent the HAZ microstructural changes [14]. Adjacent to FZ and HAZ the degree of grain coarsening may be experienced because of grain structure evolution owing to high thermal input during welding, causing the grains to go through heat treatment process of growth, recrystallisation and or even recovery towards the cooler regions adjacent to the BM. The sensitivity of the steel to chloride SCC is increase with increasing grain size.

2.3.4 Heat Affected Zone (HAZ) of austenitic stainless steel weldments

During welding operations of steels, the HAZ is normally exposed to inconstant cycles of cooling and heating with peak temperatures from solidus to ambient. The arc welding is regarded a feasible technique to join ferrous materials, with austenitic stainless steels not being an exception. However, there are anomalies associated with arc welding of ferrous metals i.e. chemical inhomogeneity at the HAZ and the FZ of the joint parts affecting weld quality by causing defects such as cold-laps, micro-porosity, micro-fissures, hot-cracks, sensitisation etc. The rapid thermal cycles experienced in the HAZ from fusion welding promotes metallurgical changes that significantly affect the corrosion resistance of the weld joints because of the existing metallurgical inhomogeneous and dendritic microstructure with micro-segregation. In the welded austenitic stainless steel, a degree of grain coarsening may be experienced very close to the FZ and or FL, while sensitivity to SCC is increased with increasing grain size as well as sensitisation.

2.3.5 Precipitation of inter metallic phases in austenitic stainless steel

The intermetallic phases that normally exist in the weldments of austenitic stainless steels are presented in Table 5 and they can be classified as Topologically Close Packed (TCP) and Geometrically Close Packed (GCP) phases . The TCP phases are characterized by layers of close packed atoms which are separated by relatively large interatomic distances. The layers of close packed atoms are displaced from others by inserted large atoms evolving a characteristic topology. On the other hand, the GCP phases are close packed in all directions and they form mainly in Ni base alloys such as austenitic stainless steels. The three TCP phases that are often found in the austenitic stainless steels are the chi (χ)-phase, sigma (σ)-phase and laves (η)-phase. The other intermetallic phases that are rarely found are the Mu (μ)-phase, R-phase, gamma prime (γ')-phase and gamma double prime (γ'')-phase. The chemical compositions of the intermetallic phases forming in austenitic steel are presented in Table 5 below This intermetallic phases are associated with undesirable effects in the steel proprieties although precipitation of the laves (η)-phase (Fe_2Nb) can result in precipitation hardening strengthening mechanism [29].

Table 5: Composition of intermetallic phases precipitate in austenitic stainless steels [29].

Phase	Nominal Compositions	Lattice type
Topologically Close Packed phases (TCP)		
Sigma (σ)-phase	Fe,Ni,Cr,Mo	BCT
Chi (χ)-phase	$Fe_{36}Cr_{12}$ Mo_{10}	BCC
Laves (η)-phase	Fe_2Mo, Fe_2Nb	hex
G-phase	$Ni_{16}Nb_6$ Si_7, $Ni_{16}Ti_6$ Si_7	FCC
Carbides	$M_{23}C_6$ M_6C_4	FCC Diamond cubic
Geometrically Close Packed phases (GCP)		
Z-phase	CrNbN	Tetragonal
M_2N	$(Cr,Fe)_2N$	Hexagonal
M_2B	$FeMo_2B_2$	Tetragonal

The transformation of hard and brittle phases of chi (χ) and sigma (σ) makes the stainless steel to become more brittle. The embrittlement effect transpires in the temperature range of 500–900℃. This is a sluggish process and is usually not problematic during the welding of steel, but it can take place when the elevated operational temperature is applied or when the welded components are stress relieved. Secondary phase formation listed in Table 5 above, are basically promoted by the ferrite forming elements such as high Mo and Cr content. Delta-ferrite also transforms more rapidly than austenite, subsequently the alloys containing large amounts of this phase will degrade faster than an austenitic stainless steel with only a small percentage of ferrite – hence the problems with duplex stainless steels [23].

2.3.5.1 Precipitation of the sigma (σ)-phase in austenitic stainless steels

The sigma (σ)-phase has Body Centred Tetragonal (BCT) crystal lattice that precipitates at the temperatures of 600 – 1000℃. The Cr level in σ-phase is 25 – 76wt.%, thus the formation of this phase is encouraged by an increase in Cr content of more than 17 – 20wt.%Cr, in contrary the phase is lowered by an increase in Ni level. The amount of Cr and Ni equivalence can be used to evaluate the possibility of σ-phase formation in Fe-Cr-Ni alloy. The propensity of σ-phase precipitating in austenitic stainless steels depends on the chemical composition of the residual austenite after precipitation of carbides and nitrides which always form first [28]. The tendency of austenitic stainless steels to form σ-phase can be determined by means of Hull formulae for Equivalent Chromium Content (ECC) as per equation 5 below. The steel is prone to formation of σ-phase once the ECC value is more than 18wt.%.

$$\mathrm{ECC} = \%\mathrm{Cr} + 0.31\%\mathrm{Mn} + 1.76\%\mathrm{Mo} + 0.97\%\mathrm{W} + 2.02\%\mathrm{V} + 1.58\%\mathrm{Si} + 2.44\%\mathrm{Ti} + 1.7\%\mathrm{Nb} + 1.22\%\mathrm{Ta} - 0.266\%\mathrm{Ni} - 0.177\%\mathrm{Co} \quad \text{Equation 5 [22]}$$

In addition, the alloying elements of Mo, Ti, Nb also promote the precipitation of σ-phase. The precipitation rates are increased by additional 2–3wt.%Si (silicon-Si-element). Figure 2-5 below illustrate various austenitic stainless steel grades of 304,316, 321 (Ti-stabilized), and 347 (Nb-stabilized) where transformation of σ-phase is feasible at different times and temperature of 700℃. When nitrogen (N) is incorporated in the weld deposit it delays or even mitigate the nucleation and growth of the σ-phase and χ-phase. The occurrence of delta-ferrite affects the growth kinetics of σ-phase and other intermetallic phases but not the total content of these phases [28]. The delta-ferrite present in the welds of austenitic stainless steel can reduce incubation period for σ-phase formation.

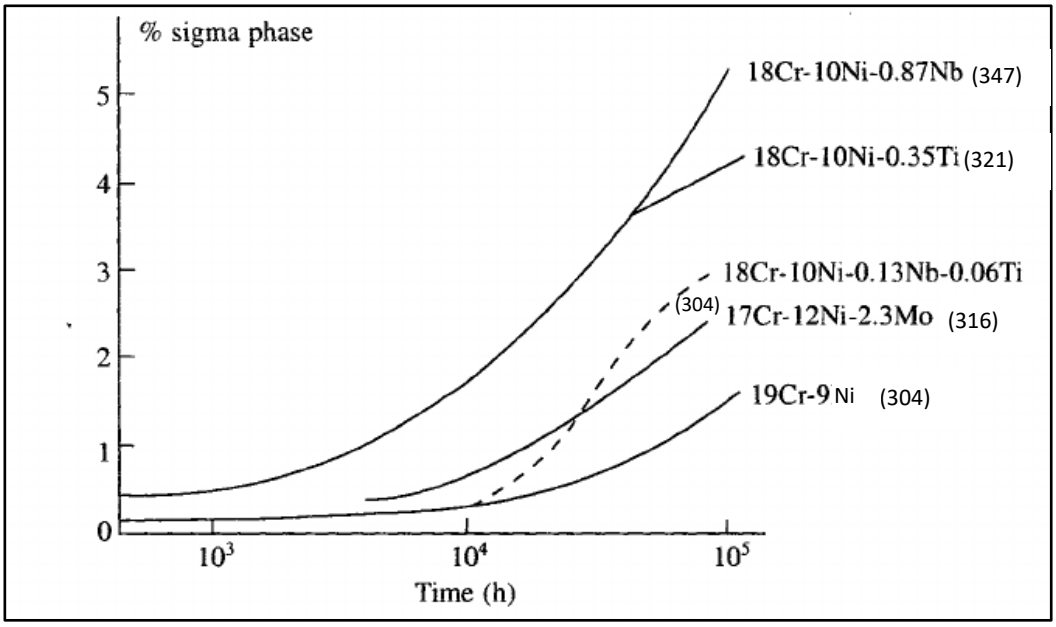

Figure 2-5: Sigma ($\boldsymbol{\sigma}$)-phase precipitation in different grades in austenitic stainless steel with respect to time at temperature (700℃) [28].

The cold worked material is characterised by decrease in incubation period for the σ-phase precipitation, whereas an increase in grain size due annealing at high temperatures retards the σ-phase transformation. The stress accelerates precipitation of σ-phase and extends its formation range to lower temperatures. The σ-phase nucleation and growth can be controlled by the rate of Cr diffusion and other elements of σ-phase former. Similarly, the compositions of delta-ferrite and σ-phase are nearly comparable, hence the delta-ferrite in austenitic stainless steel weldments transform to the σ-phase with ease through a crystallographic re-orientation. The heat input during welding has a significant effect in the precipitation kinetics of delta-ferrite and other intermetallic phases. When components are welded, the thermal effects can significantly alter the metallurgical structure of the parent metal to produce HAZ. Consequently the different parts of the weldments can have different constitutive behaviours. Furthermore, the high heat input to the weld metal can retard the decomposition kinetics of delta-ferrite similarly retarding the precipitation kinetics of σ-phase. The σ-phase is known to affect the tensile and creep-ductility of the stainless steels [20].

2.3.5.2 Chi (χ) and laves (η)-phase precipitation in austenitic stainless steel

The chi (χ)-phase is comparable to sigma (σ)-phase, although the χ-phase has less Cr and more Mo levels with Body Centred Cubic (BCC) structure (Table 5). The two phases can coexist at temperature range of 700-900℃ by precipitating at ferrite/austenite (δ/γ) grain boundaries while having similar deleterious effects [30]. The composition of χ-phase can vary appreciably with a high tolerance for metal atom interchange. The addition of carbon results in the metal atom

proportion within the χ-phase shifting towards the strongest carbide former, i.e. towards Mo at the cost of Fe and Cr elements. The presence of delta-ferrite in the steel favours the precipitation of χ-phase and σ-phase. The precipitates of the laves η-phase are also formed at the temperature range of 550–650℃ over the period of hours. This phase has the structure of B_2A, where B and A denotes the elements of Fe/Cr and Ti, Mo, Si/Nb respectively. It is possible for η-phase to form at temperatures below σ-phase and above alpha prime (α')-phase, but the long times for the phase transformation make it rare (Figure 2-6). Even though its effect would be deleterious, it seldom that it becomes a practical problem.

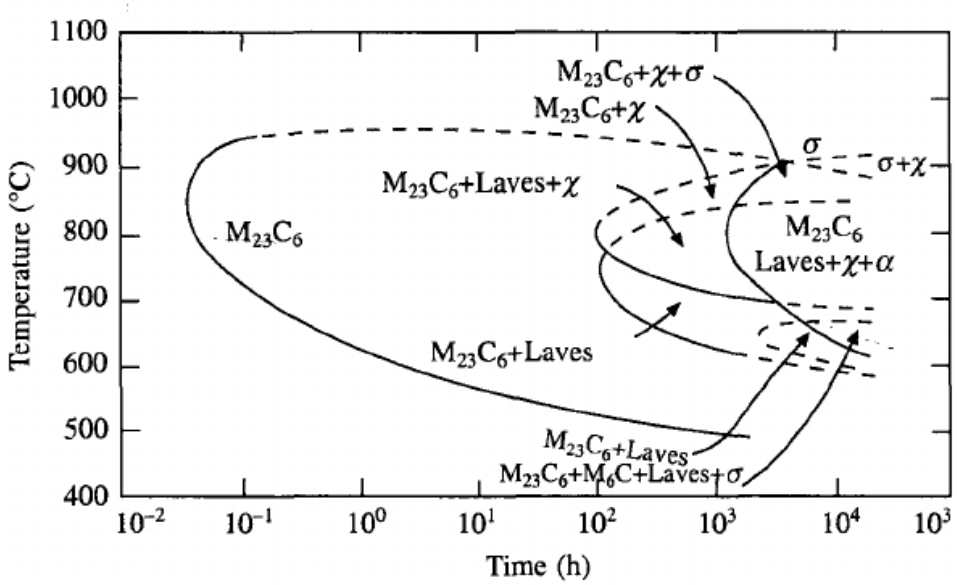

Figure 2-6: Time-Temperature-Transformation (TTT) diagram for the precipitates occurring in 18-Cr-12Ni-2Mo (Austenitic stainless steels).

2.3.5.3 The precipitation of carbide and nitride in austenitic stainless steel

The carbides ($M_{23}C_6$) are the main precipitates found in austenitic stainless steels having orthorhombic structure. The precipitates of carbides transform at the temperature that the austenitic stainless steel becomes saturated with C-element [30]. The $M_{23}C_6$ precipitates usually form before the intermetallic phases, whilst the formation of the intermetallic phases increases, they re-dissolve due to thermodynamic considerations to replenish the matrix in Cr, Mo, C and N. Their precipitation at the grain boundaries are known to impair the impact property more than any other mechanical property. The precipitates are also acknowledged to deteriorate the localised corrosion behaviour of austenitic stainless steel- Table 6 [28].

Table 6: Composition and crystal structures of the carbide that precipitate in austenitic stainless steel.

Carbide stochiometric	**Unit cell**	**Principal metallic elements**
$M_{23}C_6$	FCC	Cr, Fe, Mo & Ni

The $M_{23}C_6$ initiate at the grain boundaries and incoherent twin boundaries of the steel microstructure [28]. The Cr-element that reacts with the C-element originates from the matrix of austenitic stainless steel in the immediate vicinity, thus decreasing Cr content in the material immediately adjacent to the grain boundary, giving rise to the phenomenon of sensitisation also referred to as "sensitisation to intergranular corrosion". Ni-element and Mo-element decrease the solubility of carbon in austenite and accelerate the carbides precipitation, on contrary N-element retards the precipitation of the carbides [28]. The sensitised regions are prone to localised corrosion, which transpire when unsuitable heat treatment is applied or when the material is heated to higher temperatures for extended durations during welding. The HAZ of such material suffer from intergranular corrosion termed weld decay. Stainless steels can be stabilized against this behaviour by addition of titanium (Ti), niobium (Nb) and tantalum (Ta), which reacts with C-element to form titanium carbide (TiC), niobium carbide (NbC) and tantalum carbide (TaC) preferentially to $Cr_{23}C_6$ to lower carbon content of in the steel (Table 6). The filler metal with the carbon content of less than 0.02wt.%C will lessen the prospect of carbides formation. The carbides can also be reduced by heating the entire welded part above 1000°C followed by quenching with water for the dissolution of the $Cr_{23}C_6$ within the grains, thus preventing the diffusion to take place and precipitation of the carbides to form. Another possibility is through keeping the welded parts thin enough so that upon cooling the metal dissipates heat rapid enough for the carbide to precipitate. Another option, most popular, is to use L grades (low carbon grades of austenite stainless steels) for the base metal to avoid sensitisation, e.g. 304L [28].

2.3.5.4 The nitride precipitation in austenitic stainless steel

Nitrogen-element can substitute carbon contained in the carbides – $M_{23}C_6$, when the nitrogen level is higher the chromium nitride compound – Cr_2N precipitate instead. This can occur especially in duplex alloys when the alloy has high N-element solubility and it is heated to the solution annealing temperature. Cooling from high temperatures creates excess nitrogen to precipitate needle like structure of Cr_2N with the CrN nucleating at the HAZ adjacent to the weld metal.

2.3.6 Heat treatment of austenitic stainless steels

The annealing heat treatment on austenitic stainless steel is employed to restore the ductility and softness while protecting the material against corrosion, consequently post-annealing may be specified as thermal processing or post welding. The annealing heat treatment re-dissolves the carbides within the matrix consequently reducing the intergranular corrosion attack markedly. As mentioned previously the $M_{23}C_6$ usually precipitates at the temperatures of 425–900℃, while annealing at temperatures of 1010–1120℃ permit complete dissolution of the formed carbides followed by rapid cooling. The rapid cooling action using water ensures that the dissolved carbides remain in solution post the annealing treatment. Air blasting can also be applied as a cooling method when practical considerations such as distortion are ruled out. The thin section size products are difficult to cool by means of intermediate cooling rates; hence still air cooling is carried out. When air cooling does not provide adequate cooling rate to prevent carbide precipitates, maximum corrosion resistance will not be attained using this practice [30].

2.3.6.1 Post-Weld Heat Treatment (PWHT) of AISI304 stainless steels

The AISI304 grades does not generally require PWT, however if need arise that heat treatment is necessary normally due to service conditions, solution heat treatment can be completed. In most applications solution heat treatment is done to ensure the greatest degree of corrosion resistance appropriate for compositional homogenization to reduce the possibility of sensitization during high temperature exposure. In other applications heat treatment may be completed for stress alleviation to give extra dimensional stability of components to be machined and or to reduce reheat cracking and to lessen the welded materials susceptibility to SCC. Fairly low temperature treatments (±400℃) are normally applied to achieve dimensional stability and giving partial stress relief which might be adequate. Heat treatment at higher temperatures of 1000℃ may be employed to stress relieve most of the material's internal stress, while solution annealing is achieved at temperature greater than 1000℃, followed by rapid cooling to prevent the precipitates to nucleate, however new stresses of considerable magnitude could be formed. In such conditions a lower temperature treatment of ±400℃ to provide stress relief within the material without the precipitation of secondary phases might be desirable [14].

2.3.6.2 Sensitisation in austenitic stainless steel

The austenitic stainless steel of AISI304 grades contain a small amount of carbon (0.03wt%C) contributing to solution strengthening of the material; although the C-element can become undesirable during the welding operations. The C-element is austenite former and it has a great thermodynamic affinity for Cr-element that can form $Cr_{23}C_6$ when it became supersaturated and when the diffusion rates are adequate for Cr and C to segregate into precipitates. The solubility of C-element in austenite is above 0.4% during solidification but reduces significantly when the temperature decreases to room temperature. During welding activities, the steel is exposed to thermal cycle adjacent to the FZ, that facilitates $Cr_{23}C_6$ nucleation and its growth along the grain boundaries. The formed carbide can only become insoluble at intermediate temperatures of 425℃ and 815℃, and when the temperature is above 815℃ it become soluble whereas below 425℃ the diffusion rate of C-element becomes sluggish for precipitation to initiate [25]. It is mainly the diffusion of Cr-element from the neighbouring grains diffuse to initiate the nucleation and growth of transformed carbides making the Cr-mass transfer rate to be much higher along the grain boundaries than in the matrix of the grains. As diffusion progresses the $Cr_{23}C_6$ precipitates become rich in Cr-element causing areas adjacent to the grain boundaries to become Cr-depleted (Figure 2-8). This result in reduction in Cr content to the affected regions to below 10% threshold required to maintain the chromium oxide (Cr_2O_3) or chromium hydroxide [$Cr(OH)_3$] protective film [28]. The Cr-depleted zones become more susceptible to corrosion than the surrounding grains as it is known to be sensitised (Figure 2-7 and Figure 2-8). The sensitised regions serve as a preferential site for localised corrosion that will eventually progress to SCC when conditions are favourable [28].

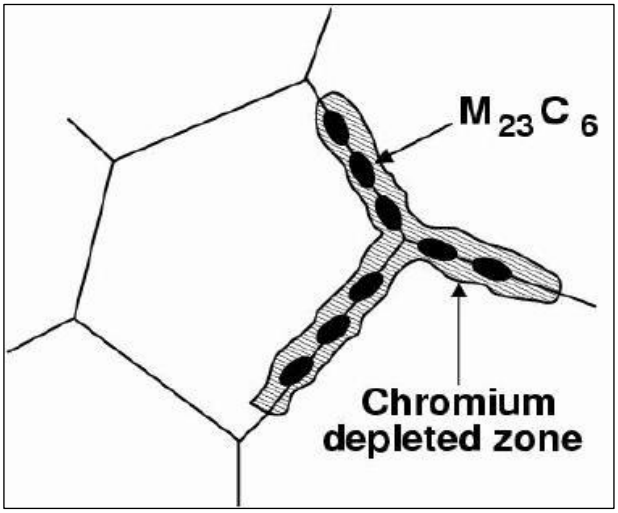

Figure 2-7: Schematic representation of the precipitation of $M_{23}C_6$ at the grain-boundary during sensitisation in austenitic stainless steel [12]

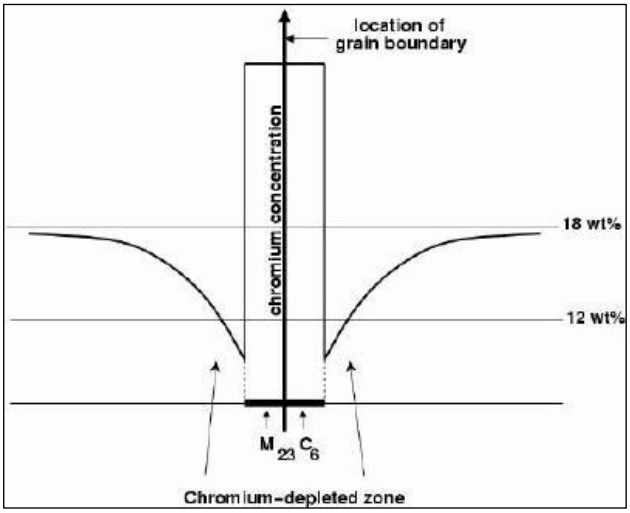

Figure 2-8: Concentration [Cr] profile at a grain boundary.

Sensitisation initiate at the grain boundaries as it is highly energised and there is high lattice mismatch between adjacent grains, thus with continuous heating more grain boundaries become sensitised. Figure 2-9 – illustrate austenitic stainless steel of AISI304 grade with varying carbon content at the temperature and durations that it becomes sensitised.

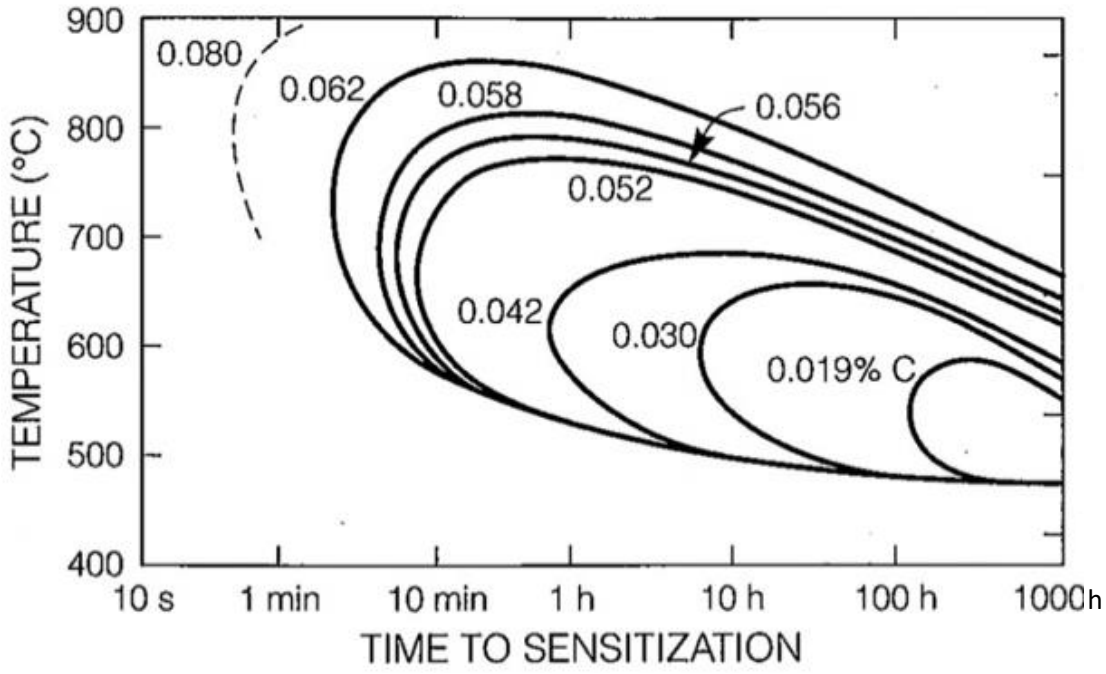

Figure 2-9: Sensitisation diagram for 18Cr-8Ni stainless steel with varying carbon content **[25]**.

The extend of sensitisation in austenitic stainless steel depends on factors such as carbon content of the metal alloy and the exposure durations to sensitisation temperature and many other design factors. According to Figure 2-9 supersaturation of steels with 0.062wt.%C is attained at the temperature of (600-850℃) at less durations, thus the sensitisation initiate faster, whereas the steels with 0.019–0.042wt.%C takes a considerable amount of time at lower temperatures (500-670℃) to become supersaturated. Below 850℃ diffusion decreases exponentially while supersaturation increases exponentially resulting in different rate to which the carbides precipitate. The diffusion at the grain boundaries becomes more rapid in comparison to the diffusion within the bulk of the grain as the grain boundaries provide excellent nucleation sites. C-element diffuses at several orders of magnitude more rapidly than Cr-element; therefore, it diffuses together with Cr, through which the Cr-element is diminished in the grain boundaries .

The Ni is one of the alloying elements that has secondary effects of increasing the carbon activity in solid solution facilitating the carbides precipitates, thus encouraging sensitisation. The presence of Mo-element behaves rather like Cr-element because it precipitates as carbide at grain boundaries which contribute to the materials Cr-depletion.

Sensitisation in austenitic stainless steel is encouraged by high temperature exposure adjacent to weld joints reducing corrosion resistance at this region (HAZ). It is at welding temperatures that the depletion of Cr-element become less than 12wt.% at the grain boundaries precipitating continuous network of $M_{23}C_6$ (Figure 2-7). Different sections of the welded parts experience different heat/ thermal energy from the welding processes, at which the weld metal (FZ) introduces high temperatures dissipating the heat in to the HAZ that eventually affect some section of BM, hence sensitisation is not uniform across these regions. Figure 2-10 illustrates sensitisation due to thermal cycles at different sections of HAZ, represented by the marked points 1, 2, 3 and 4 experiencing varying thermal exposure. The shaded area represents the temperature and time at which these points/sections are sensitised. Temperature effects that is introduced at the FZ is dissipated to different HAZ with points 1, 2, 3 and 4 experiencing varying sensitisation at the temperatures of below 550 and above 850℃, at which points 2 and 1 experience most sensitisation at different times between 550–850℃. Point 4 show this area will be slightly affected as it is a bit further from the FZ–high temperatures and adjacent to the BM–lower temperatures. The weld joint gets cooled through conduction heat transfer by the cooler BM and through the radiation of heat to the surrounding medium i.e. air, water etc. If the steel is thicker the HAZ-BM interface at point 4 could also experience some level of sensitisation when conditions become favourable. Thus, for the thicker sections butt weld increases the heat input and time spent by the region of HAZ in the sensitisation temperatures. The carbides do not form in all the regions experiencing temperature above 850℃ instead they dissolve and below 450℃ they are too sluggish to cause any concern. [28].

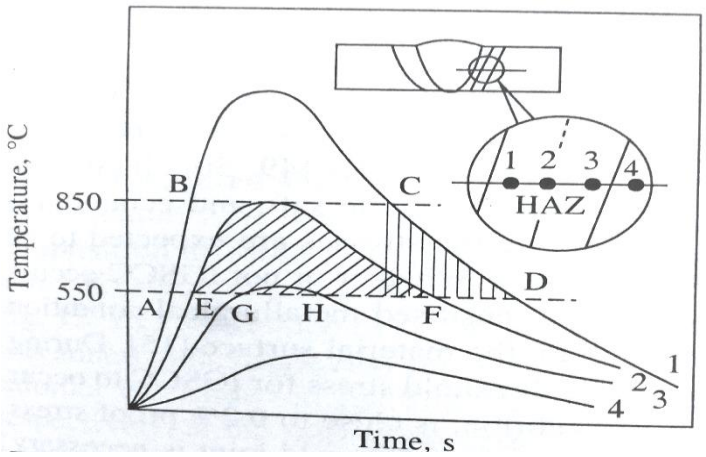

Figure 2-10: Schematic diagram indicating the effect of thermal cycling in inducing sensitisation in different sections of HAZ exposed to temperature (1) Above 850℃, (2) at 850℃, (3) Between 550℃ and 850℃ and (4) Below 550℃.

2.4 Corrosion of stainless steels

Corrosion is a gradual degradation of a metal by means of an electrochemical reaction between the metal and the surrounding environment [31]. Electrochemical reaction takes place by means of anode and cathode reaction, also referred to as oxidation reduction (REDOX) reaction expressed by equations 6, equation 7, equation 8, equation 9 and equation 10 respectively. Corrosion impacts metals properties by degrading their usefulness such as their permeability to gases and liquids, appearance, deterioration of mechanical properties etc. Although stainless steels are frequently selected for their resistance to corrosion, they are not entirely immune to deterioration due to corrosion. Whether or not a stainless steel will be corrosion-resistant in a severe corrosive condition depends on combination of several factors such as aggressiveness of the environment, the employed manufacturing technique and the residual stresses within the material. The resistance to corrosion of stainless steel is attributed primarily to the thin passive film that forms spontaneously on its surface in oxidising environments, when the steel has a minimum chromium content of 10.5wt.%. The thin passive film forms when alloying element of Cr interact with oxygen (O_2) from atmosphere forming the chromium oxide (Cr_2O_3) layer on the surface adhering strongly to the metal substrate protecting the material from interacting with corrosive surroundings. The REDOX reactions initiating corrosion are efficiently hindered by the well-developed Cr_2O_3 layer [32]. However, the dented film perhaps, damaged or removed after mechanical damage to the surface exposing un-oxidized steel will cause REDOX reaction to initiate at these area. The dented film in stainless steel can mend by means of spontaneously re-passivation in oxidizing environment [13]. The corrosion type that generally affect stainless steels are related to permanent damage of the passive film through either complete or local breakdown of the film [33].

2.4.1 Overview of stress corrosion cracking (SCC)

The stress corrosion cracking (SCC) transpires through environmentally induced crack initiation and propagation that may lead to catastrophic failure of engineering material if not properly maintained. As cited in the previous sections, that stainless steels are the preferred design materials in combating corrosion problems mainly because of protective self-healing oxide layer that the material develops. However, when this protective film has defect i.e. locally damaged by mechanical means it will expedite corrosion attack in a very narrow region, with the rest of the undamaged area remaining protected [26]. The SCC manifest within the susceptible material when the following conditions coexist; corrosive environmental exposure in the presence of tensile stress (residual and applied stresses) within the material introducing cracks and subsequently crack growth. The Venn diagram (Figure 2-11) summarise conditions that necessitate the SCC initiation and progression. The SCC and other corrosion types such as pitting, crevice and intergranular attacks initiates more readily at pre-existing surface defects created by poor workmanship during maintenance and material handling, manufacturing or fabrication processes. The SCC can also initiate on smooth surfaces that are without previous defects or dents, but during operational conditions that do not adhere to design specifications. The SCC failure mechanism manifest as non-ductile fracture of metal derived from the co-occurrence of susceptible material having tensile stresses operating in corrosive medium. It is only when these aspects exist concurrently to produce corrosion cracks, when any of these aspects is eliminated the SCC initiation can be alleviate – Figure 2-11 [7].

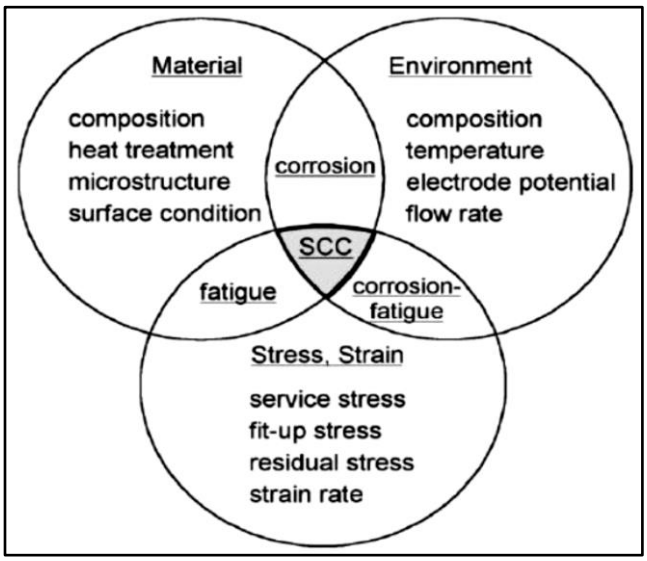

Figure 2-11: Venn diagram illustrating the three necessary conditions for SCC formation **[7]**

The typical corrosive environmental exposure that could expedite the SCC defects in stainless steels is the aqueous solutions containing chlorides ions (Cl^-), acidic environments (hydron ions –

H^+) and basic environments (hydroxyl ions – OH^-) with a specific concentration and temperature at a specific exposure duration [34]. When metals are exposed in a more complex electrolyte such as the environments containing the ions listed above, the galvanic series may be used to predict if the corrosion of the metal is possible. It should be noted that for some metals i.e. stainless steels, there are significant differences in the potential they are likely to exhibit. These differences are generally owed to the condition of the metal surface. If the oxide layer is compromised the potential may shift causing localised attack at the active sites.

2.4.1.1 Susceptible material

The Venn diagram (Figure 2-11) shows that one of the fundamentals of SCC is the susceptibility of material to corrosion. There are several factors that can influence the materials to become susceptible i.e. metal alloy elemental composition, concentration of impurities or inclusions and the concentration intermetallic precipitates. The metallurgical conditions such as the presence of secondary phases at the grain boundaries including their compositions, grain boundary segregation, defects of the passive film etc can immensely contribute towards materials susceptibility. Similarly, the fabrication techniques of welding, forming, extrusion etc. can introduce inclusions and residual stresses within the material that will eventually exacerbate the material susceptibility to corrosion attack.

2.4.1.2 Alloy composition

The alloy chemistry and microstructure have a very significant influence on SCC resistance of stainless steels. The corrosion resistance in steels can be improved through the modification of chemical compositions of the alloying elements such as selection of austenitic grades comprising of titanium (Ti) and nickel (Ni) as an alternative to the austenitic grades containing chromium (Cr) alloying element. The steels with increased Ni-element content of above 8wt.% will significantly improve the SCC resistance. Moreover, the austenitic grades that are not solution strengthened by adding carbon as alloying element i.e. AISI304L can be utilised especially when welding is a preferred fabrication technique to join components or parts as an alternative to selecting the austenitic grades of AISI304 which contains maximum carbon of 0.03wt.%. The austenitic stainless steel grades of AISI304L has low carbon content, therefore this grade is suitable for welding as the HAZ sensitisation can be reduced. Similarly, addition of alloying elements such as Mo-element and N-element improves the SCC resistance, through the beneficial effect of these elements on pitting resistance, as in many practical situations pits are formed as precursors to SCC [26].

2.4.1.3 Passivation of stainless steels

Stainless steels are naturally corrosion resistant metal alloys due their capability to auto-passivate by spontaneous formation of 1-3nm thin oxide/hydroxide film. The film is formed naturally during a reaction between the metal and oxygen present in the surrounding environment and its main constituent is chromium oxide with significant contributions from iron and molybdenum oxides. However, the composition of the oxide film varies with alloying compositions within the stainless steel. The minimum chromium content of 10.5wt.%Cr is necessary for the formation of a stable oxide layer. Since the protective layer reduces the dissolution rate of the alloy elements it is usually referred to as the passive film. The significant property of stainless steels to resist corrosion is because of this surface film, and for effective protection it needs to completely cover the surface to reduce the reaction rate between the metal and the surroundings as it is non-reactive. Thus, the film hinders the electrochemical reactions from commencement or even advance. The passive film is fragile and porous, and can be removed with ease, but during construction and handling of large components it is usually removed or damaged mechanically through machining or grinding and by high thermal exposure from welding and heat treatment. When the impaired material is not maintained accordingly the corrosion properties of stainless steel may be compromised. Even though the passivation layer can be damaged to an extend that the material beneath is exposed, it is capable of naturally repairing itself if the base stainless steel is free from contaminants. When there is contamination on the stainless steel surface, chemical treatment viz. pickling and passivation are applied to the surface to remove contaminants and assist the formation of a continuous chromium oxide and or passive film [35].

2.4.1.4 Tensile stresses

Tensile stresses in engineering assemblies have detrimental effect on the structural integrity having negative effects on fatigue performance, brittle fracture and corrosion properties. The residual stresses are inherently introduced through different manufacturing processes, even though their adverse effects are mostly apparent in the weld joints [36]. Welding procedures produce residual tensile stresses through traces stress as a function of strain and temperature during heating, melting, freezing and cooling of the weldments. The distribution of these stress across a complete butt weld is demonstrated in Figure 2-12. In the welded metal high tensile stresses (σ_X) are apparent, with substantial compressive stresses in the BM necessary to resolve total stress state to zero. During welding operations softening and thermal expansion resulting from heating up of the metal due to thermal input is enough to cause plastic deformation in the BM adjacent to the molten fusion zone (FZ). Succeeding freezing and thermal contraction, the tensile stresses up to the yield stresses are produced at the weld and near the solidified weld metal. The distribution and

magnitude of the residual tensile stresses introduced through welding operations are influenced by the geometry of the structure [25].

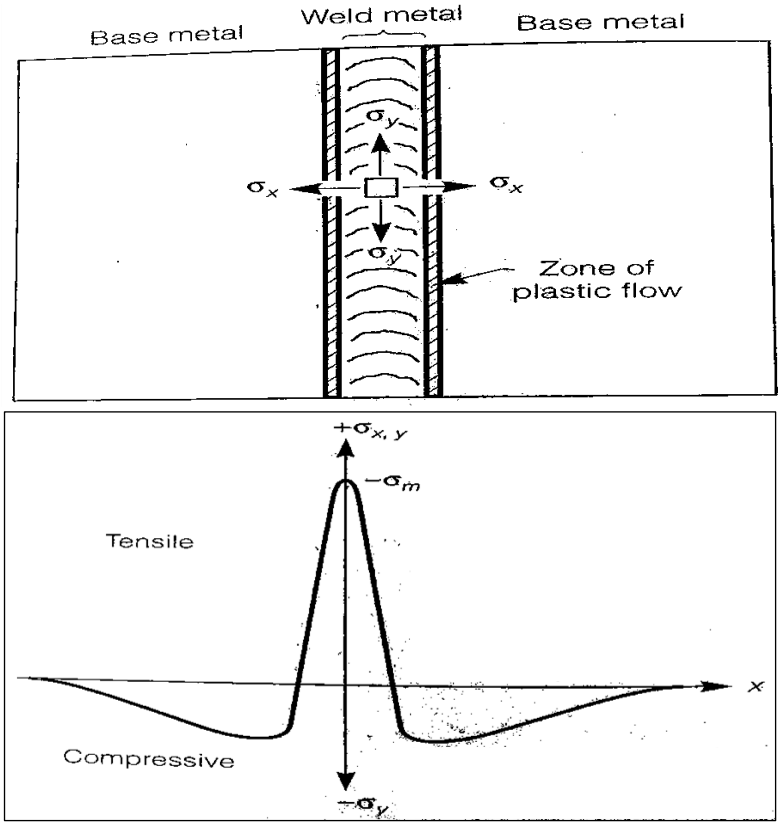

Figure 2-12: Distribution of stress across a butt weld of the two plates [25]

The residual tensile stresses introduced by means of welding practices can be appreciated as they affect SCC in transverse and longitudinal planes to the butt weldments (Figure 2-12). Welding operations produce a geometric discontinuity in the cross section, which concentrate the applied or residual stresses having the resultant SCC failures originating at the toe of the weld. The importance and the magnitude of such stresses are often underestimated, as they can have damaging consequences on the structural integrity or even catastrophic consequences if left unnoticed. High residual stresses concentration make weldments the weakest point for all forms of environmentally induced cracking, and will often lead to crack development preferentially at the regions of HAZ extending to the weld joint (FZ) [25].

2.4.2 Corrosive environment

The corrosive environment necessitates the atmosphere that can provide the electrochemical driving force for the corrosion reactions to initiate. Environmental factors that will promote the metal alloy to become prone to cracking include saline conditions at high chlorides concentrations (Cl^-), low pH or acidic conditions (H^+) and high pH or basic conditions (OH^-), high temperature surroundings, and absence or lack of oxygen etc. It is well known that the halide, particularly chlorides, owing to its presence in many environments, attacks the passive layer and can lead to local breakdown of the protective oxide film.

The temperature variable expedites the corrosion depending on type of corrosive medium that the susceptible materials are exposed, e.g. fully immersion of the material in aqueous salt solutions, acidified and or basic solutions. In aqueous salt solutions there is a synergistic relationship between the chloride concentration and the dissolved oxygen, thus when oxygen concentration is between $0.01ppm$ and $0.1ppm$ in a low to moderate chloride concentrations, it is less likely to initiate the cracks or even for the cracks to develop in austenitic alloys. In the field environment such as those near coastal regions the humidity from sea can accumulate to form the localised hostile corrosive ions of hydrogen (H^+) and chloride (Cl^-) which yields more aggressive conditions on the material surface. It is at these conditions that stainless steels can initiate cracks at room temperature and low service temperatures which are less than the temperatures required to initiate cracks when the steel is fully immersed in aqueous solutions. The chloride levels necessary to initiate cracks in austenitic stainless steels are relatively lower than $10ppm$. This is particularly true in the environments that have evaporating or concentrating mechanisms such as those having dry and wet interfaces or a film of solution in direct contact with the hot or warm surface. In these conditions the low chloride levels (3.5-5wt.%NaCl) in solution can have higher chloride concentrations and when the water is evaporated on the exposed area the REDOX reaction can advance and the corrosion indications will manifest [35].

2.4.2.1 Electrochemical/ Reduction Oxidation reactions (REDOX)

For the cracks to initiate and advance to encourage SCC progression, the corrosive exposure is one of many attributes to this failure mode in steels. The electrolyte properties to initiate SCC are the dissolved oxygen, pH, conductivity, concentrations and temperature. In aqueous solution the metal corrosion is almost always electrochemical comprising of half-cell reactions of reduction and oxidation (REDOX) reactions. In arranged electrochemical cell the metal gives up electrons to the surroundings (anode), whereas the cathode gains/accept electrons from the anode as presented by equations 6 to 11.

Anodic reaction for corroding metals:

$$M \rightarrow M^{n+} + ne^{-}$$ Equation 6 [37]

Where *n* is the number of electrons (e-) released by the metal, meaning the loss of electrons by the metal atoms (equation 6).

Rusting is a complex process. Equations 7 below demonstrate the oxidation reaction, whereby the electrons loss by iron and is oxidised to iron (II) ions:

$$Fe \rightarrow Fe^{2+} + 2e^{-}$$ Equation 7 [37]

Crucial to the formation of rust is the accompanying reduction/ oxidation (REDOX) reaction between iron and oxygen in the presence of water, see Equation 8 below representing iron (II) ions, loss of electrons and are oxidised to iron (III) ions by oxygen

$$4Fe^{2+} + O_2 \rightarrow 4Fe^{3+} + 2O^{2-}$$ Equation 8 [37]

Cathodic reactions:

Cathodic reduction reactions commonly occur in nature in neutral or basic solutions containing dissolved oxygen, illustrated by equations 9 and 10.

$$O_2 + 2H_2O + 4e^{-} \rightarrow 4OH^{-}$$ Aerated neutral to alkaline water Equation 9 [37]

$$O_2 + 4H^{+} + 4e^{-} \rightarrow 2H_2O$$ Aerated acidic solutions Equation 10 [37]

In the absence of all other cathodic reduction reactions, water can become an oxidizing agent and gains electrons as illustrated by equation 11.

$$2H_2O + 2e^{-} \rightarrow H_2 + 2OH^{-}$$ Equation 11 [37]

2.4.3 Metallurgical behavior of duplex stainless steel

Commercially produced SAF2205 has an inhomogeneous microstructure, whereby each phase has a different response to the applied stress [36]. Ferrite-δ and austenite$-\gamma$ phases have different coefficient of thermal expansion and have a phase-specific residual stresses that are introduced through quenching from the solution-annealing temperatures. The residual stresses are the resultant of micro and macro-stresses of the formed or welded metallic material, whereby the micro-stresses are of tensile nature in the austenite (γ)-phase and compressive in the ferrite (δ)-phase. These stresses are found to be higher in the transverse direction when compared to the rolling direction. Furthermore, the highest stresses are mostly found in the austenite(γ)-phase and they comprise of more complex texture since their micro-stresses increase with an increase in load in macroscopic elastic regime. The stresses become saturated during plastic deformation or dislocation motion. Following 2.5% of total plastic deformation the stresses are higher in the austenite(γ)-phase because of the complex microstructure of DSS generating heterogeneous stress distribution. The surface macro-stresses are equal in both phases (γ and δ) and they differ on a large scale when compared to material micro-stresses and their presence may affect the corrosion resistance of steels. The average stress that contributes in SCC are considered as the overall surface macro-stresses and the surface micro-stresses [2].

CHAPTER 3 : EXPERIMENTAL DESIGN AND MATERIALS

3.1 Welding protocol for AISI304 and SAF2205

The SAF2205 test plates were welded on site and the AISI304 test plates were welded by the Marine & Industrial welding specialist sourced through UCT. The test material plates of SAF2205 and AISI304 were welded using similar welding method of gas tungsten arc welding (GTAW). The two test pieces from the tested bulk material (AISI304) were sectioned to the dimensions of 150×150×24mm^3, with one plate end chamfered to a V-shape by machining the edge and the other plate was left with the flat edge. The two prepared plates were aligned ensuring that there is a joint gap size of 2mm between the flat edge and the chamfered V-shaped plate. The prepared plates were joined with a single-K-groove butt weld [Figure 3-1 (a)]. The GTAW technique was applied to seam the two plates for a high quality welded pad of 300×150×24mm^3, as presented in Figure 3-1 (a) and (b).

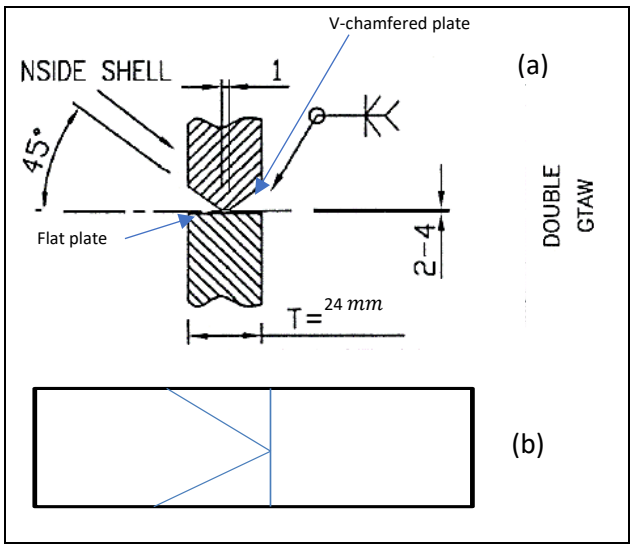

Figure 3-1: (a) Groove weldment preparation on SAF2205 and AISI304, (b) Side view for single groove and flat plate prepared for welding.

The AISI304 stainless steel plates were joined by means of the GTAW welding technique using ER 308L welding consumables, whereas the SAF2205 was welded with E2209Ti-4 filler wire. The filler metal was selected such that the chemical compositions match those of the parent metal (Table 7). During solidification of the weld pool to room temperature the regions adjacent to the FZ (HAZ and BM) consist of distinctly different microstructures [14]. In order to characterize thermal effect on the material during welding, specimens were precisely sectioned to be specifically representative of the various zones, i.e. FZ, HAZ and BM.

Table 7: Chemical composition for ER 308L filler material used to seam weld AISI304 and E2209Ti-4 used to seam SAF2205 [37].

Filler material (ER 308L) chemical composition used to weld AISI304 (wt. %)										
Elements	**Fe**	**Cr**	**Ni**	**Mo**	**Mn**	**C**	**S**	**P**	**N**	**Si**
Compositions	Bal	18.19	8.07	N/A	1.21	0.039	0.002	0.026	0.042	0.55
Typical chemical composition of E2209Ti-4 filler material for welding SAF2205 (wt.%)										
Compositions	Bal	22.671	5.156	3.041	1.802	0.023	0.01	0.0271	0.169	0.304

3.1.1 Welded plates for AISI304 specimens sectioning

Two AISI304 plates were sourced from the supplier having dimensions of (200×100×25mm^3). One plate was modified by machining to a V-shape edge at UCT workshop, while the other plate was left with flat edge. The prepared plates were welded by Marine & Industrial welding specialist. The welding protocol was completed as explained in the previous section using GTAW technique to join the two plates. The flat rectangular strip of AISI304 specimens exposed to stress corrosion cracking test, were sectioned from these welded plates ensuring that weldments is maintained in the middle of specimen as shown in Figure 3-3. The extracted specimens were modified by adjusting specimen length from 250mm to 75mm with the weld maintained in the middle for the intergranular attack testing.

3.1.2 Welded plates for SAF2205 specimens sectioning

The four of welded SAF2205 plates were cut-offs from both sides of the welded bulk material done on site. The received welded plates had dimensions of 300×60×24mm^3 were provided as shown in Figure 3-2 (a) and (b).

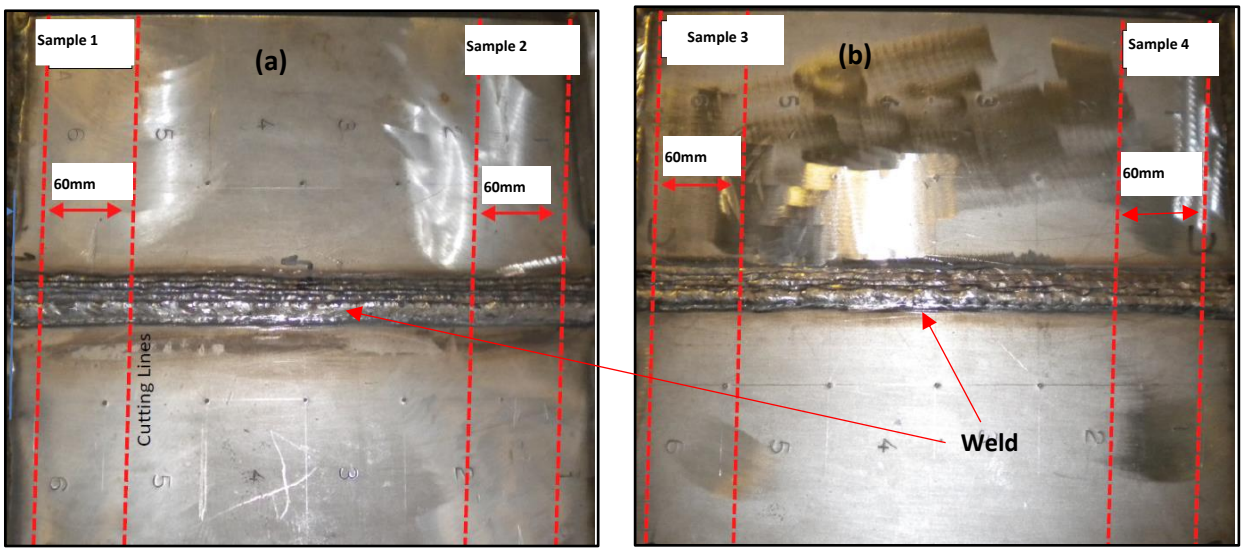

Figure 3-2: (a) Plate 1- SAF2205: 2× Samples from bulk material, (b) Plate 2 - Additional 2× welded samples of SAF2205 extracted from the bulk welded plate, sample plated received from the industry.

The SAF2205 and AISI304 specimens used for the bend-beam SCC exposure test and intergranular attack test were sectioned at the positions illustrated in Figure 3-3 from the welded plates which were further machined to the flat rectangular strip in accordance to ASTM G39 [38].

3.2 AISI304 and SAF2205 specimen matrix for stress corrosion testing

The prepared specimens used to perform SCC test in the salt spray chamber and Strauss test for intergranular corrosion attack were precisely sectioned from the welded plate joints. The geometry of the sectioned flat rectangular specimen's was intended that it is easy to handle when it is affixed on to the specimen holder and it also encompasses the mimicked welded material conditions at the weld zones (FZ, HAZ and BM) such as those experienced on site or field.

3.2.1 Corrosion specimen's matrix and material conditions

The specimen's geometry used for cyclic corrosion test and intergranular corrosion attack test permits that the bending moments are imposed directly at the welded region of the bend-beam. The specimens were sectioned with excess thickness of $\pm 0.04mm$ using the WEBM-HS wire cutting machine at UCT machine workshop. The extra specimen thickness allowed the removal of the ripple effect and uneven surface caused by the wire cutter through grinding without damaging the specimens, but to obtain smooth surface finish that is within tolerance of the specification (ASTM G39). Each specimens were labelled as SAF2205 or AISI304 as well their heat treatment conditions of 500℃/3h, 800℃/2h, as-received BM and as-weld (Table 8). The specimens were also labelled with dates for traceability during salt chamber cyclic corrosion testing and for intergranular attack testing.

Table 8: Bend beam test specimen matrix for welded AISI304 and SAF2205 stainless steel grades

AISI304			
No. of specimens for as-received BM	No. of specimens for as-weld	No. of specimens for PWHT at 500℃/3h	No. of specimens for PWHT at 800℃/2h
3	3	3	3
Tested No. of AISI304 specimens for SCC exposure			**12**
SAF2205			
3	3	3	3
Total No. of SAF2205 specimens for SCC exposure			**12**

The sectioned specimens from the welded plates (Figure 3-3), with the specimens' geometry specified in Appendixes B: Figure 7-1, were mounted on the AISI304 and SAF2205 specimens holders shown in Appendixes B: Figure 7-3 and Figure 7-4 respectively. The mounted bend specimens were exposed to the cyclic corrosion test in conditions in the salt chamber. The specimen mount was designed using non-conductive material to prevent galvanic corrosion from occurring (ASTM G-39) [38]. Similarly, the specimens used for the intergranular test were cut from the same position with the different specimen's dimensions illustrated in Appendixes B:Figure 7-2.

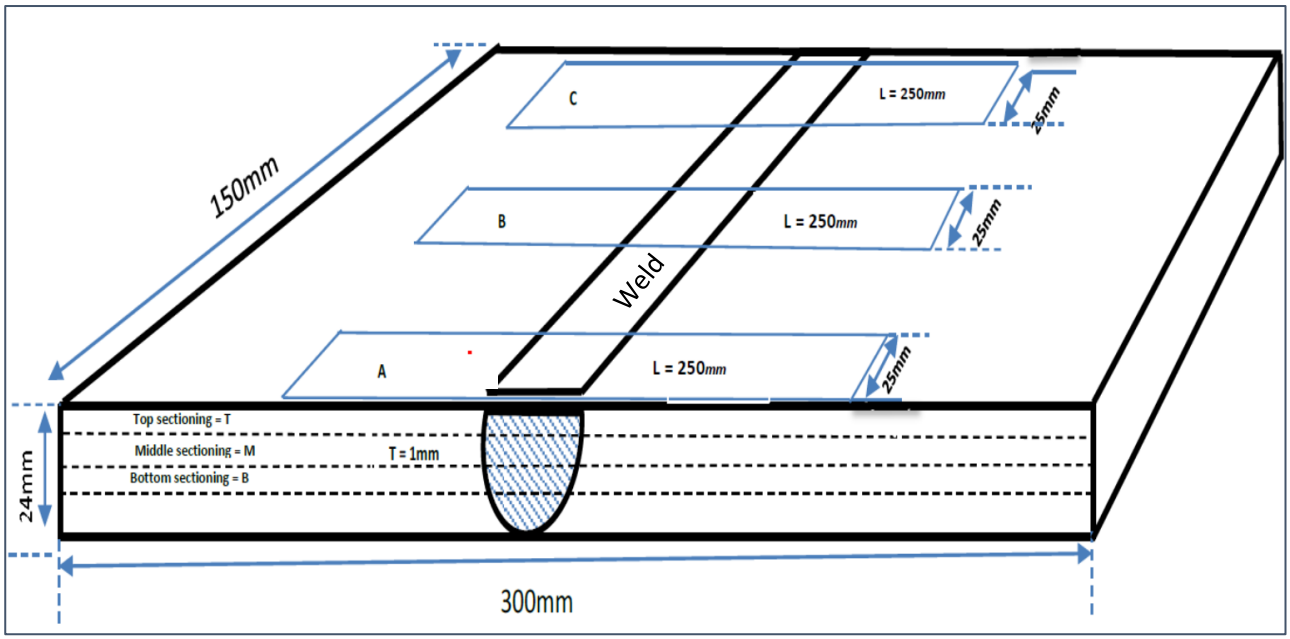

Figure 3-3: The orientation and the location of the sectioned bend-beam specimens at the positions marked "A", "B" and "C" at the top: T, middle: M and bottom: B.

One side of each test specimen was initially surface ground at the UCT workshop to remove the uneven ripple effect with the opposite side left without grinding. The specimens were further hand grounded using silicon carbide (SiC) abrasive paper of sizes; 220grit, 500grit, 800grit and 1200grit

progressively until the surface was free from flaws. The final rinse off usingr water followed by ethanol (C_2H_5OH) to remove the remaining minute residue and for speedy dry off using an air blow dryer to prepare for the hand polishing step was done. The manual polishing was accomplished by applying diamond based polishing paste containing a monocrystalline diamond suspension and lubricants in the order of $9\mu m$, $6\mu m$, and $3\mu m$. The specimens that did not require further heat treatment were coated on one side (non-polished side) using Neoprene water proof polymer-based paint and labelled accordingly (Table 8). The opposite side (polished side) was left unpainted so that the electrolyte can interact with the prepared surface during the SCC exposure test [Figure 3-4 (a) and (b)].

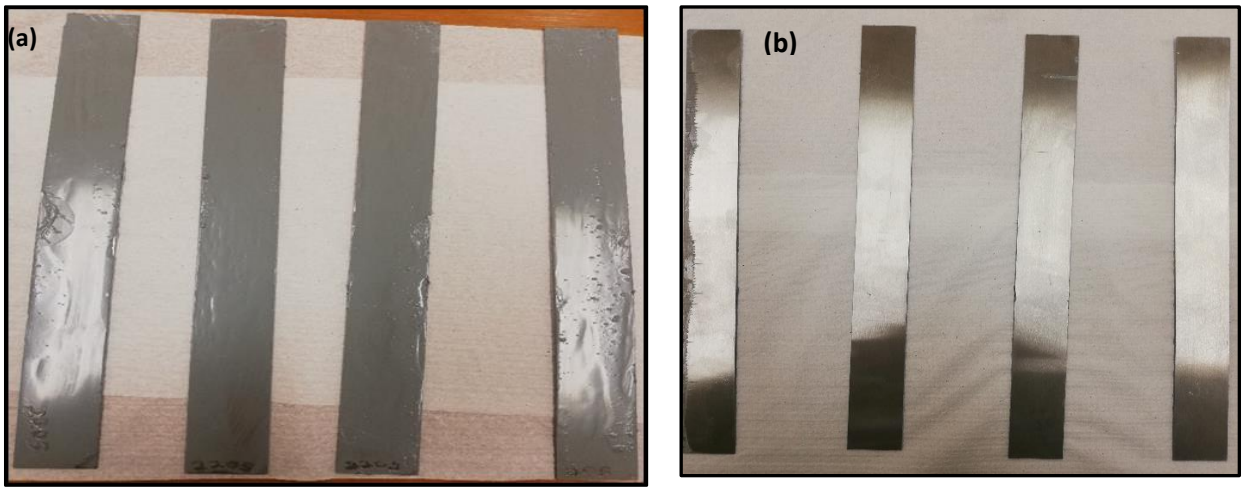

Figure 3-4: (a) One sided neoprene painted specimens, (b) One sided unpainted for exposure prior ready for mounting on to the specimen holder

3.3 Heat treatment to accelerate deleterious intermetallic phases and carbides at the HAZ of tested stainless steel grades

To achieve adequate stress relief in AISI304 grade, the material is heat treated at temperatures between 425℃ and 925℃. When high temperatures of $\pm$870℃ are applied for heat treatment about 85% of the residual stresses are relieved. However, the $M_{23}C_6$ precipitation at the grain boundaries, thereby resulting in sensitization that severely impairs corrosion resistance properties at the areas affected by heating i.e. near the weld regions (HAZ). Heating of austenitic stainless steels to lower temperatures of 425−550℃ is preferred because the precipitation of $M_{23}C_6$ is very slow. Slow diffusion due to these temperature conditions enables material to be heated for several hours without sensitisation occurring [39]. This treatment may not be very efficient in reducing residual stresses of the welded material [12].

The SAF2205 grade comprises of austenite-γ and ferrite-δ matrix which suffers from decomposition process during isothermal aging within the critical temperature range of 650–950℃ resulting in the precipitation of secondary phases. The formed secondary phases are known to be deleterious to

corrosion attack of the duplex stainless steels, since they are considerably enriched in chromium. The heat treatment schedule to accelerate these detrimental phases in SAF2205 stainless steel is as tabulated in Table 9. Likewise, the procedure to complete the heat treatment to emphasize the detrimental secondary phases in the weldments of SAF2205 and AISI304 specimens are similar, see Table 9.

3.3.1 Sensitisation post weld heat treatment for AISI304 and SAF2205

The detrimental precipitates and secondary phases of the studied materials were exaggerated as per heat treatment schedule tabulated in Table 9. The post weld heat treatment (PWHT) of 800℃ for 2 hours and 500℃ for 3 hours was carried out on the rectangular thin strip specimens prepared from the welded plates. Prior to the heat treatment specimens were coated with spirit-based coating (Foseco-Isomol 100) on the prepared side and they were left for ±30minutes to dry up. The coating was applied to minimise the oxidation on the exposed specimens' surface during the high temperature heat treatment. The K-type thermocouples were attached to uncoated side to read the actual specimens' temperature rather than the furnace temperature [Figure 3-5 (a) and (b)].

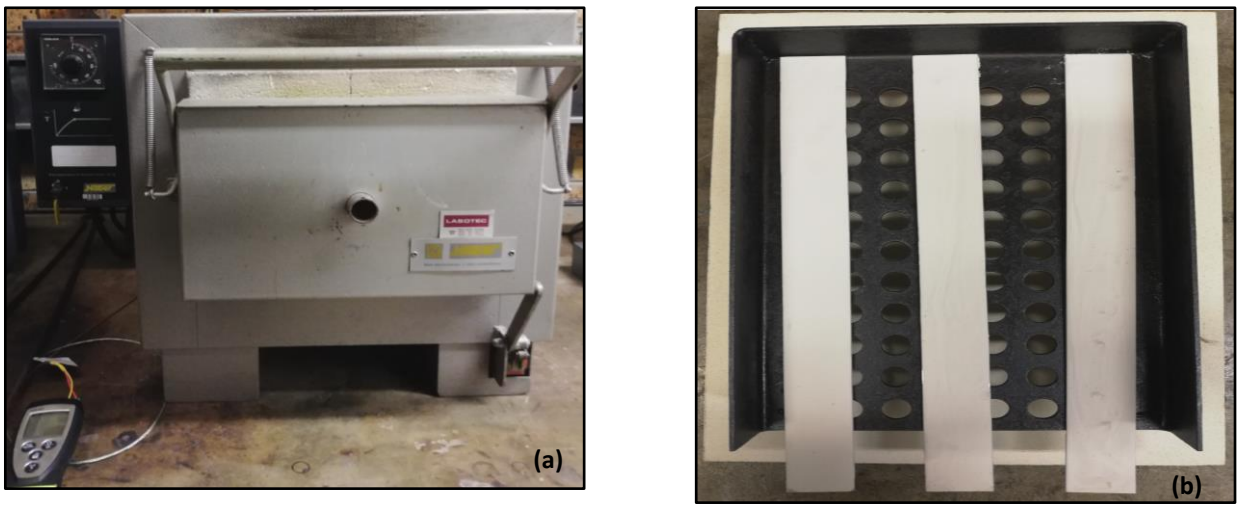

Figure 3-5: (a) Naber industriofenbau D-2804 Lilienthal/ Bremen furnace equiped with external thermocouple and (b) Specimen batch coated with Faseco Isomol 100 ready for heat treatment.

The electric box furnace was preheated to achieve the heat treatment temperatures of 800℃ and 500℃ before placing the coated specimens inside. Timing of the PWHT durations of 2 and 3 hours (Table 9) was done when the heated specimens attained the required temperature. The PWHT was completed by heating the specimens of AISI304 and SAF2205 in batches of three at a time [Figure 3-5 (b)]. The heat-treated specimens were removed from the furnace and air cooled to room temperature by exposing them to atmospheric conditions for 24 hours before they were cleaned to remove the coating and any deposited oxide layer to prepare for the SCC exposure test in the Q-FOG salt chamber.

Table 9: Heat treatment schedule to exaggerate the detrimental intermetallics and carbides in the welded AISI304 and SAF2205 specimens

Heat treatment to exaggerate the carbides precipitate in AISI304 HAZ		
Heat treatment Temperature (℃)	Heat treatment Duration (Hours)	Sample cooling medium
800	2	Air
500	3	Air
Heat treatment to exaggerate the precipitation of deleterious secondary phases (σ-phase and χ-phase) in SAF2205 HAZ		
800	2	Air
500	3	Air

3.4 Strain gauge installation, preparation and handling

The strain gauge of type, KFC-20-C1-11, having thermal output of 1.8$\mu\varepsilon/$℃ and resistance of 120Ω was used to measure the strain imposed to AISI304 and SAF2205 specimens. The initial specimen surface preparation was done by grinding and polishing before the strain gauge was installed. For the strain gauge to adhere perfectly on to the specimen weldments the bonding area was kept clean by wiping the surface repeatedly after it was rinsed with ethanol solution until there was no trace of grease or debris detected on the gauze sponge and thus ready for the gauge installation. The strain gauge was carefully removed from the acetate envelope by holding the edge of the gauge backing with tweezers and placing it on a glass plate. M-line PCT–2A cellophane tape ($\pm 120mm$) was used to handle and lift the strain gauge from the glass plate without damage. This was done by lifting the cellophane tape at an angle of approximately $40°$ ensuring that the gauge-terminals are intact with the gauge. The markings on the gauge were accurately aligned with the marked specimen centreline at the weld. The M-Bond 200 catalyst was applied to speed up the adhesive bonding between the strain gauge and the specimens. The gauge was then attached by single stroke wiping over the taped gauge using the gauze sponge, followed by applying thumb pressure to the gauge and the terminal area to warmup the adhesion for quick drying before the tape was removed.

3.4.1 Electrical wire connection to the strain gauge

The strain gauge grid was protected by covering with drafting tape thereby exposing only the solder tabs or terminal. By using a soldering pencil, the resin-core solder wire was placed flat on the strain gauge tab and pressed firmly with the tinned hot soldering tip adding $\pm 3mm$ solder at the edge of the tip. The soldering pencil was lifted to complete soldering at the terminals by progressive deposit of the solder mound. The electric wires were separated by approximately $20mm$ and the insulation was stripped off ($13mm$) on both ends of the electrical wires (Red→positive and Black→negative) and twisted. The twisting action was done to coalesce the loose wires so that they are easily soldered with the strain gauge terminals. The soldering of terminals was completed in accordance with ASTM E123 [40]. The soldered terminals were finally cleaned with solvent and soft brush to remove residual flux.

3.4.2 Determination of specimen bend angle and specimen holder design

The studied materials were prepared in accordance with ASTM-E1237 [41] to install the strain gauge at the bend weldments. The strain gauge approach to bend the specimen to reach the calculated elastic strain limit so that the metal is prepared for cyclic corrosion test inside the salt chamber at a stress level just below the yield stress was carried out. The flat rectangular specimens were bend so that it is fixed on the specimen holder span and to create stresses at the apex that are below yield stresses. The specimen flexing was determined experimentally by obtaining the yield strain, demonstrated in Figure 3-9 and Figure 3-10, that it matches the calculated yield strain (Table 10). The actual yield strains for SAF2205 and AISI2304 specimens were obtained by applying the Young's Modulus relationship (Equation 12). The actual yield stress (σ_y) for the tested materials was obtained from the stress-strain relationship (Figure 3-7: SAF2205 and Figure 3-8: AISI304) through application of tensile testing technique explained in § 3.4.2.1–3 below. The measured strain was accomplished by means of trial and error method through manipulating the degree of bending without overbending the specimens beyond the materials yield stress (σ_y). See the experimental setup for measuring the yield strain presented in Figure 3-9 and Figure 3-10

3.4.2.1 Tensile test

Tensile tests were completed at the Centre of Materials Engineering (CME) laboratory, University of Cape Town (UCT) using Zwick universal 1484 tensile test machine equipped with load cells [Figure 3-6 (a)]. Constant strain rate of $1 \times 10^{-3} s^{-1}$ was applied to pull round dog-bone tensile test specimen depicted in [Figure 3-6 (b) and (c)] and the specimen geometry specified in Appendix B: Figure 7-5 [42].

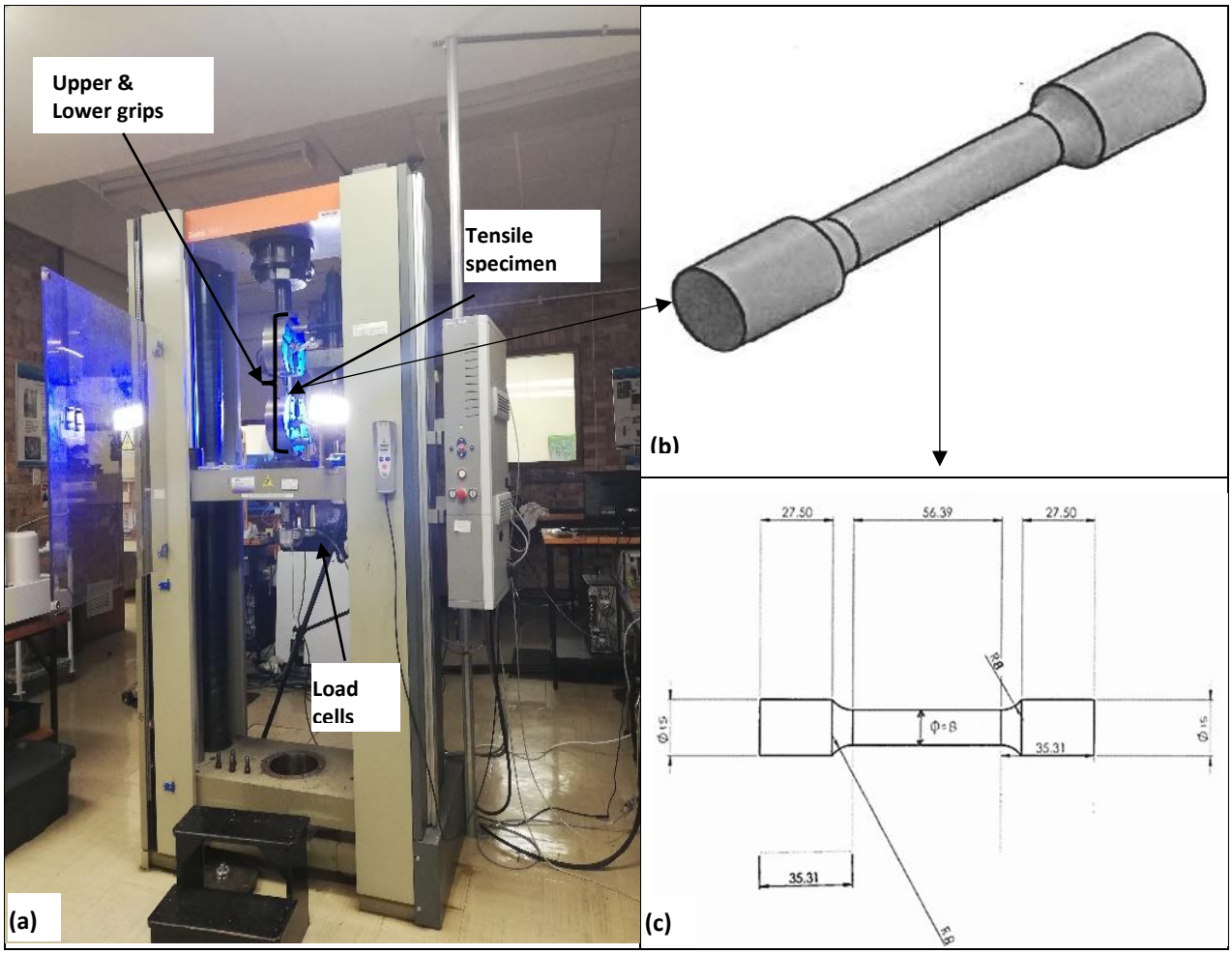

Figure 3-6: (a) Zwick universal 1484 tensile testing machine at UCT, CME laboratory, (b) Tension test specimen, (c) Dog-bone shaped tension test specimen geometry

3.4.2.2 SAF2205 materials yield strain determination

Five tensile test specimens of SAF2205 were machined and tested to the obtain the stress versus strain relationship presented in Figure 3-7 .

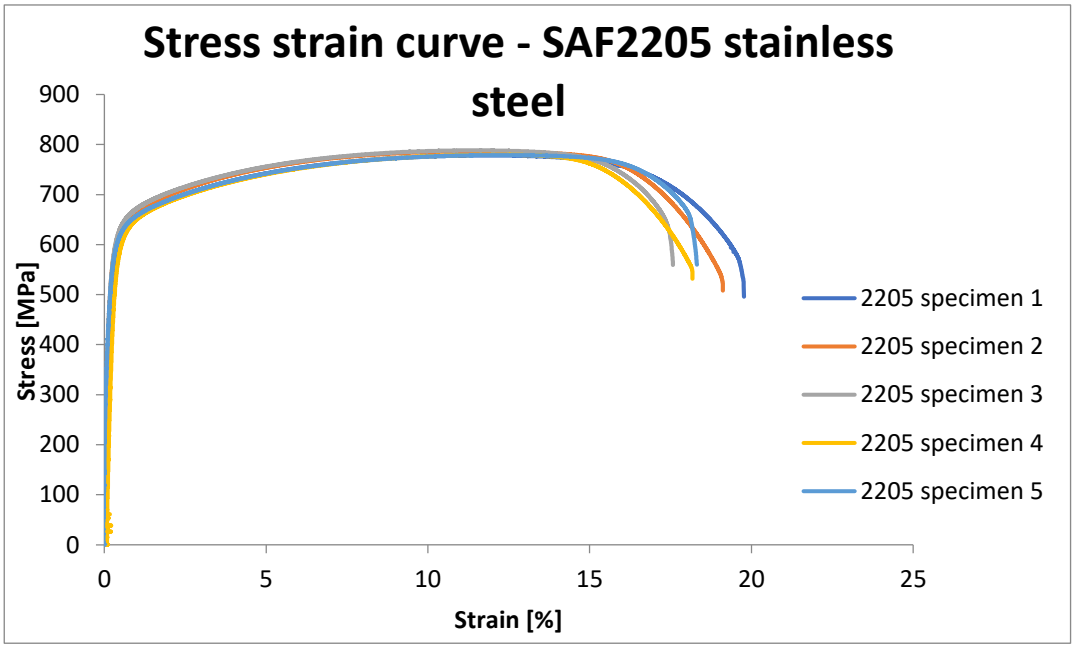

Figure 3-7: Combined stress-strain curve for the tested five SAF2205 specimens

The tested SAF2205 specimens followed the expected stress-strain trend shown in Figure 3-7 demonstrating similar behaviour with no outlier. The experimental UTS for SAF2205 material was measured at ±770MPa which was slightly higher than the UTS values from Material Certification (745MPa), but still within the expected UTS range of this material. The experimental YS was measured to between 475–600MPa due to the continues nature of yielding in the duplex steel, which was slightly higher than the YS values from SAF2205 grade Material Test Certificate (460–581MPa), see Appendix C: Table C-1 [43]. The SAF2205 demonstrated high ductility and high strength (Figure 3-7), so severe forming operations such as cold heading are generally possible. The ductility of SAF2205 is less than that of AISI304 grade (Figure 3-8).

3.4.2.3 AISI304 material yield strain determination

Tension test were completed using five representative standard dog bone shaped samples of AISI304. Two of five the dog bone specimens were tested successfully, with their tension test results presented on the same stress-strain axes shown in Figure 3-8 below. Tensile test results of the remaining three specimens were disregarded as their stress–strain plot was not according to the expected AISI304 stress-strain trends. This was due to the flawed sample gripping mechanism that kept slipping when the force was applied to displace the specimen to its breaking point. The

mechanical wedge action tensile grip was dismantled and cleaned at the UCT mechanical workshop to improve their gripping capabilities. The improved gripping mechanism resulted in attaining tensile properties of two of the five AISI304 tensile specimens, with their stress-strain relationships shown in Figure 3-8 below.

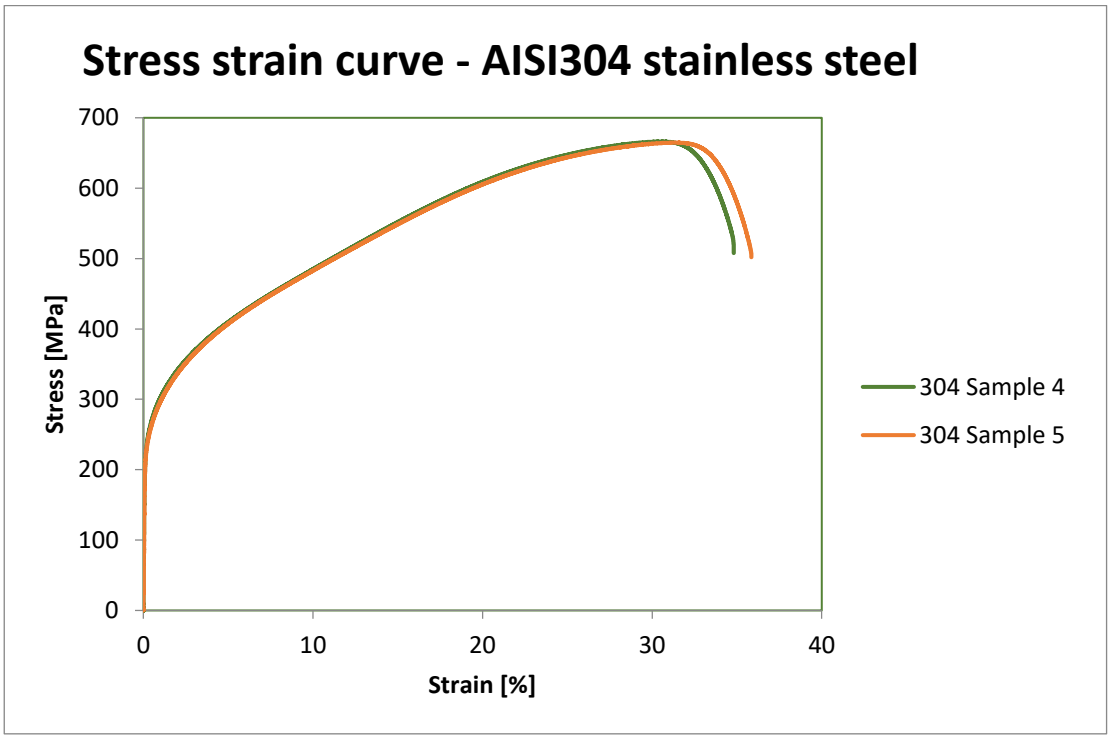

Figure 3-8: Combined stress-strain curve for two AISI304 samples 4 and 5

The stress–strain plots for the two AISI304 samples 4 and 5, which were successfully tested without flaws trended as expected following AISI304 stress versus strain trends. The UTS for AISI304 specimens was measured to be 663MPa (Figure 3-8), which was higher than the standard UTS of 515MPa. The measured YS of $\pm$250MPa was also higher than the standard YS value of 205MPa, as shown in Appendix C: Table C-2.1 [43]**.**

Tensile yield properties for the evaluated materials clearly demonstrate higher strengths for SAF2205 grade at 600MPa, which is more than twice that of AISI304 grade with the measured yield strength of 250MPa. The stress–strain relationship for AISI304 grade demonstrated high ductility of this material in comparison to SAF2205 grade. Conclusively both material grades of SAF2205 and AISI304 possess excellent mechanical properties which are attractive for design engineering.

3.4.2.4 The elastic tensile strain calculations for AISI304 and SAF2205 materials

The elastic tensile strain(ε_y) was calculated to determine the maximum elastic stress that can be reached to avoid plastic deformation of the weld located at the apex of the bend test specimen.

Through the application of the Young's Modulus relationship (Equation 12), the elastic tensile strain for both tested materials are shown in Table 10 below.

Table 10: Calculation of yield strain ($\boldsymbol{\varepsilon_y}$) for AISI304 and SAF2205 stainless steels

Young Modulus relationship: $\varepsilon_y = \frac{\sigma_y}{E}$ Equation 12 Where: ε_y = Yield strain (Dimensionless) E = Modulus of elasticity (GPa) σ_y = Yield strength (MPa)	
AISI304	**SAF2205**
$\sigma_{y(AISI304)}$ = 241MPa E = 193GPa =193000MPa [44]	$\sigma_{y(SAF2205)}$ = 470MPa E = 200GPa = 200000MPa [44]
From equation 12 the calculated value of $\varepsilon_{y(AISI304)}$: $\varepsilon_{y(AISI304)} = \frac{241\text{MPa}}{193000\text{MPa}} = 0.001249$ $\varepsilon_{y(AISI304)} = 0.001249 \times 1000000$ $\varepsilon_{y(AISI304)} = 1249\mu strain$	From equation 12 the calculated value of $\varepsilon_{y(SAF2205)}$: $\varepsilon_{y(SAF2205)} = \frac{470\text{MPa}}{200000\text{MPa}} = 0.00235$ $\varepsilon_{y(SAF2205)} = 0.00235 \times 1000000$ $\varepsilon_{y(SAF2205)} = 2350\mu strain$

3.4.3 Strain gauge approach for bending AISI304 and SAF2205 specimens

In order to bend the flat strip specimens of AISI304 and SAF2205 to reach the calculated elastic strain, the specimens were positioned on top of the adjustable stressing jig, which was then flexed to create a bend or an arch with the weldment experiencing more stress at the apex of the formed arched. The measured strain values corresponding to the degree of bending was confirmed to correspond to the calculated strain (ε_y) obtained in Table 10 for each of the tested material. The distance from both ends of the bent specimen or the sides of the bending jig where specimens are supported, was measured using a Vernier callipers to measure the length for the holder span design (H in mm) to securely support the mounted specimen and thus maintaining the measured strain. This was accomplished by bending the specimens to reach the calculated elastic strain values at 1249$\mu strain$ and 2350$\mu strain$ for AISI304 ($\varepsilon_{yAISI304}$) and SAF2205 ($\varepsilon_{ySAF2205}$) respectively. Specimen bending was cautiously done to prevent the material from plastic deformation allowing the specimens to spring back to zero strain or to its original flat shape when the strain is released. The experimental set up for the strain measurement is presented in Figure 3-9, showing mounted specimens with strain gauges affixed at the centreline prior to placing the

unit on top of the stressing jig. Figure 3-10 displays the assembled strain gauge unit connected to HBM sensors connected to Catman software used for data acquisition, and the computer monitor to display the measured yield strain.

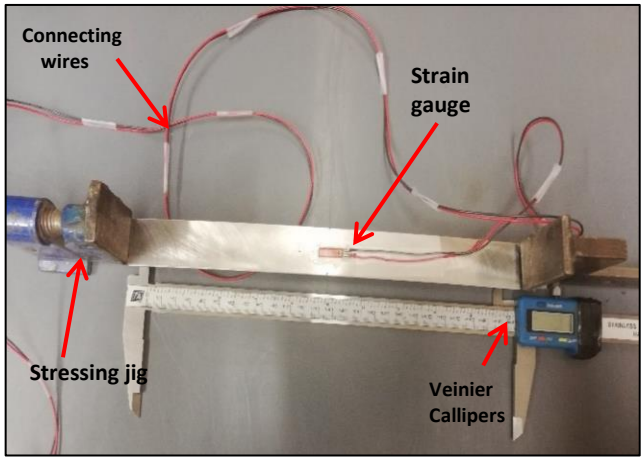

Figure 3-9: Stressing jig equipped with stressing lever for bending the specimen attached to strain gauge.

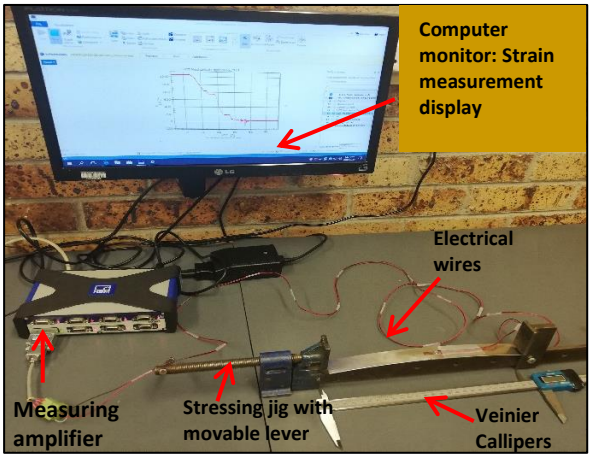

Figure 3-10: General set up for strain measurement test.

3.4.4 Holder/mount design for AISI304 and SAF2205 specimens

The specimen holder was designed in accordance with ASTM G39, whereby the holder span (H) measurements were attained from the strain test by measuring the distance between the two ends of the arched specimens without yielding, and simultaneously measuring the actual strain. The holder span design values for AISI304 and SAF2205 where attained as follows; $\mathrm{H}_{AISI304}$ at 248mm and $\mathrm{H}_{SAF2205}$ at 244mm. The holder span measurements were attained using a flat specimen of original length (L_o of 250mm) and bent at a distance of 2mm and 6mm ($L_o - H$) to create an arch with a desired yield strain for ISI304 and SAF2205 specimens respectively (Figure 3-11). The actual holder span measurements ($\mathrm{H}_{AISI304}$and $\mathrm{H}_{SAF2205}$) are presented in appendix A-Table **19**. To maintain the stress within the elastic limit of the tested materials, the relationship between the original specimen lengths (L_o) and the distance between the holder span supports (H) was kept within the limitations of 0.01 and 0.5 as specified in ASTM G39, see appendix A (b).

3.4.5 The assembly of bent beam specimens in the holder

The specimens were successfully mounted on the holder span by means of bending into an arch shape securely supported by two side frames [Figure 3-11 (a) and (b)]. The arch shape creates a bending moment associated with tensile stress on the outer radius or apex of the bent specimen. The stress developed varies from zero at the outer supports to a maximum at the centre of the weldment. The two-end support-frame that are perpendicular to the base of holder span were

designed to be $4mm$ high at 90°[Figure 3-11 (a) and (b)], which tightly holds the arched specimen in to position and maintaining the stress within the elastic region. It was equally important that the material selection for the holder design is non-conductive to inhibit different modes of corrosion such as galvanic corrosion from taking place [38]. Polyvinyl Chloride of PVCSG252000100 material was used to fabricate the specimen holder to eliminate the probability of galvanic corrosion.

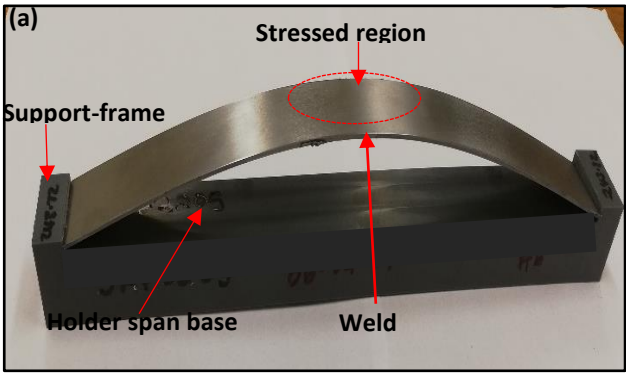

Figure 3-11: (a) Bent beam loading frame with the loaded sample.

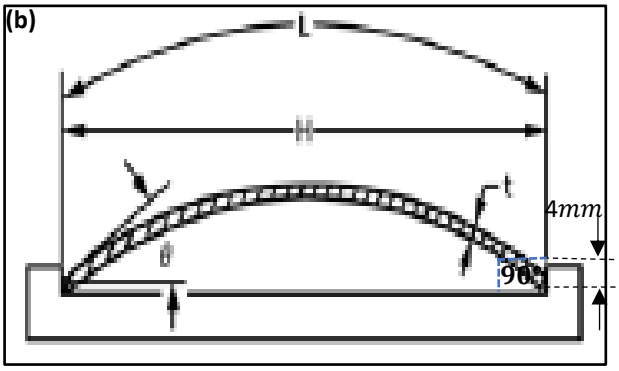

(b) Schematic of bent beam specimen – ASTM G39-99 [38].

A total of forty specimens with twenty of each of the test materials (AISI304 and SAF2205) were machined and surface ground to adjust to the specimens' geometry profile (Appendix B: Figure 7-1). Twelve of the twenty specimens from each of test material set were exposed to the salt chamber for cyclic corrosion testing conditions, with the remaining eight specimens used for testing for intergranular corrosion attack. Each of the twenty four (twelve of each tested material) prepared specimens were mounted on to the specific designed holder to maintain the stressed region in the mid-length of the mounted specimen as illustrated in [Figure 3-11 (a) and (b)]. The specimens were carefully inserted into the holder span so that it does not deform permanently.

3.5 Corrosion test environment

There is a wide range of test methods available to investigate the physical and corrosion behaviour of stainless steels. Accelerated laboratory tests are useful for a constrained period to perform corrosion tests, since they are relatively fast in availing results and reproducing data. These testing techniques are also preferred because numerous specimens of similar and or different properties can be tested simultaneously without affecting the other. Two different test approach were used, namely exposure in a salt spray chamber and short-term immersion using the Strauss test.

3.5.1 Salt spray chamber corrosion test method

The salt spray-test process is one of many accelerated corrosion experimentation techniques that provide controlled laboratory corrosive conditions used to produce relative corrosion information for metallic specimens exposed to harsh conditions in the test chamber [45]. Traditional salt spray exposure test practice specifies combination of functions automated to exaggerate the conditions experienced in the field or on-site using salt spray (Q-FOG) apparatus-ASTM B117.
The Q-FOG cyclic corrosion tester was programmed to continuously operate for the duration of the test with the only human intervention being to refill the salt solution when the tank is at low level. Under normal environmental exposure, stainless steels may take many years before any type of corrosion manifests. Thus, in order to expedite corrosion, it is important to design and or select the programme on the Q-FOG cyclic corrosion tester that will mimic the desired corrosive conditions producing corrosion failure mode that simulates those of exposing stainless steel to the marine environment [45]. The specimen's exposure test was an ongoing process until the test was terminated only when the indications of corrosion failures were confirmed.

3.5.2 Procedure for accelerated exposure using Q-FOG Cyclic Corrosion Tester

The Q-FOG salt spray chamber was operated in a continuous cyclic mode of varying operating conditions which were automated to simulate the marine conditions. The tests were carried out using a sodium chloride solution at 5w.t%NaCl concentration as stipulated in ASTM B117-18 [45]. Since the actual atmospheric exposures typically comprise of wet, dry and humid conditions it was necessary to mimic these conditions upon which the pre-programmed machine mode of CCT-1 was selected from the Q-FOG salt spray chamber control panel. The CCT-1 mode was previously specified by Japanese automotive manufacturers which used to test corrosion for the car body parts in saline surroundings [46]. The exposure conditions specify the use of 5wt.%NaCl, at the exposure cycles alternating at various temperatures i.e. 35℃, 40℃, 50℃ and 60℃ and different duration. The CCT-1 programmed cycles (x4) are presented in the flow diagram in Figure 3-12 and § 3.5.2.1-8 below.

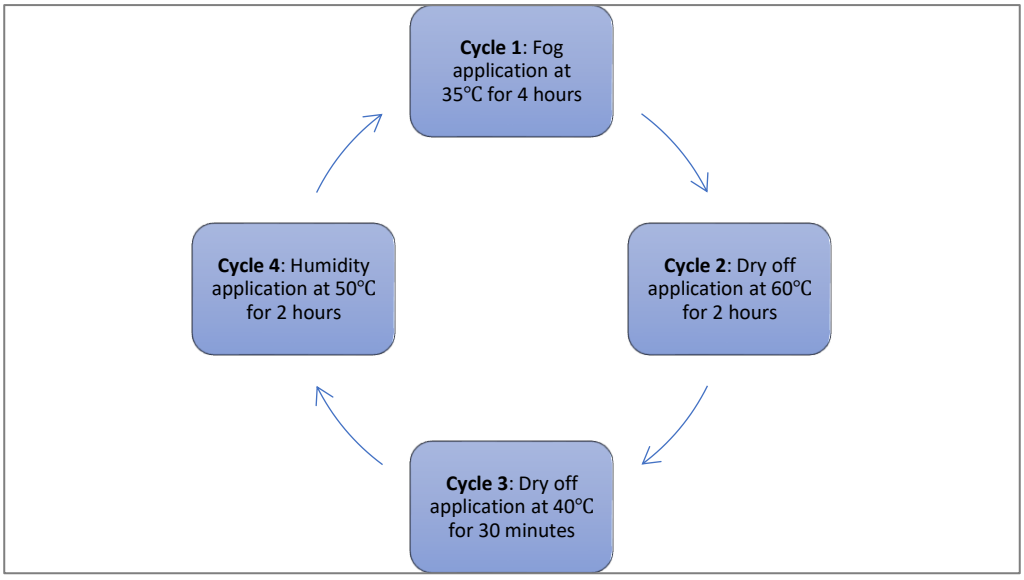

Figure 3-12:Q-FOG salt chamber exposure conditions and durations

The cycles for the CCT-1 functions were programmed to alternate between the application of fog, humidity and dry off at two different temperatures. When the cycles set duration elapse they were repeated by resetting the timer to the desired duration in days. The cyclic corrosion test was carried out continuously for a period of 10 months.

3.5.2.1 Cycle 1: 4 hours of salt fog application at 35°C

The Q-FOG CCT-1 functions are configured such that the salt solution contained in the tank is transferred into the chamber via a spray nozzle. The solution is atomised by mixing with compressed air at the outlet nozzle to form fine brine mist which is distributed evenly throughout the chamber by diffusers. The atomizing air is saturated with water vapour from a boiler or vaporiser, fed from a Reverse Osmosis (RO) water unit (Figure 3-13). Potable water from the municipality is purified before supplied to the boiler fed from the RO unit.

Temperature (35°C) required for the fog application is maintained by heaters situated at the bottom of the chamber (Figure 3-14). Likewise, temperature requirements for the mist, dry-off and humid application is controlled by the heater in the salt chamber that is at a pre-set temperature. The solution flow rate is controlled by pump speed also at a set point, programmed from Q-FOG CCT salt spray machine control panel.

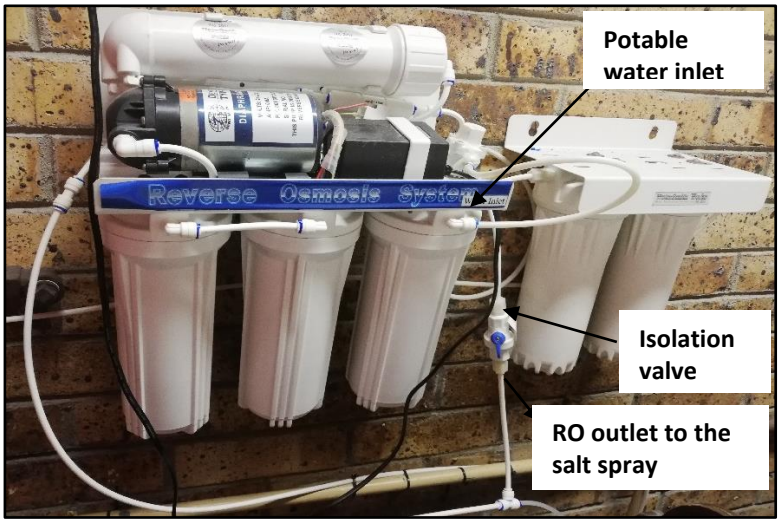

Figure 3-13: RO system to produce purified water used in the Q-FOG CCT-1 salt spray chamber

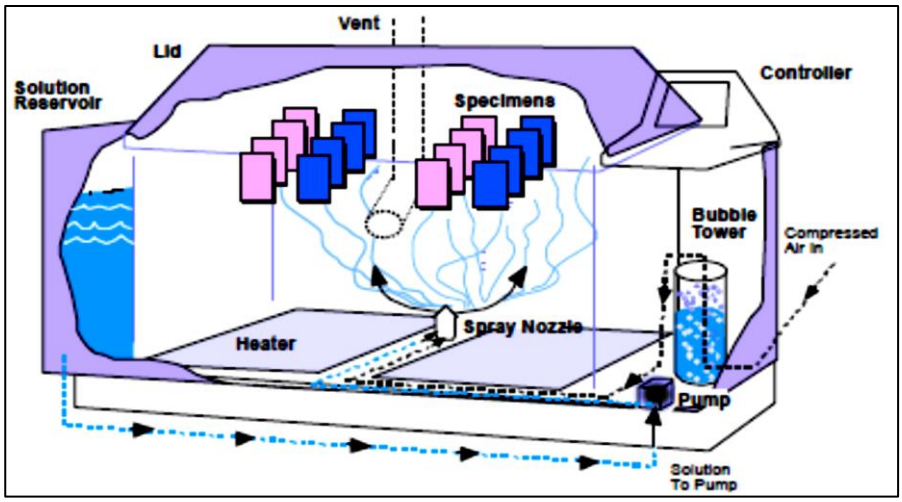

Figure 3-14: System flow configuration for the Q-FOG CCT-1 [47]

3.5.2.2 Cycle 2: dry-off air applied at 60℃ for 2 hours

Following Cycle 1 for salt fog application, the dry-off function during cycle 2 is activated for 2 hours. The dry-off function configuration is through the activation of air blowers and the fans equipped with filters sucking air from the atmosphere (in the room) into the chamber. Dry off temperature of up to 60℃ is maintained by air heaters and chamber heaters. The heaters are automatically activated to provide the heating function of inlet air from the atmosphere to the chamber via blowers. The heated air is evenly distributed to the specimens through the diffusers, situated above the chamber heaters. The Q-FOG unit configured for dry-off function is depicted in Figure 3-15 below.

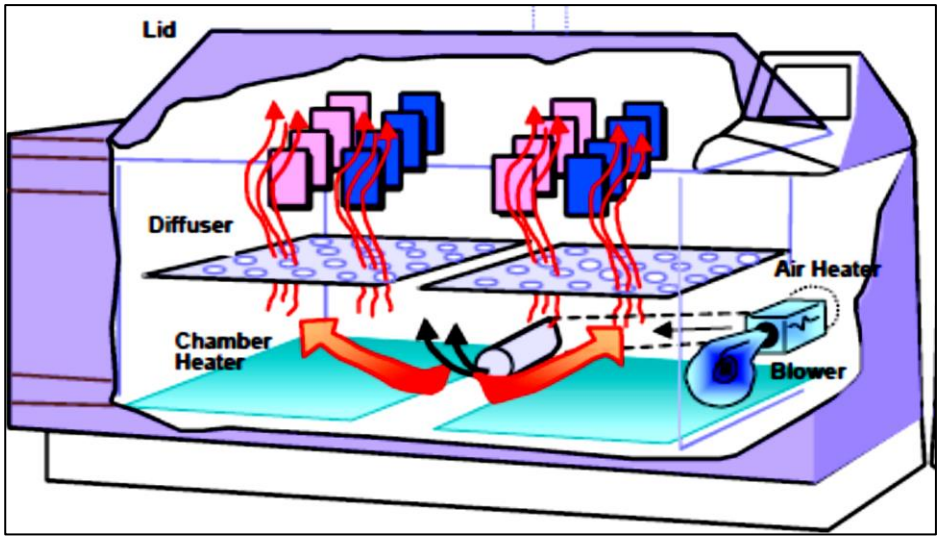

Figure 3-15: Q-FOG CCT-1-unit configuration during dry-off function [47]

3.5.2.3 Cycle 3: 30 minutes dry-off application at 40℃

Cycle 3 has a similar function as cycle 2 of drying off the chamber by sucking air from the room with the fans and blowing into the chamber via heaters. The hot air provides the dry off function in cycle 3 is similar to that of cycle 2. The difference is the heated air temperature in cycle 3 is maintained at 40℃ by the air heater and chamber heaters located at the bottom of the Q-FOG unit. The dry off function is held for 30 minutes, with operational configuration as presented in Figure 3-15.

3.5.2.4 Cycle 4: 2 hours humidity at 50℃ and RH greater than 95%

The purified water produced by the RO unit is fed into the Q-FOG machine vapour generator or boiler creating steam that is maintained at 100% Relative Humidity (RH) in the salt chamber. The diffusers distribute the humidity to the entire chamber which it is uniformly deposited on to the specimens. The secondary function of the vapour generator heaters is to maintain the chamber temperature at 50℃. The operational configuration for cycle 4 is presented in Figure 3-16 below.

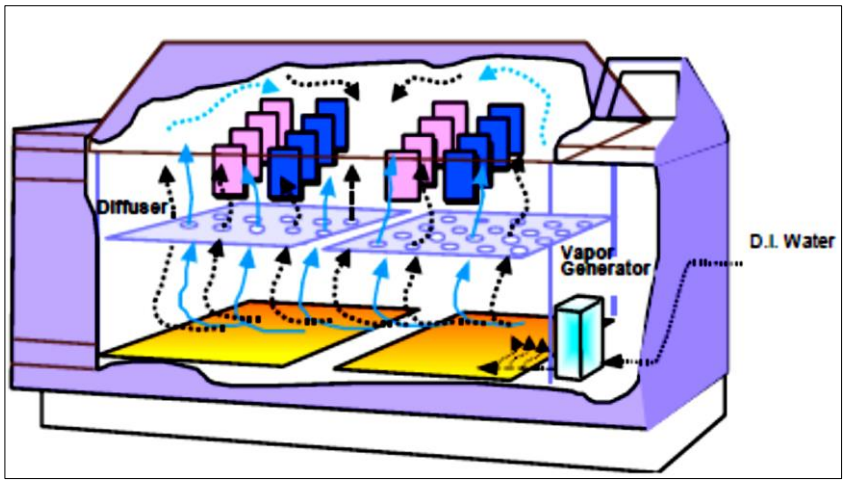

Figure 3-16: The Q-FOG CCT system configuration for the humidity function [47]

3.5.2.5 Repeating all the CCT-1 cycles

The CCT-1 programmed cycles - 1 to 4, were repeated for 10 months until corrosion indications or corrosion become evident during periodic inspections. The images of the inspected specimens were taken and logged for the duration of exposure period except for weekends and public holidays.

3.5.2.6 Arrangement of test specimens inside the Q-FOG salt chamber

Test specimens mounted on the PVC specimen holders were placed on the solid fibre-reinforced plastic support situated above the diffusers enabling greater dispersion of the fog, humidity and the hot air produced by Q-FOG machine. Specimen arrangement in the salt chamber depicted in Figure 3-17 permits the exposure conditions to be evenly distributed so that the corrosive medium can interact with the specimens without restrictions. The exposed SAF2205 and AISI304 specimens are separately arranged on the racks to prevent any means of contamination or unintended corrosion to manifest, and for the ease of sample identification during the inspections.

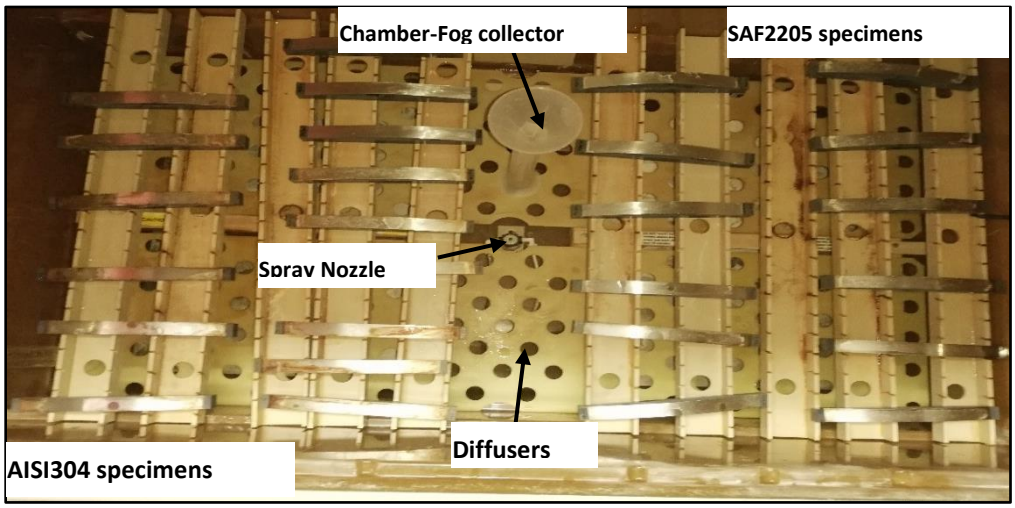

Figure 3-17: Bent-Beam specimen arrangement inside the Q-FOG salt chamber racks

3.5.2.7 Atomization and quantity of fog by means of fog collection procedure

The uniform distribution of the fog and the humidity throughout the chamber is beneficial for the specimen exposure consistency and for corrosion results that represent the exposure conditions. Two fog collectors were strategically positioned in the Q-FOG chamber such that one fog collector is placed near the spray nozzle and the second fog collector is placed ±90cm away from the spray nozzle positioned in a manner that it does not collect the sample condensates. The exposure fog rate was maintained at 1.0–2.0ml/hr and the collected condensate pH at 6.4–7.2 per 80cm^2 horizontal collecting area after the chamber has been operating for at least 16 hours or more [45]. The fog condensate volume, pH and the concentrations were recorded on a weekly basis and maintained within this specification (ASTM-B117) [45]. A typical funnel-fog collector arrangement in the Q-FOG chamber is shown in Figure 3-18 and Figure 3-19, highlighting collecting points “A” and “B”.

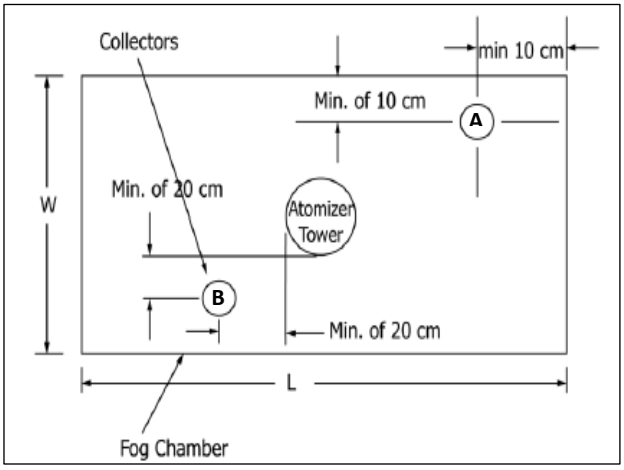

Figure 3-18: Two fog collector set-up in a Q-FOG chamber [40]

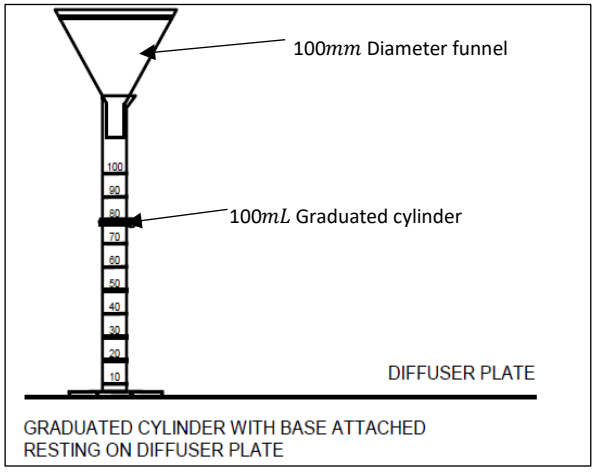

Figure 3-19: Fog collector arrangement [40]

3.5.2.8 Electrolyte solution used to generate corrosive environment

The specimens were exposed to the electrolyte solution of 5wt.%NaCl concentration ($NaCl_{(aq)} \rightarrow Na^+ + Cl^-$) dissociated to the ions of sodium and chloride at intermittent temperatures of 35℃, 40℃, 50℃ and 60℃. The exposure conditions of fog and humid are created inside the chamber depositing sodium chloride moisture on the specimens by means of the chamber cyclic operation. Aqueous sodium chloride solution of 3.5wt.%NaCl concentration is normally used to simulate sea water in the laboratory set up, but when conducting the cyclic corrosion test using the Q-FOG salt spray chamber, 5wt.%NaCl aqueous solution is recommended to exaggerate the exposure conditions inside the chamber (ASTM-B117) [48]. Salt solution of 5wt.%NaCl was prepared by dissolving sodium chloride salt granules ($NaCl_{(s)}$: Mass $= 1.235kg$) in 25L of distilled water complying to ASTM-D1193 [49]. The electrolyte was prepared in batches on a weekly interval

so that the salt granules are completely dissolved prior to transferring to 120L holding tank. The prepared salt solution was left for two days to a week for the salt granules to dissolve to prevent clogging of the spray nozzles [45]. The electrolyte was kept within the specification of 5$\pm$1wt.%NaCl and the pH of 6.4 – 7.2. Tank levels were monitored daily and maintained at high levels to prevent the low tank level alarm from activating. The reagent grade of sodium hydroxide (NaOH) and hydrochloric acid (HCl) were used to adjust the pH when the salt solution was out of specification for acidity or basicity [25].

3.5.3 Exposure by immersion test in copper-copper sulphate–16% sulfuric acid (Cu–$CuSO_4$-16% H_2SO_4): Strauss test

The Strauss test was completed to investigate the intergranular behaviour of the two welded studied stainless steels (AISI304 and SAF2205). The test was carried out in accordance with ASTM A262 practice E, by immersing the specimens in acidified copper sulphate solution using 16% sulphuric acid. Eighteen specimens of AISI304 and SAF2205 weldments were prepared to conduct intergranular attack for the material conditions of as-weld, PWHT 800℃/2h and PWHT 500℃/3h. The Strauss test was conducted by embedding two samples between two layers of copper chips forming a sandwich arrangement (i.e. Cu chips–specimens–Cu chips) before it was immersed in acidified $CuSO_4$ solution. The arranged intergranular attack test set up was brought to boil at a pre-set temperature of 100℃. A set of two specimens from the same material of AISI304 and SAF2205 were boiled in acidified $CuSO_4$ solution at a time.

3.5.3.1 Specimen preparation for acidified copper sulphate solution immersion test

Flat rectangular specimens of 75×25×1mm^3 ([38], were cut such that regions of FZ, HAZ and BM were maintained at the centreline. These specimens were hand ground using SiC abrasive papers with the grit sizes of 500grit, 800grit and 1200grit respectively. The prepared specimens were rinsed with demineralised water to remove dirt followed by degreasing with ethanol solvent before they were submerged into the Cu-$CuSO_4$-16%H_2SO_4 exposure medium.

3.5.3.2 Apparatus set up and preparation of acidified $CuSO_4$ solution used for Strauss test

Apparatus used for the intergranular attack test included the following: four-neck round-bottom flask equipped with four bulbs, Allihn condenser equipped thermometer for temperature reading and an electric hot plate used for heating the solution. The vaporised solution was cooled with the municipal water via Allihn condenser equipped with the water inlet pipe connected to the cooling water source and outlet pipe removing the heat from the vaporised solution. The evaporated solution was condensed back in to the flask maintaining adequate level of the test solution for the

duration of the test. A round-bottom flask was used to contain the experimental arrangement of copper grindings with embedded specimens immersed in 1000mL $CuSO_4$ solution containing 16% H_2SO_4. The test solution was prepared in accordance with the ASTM-A262 practice E, by mixing 100g of reagent grade copper sulphate ($CuSO_4.5H_2O$) with 900mL distilled water and 100mL of 95–99% H_2SO_4. Sufficient amount of copper grindings or shot were used to cover the surface of the specimens by forming a 3−layerd sandwich arrangement in the empty flasks prior to adding the prepared test solution. This was done to ensure effective galvanic coupling between copper chips and the test specimen as it important for intergranular attack testing. The assembled test apparatus was placed on the electric hotplate which was set to maintain the solution boiling temperature of 100℃. The arranged test apparatus was placed in the fume hood extractor for the duration of the test. Thermometer was placed inside the solution via one of the flask necks to monitor the temperature of the solution throughout the testing duration of 15 hours. The timing of the test period began when the solution reached the boiling point and the thermometer was constantly reading 100℃ without fluctuating, See Figure 3-20 below.

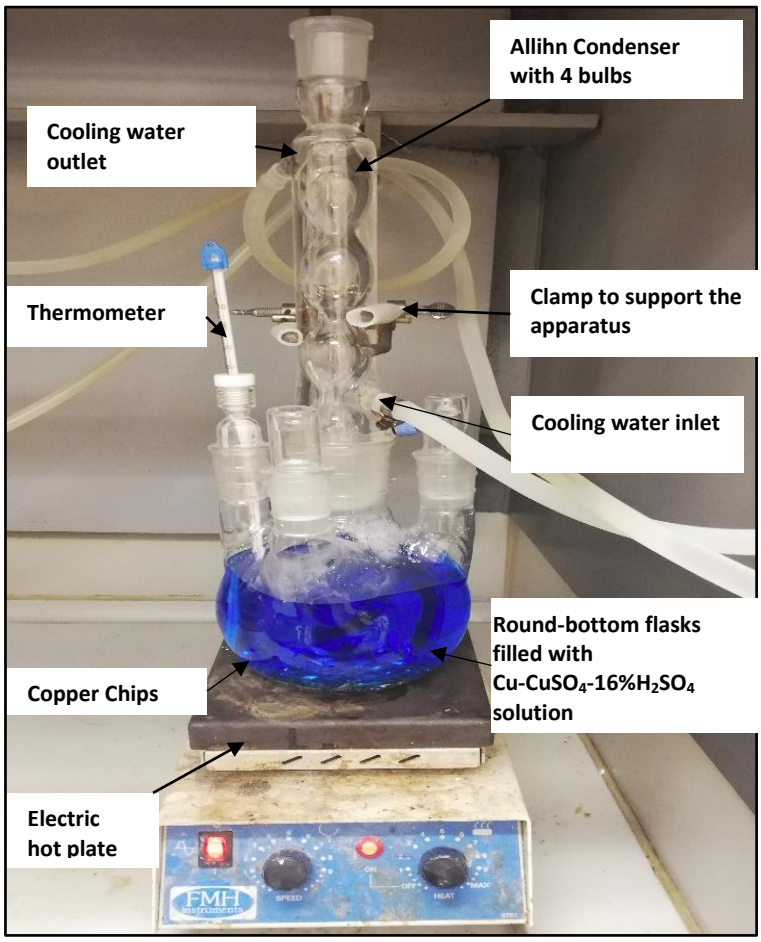

Figure 3-20: Apparatus for Cu–$CuSO_4$-16% H_2SO_4 immersion test

3.5.4 Bend test approach after immersion test

After the immersion test was complete the test solution left for 24 cool down to room temperature. The specimens were removed and etched to identify and mark the centre of specific weld region so that bending moments are imposed at these regions during material qualification. The bend regions were examined using light microscope technique to qualify the materials using qualitative evaluation criteria as per ASTM A262. In particular, the outcome of the ASTM A262 test was decided by determining the degree of bending that is required to initiate cracks at the bend sample area (HAZ, FZ and BM). A degree of localised surface plastic deformation was confirmed after substantial displacement of specimen during bending and without evidence of cracks.

3.5.4.1 Intergranular attack evaluation on AISI304 and SAF2205 using bend test criterion

After the Strauss test was completed, the specimens were cooled to room temperature and rinsed with the distilled water and ethanol. The region of interest was marked by etching the sample to identify the weld zones, FZ, HAZ and BM interface [Figure 3-21 (a) and (b)]. The Zwick tensile testing machine equipped with a 3-point bending rig was used to bend the exposed specimens. The surface on which the weld-FZ and HAZ was marked is indicated by the arrow in [Figure 3-21 (c)]. Bending was completed intermittently by increasing the displacement using a 3-point bending rig.

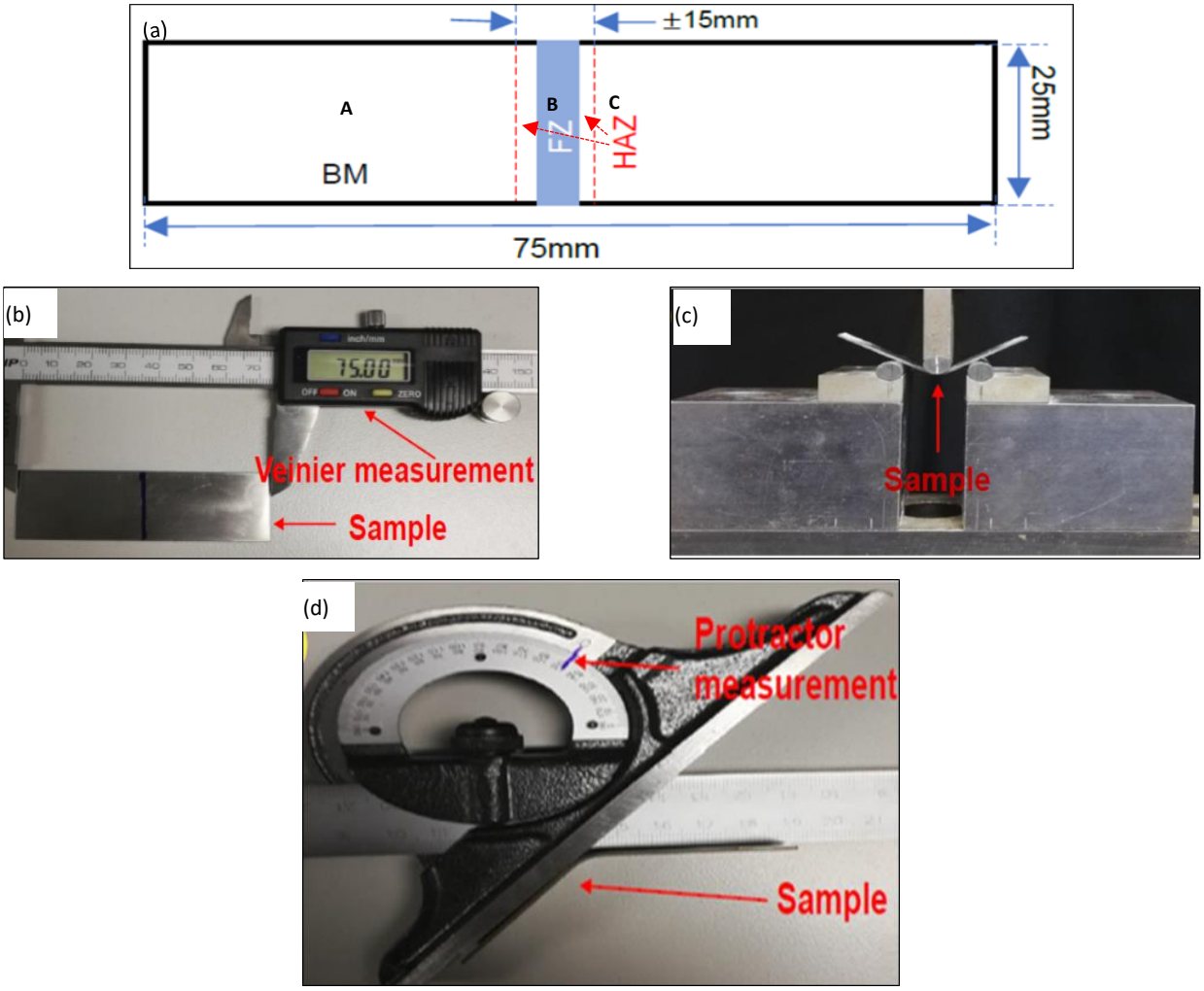

Figure 3-21: (a) Specimen geometry used in Strauss test, (b) The measured 75x25x1$\boldsymbol{mm}^3$ flat specimen, (c) Specimen bended on Zwick bending jigs, (d) Specimen bend angle measurement using the combination square set protractor

The various specimens were aligned in the bend rig to test each of the regions A, B and C as indicated in [Figure 3-21 (a)]. The specimen marked regions were bent intermittently by displacements of 1mm increments until the displacement measurement of 5-10mm was read on computer monitor [Figure 3-21 (c)]. In between the bending intervals, the load was released freeing specimens from the load and the surface effect was examined for intergranular attack using the light microscope. Defects or indications such as fissures, wrinkles, deformation lines and cracks were analysed at the apex of the bent surface. The surface analyses were completed accompanied by measuring the specimen bend angle using the combination square set protractor to determine the angle at which the defects were detected [Figure 3-21 (d)]. This was repeated for every bend at 1mm displacement for 5 to 10 times until the bend angle of 27° for FZ, 40° for HAZ and 60° for BM was measured. The termination angles were determined by bending of specimens at a specific region (FZ, HAZ and BM) and when the indications of cracks start to become evident, the bend angle was then measured and used as a reference to measure the rest of the samples.

3.6 Microstructural Characterization

Microstructural properties of an engineering alloy are largely influenced by thermal treatment, chemical composition and various production processes. The evaluation of materials metallurgical microstructure plays a significant role in distinguishing properties of one alloy as opposed to the other. The material's microstructure has a direct influence on its performance towards susceptibility to corrosion and mechanical properties. In view of this rationale, evaluation of AISI304 and SAF2205 to characterise the morphology, topography, fractography, microstructure and compound information was completed. The use of light illumination microscopy was done to analyse the microstructures for the distinct weldment regions (HAZ, FZ and BM) and their evolution during PWHT at a meaningful magnification. The analysis using the light microscope technique was adopted to examine the exposed surface quality post SCC exposure tests and intergranular attack tests. Likewise, electron illumination microscopy using the detectors for backscatter electrons (SEM-BSE) and energy dispersive X-ray spectroscopy (SEM-EDS/EDX) were deployed to identify and analyse the metallic alloy compositions in microstructure.

3.6.1 Light microscopy analysis

The micrographs for the representative microstructures of the weld regions were acquired using a NIKON Eclipse MA200 Inverted microscope equipped with camera for the material photomicrographs. The examined micrographs revealed features such as grains, grain boundaries, phase contrast, twinning and inclusions. The Leica MZ8 low power light microscope was used to analyse the surface topography for general surface features such as cracks, fissures, deformation lines, wrinkles and other defects during intergranular attack analysis. The SCC defects such as pits, corrosion products and cracks were also analysed using the Leica MZ8 microscope.

3.6.1.1 Specimen preparation for light microscopy analysis

The specimens of AISI304 and SAF2205 were sectioned to represent the following regions of interest; FZ, HAZ and BM to characterise microstructural evolution due to welding and the effect of PWHT. The microscopy characterisation for these welded regions was completed in the specified conditions of as-received, as-weld and PWHT at 500℃/3h and PWHT at 800℃/2h. The specimens were sectioned so that the welded regions of interest are represented before mounting with resin using a hot-press. This action was followed by progressive surface grinding with SiC wet grinding paper (250-grit, 500-grit, 800-grit and 1200-grit). Specimens were mechanically polished for a final mirror like surface finish. The prepared specimens were etched by means of selective chemical etching using two different etching techniques for each of the studied materials to reveal the

microstructure for microscopy analysis. The AISI304 specimens were etched by applying an etchant containing 3-parts glycol ($C_2H_6O_2$), 2-parts hydrochloric acid (HCl) and 1-parts Nitric acid (HNO_3) to cover the polished area. The etchant was applied using a syringe to the AISI304 specimen which was left for 30 seconds before it was rinsed off with distilled water and ethanol, followed by air-drying using blow dryer.

The SAF2205 specimens were etched using an electro-etching technique to reveal the distinct dual structures of ferrite-δ and austenite-γ in the BM and the distinct features of the welds regions (BM, FZ and HAZ) through contrast enhancement/staining (Figure 4-6). The electro-etching technique was executed in accordance with the ASTM A923 standard, test method A. The apparatus used to complete the electrical circuit to successfully electro etch SAF2205 specimens using sodium hydroxide (NaOH) electrolyte are listed below as follows:

i. Source of Direct Current (DC) – Top-ward dual tracking DC power supply 6303D powered at the voltage of 2V at the current flow of 9A – 15A, applied for 30 seconds.

ii. Cathode – Cylindrical piece of platinum (Pt) metal.

iii. Electric clamp to hold specimen – Conductive metal tong with non-conductive holders.

iv. Electrolyte – NaOH reagent grade at 10N concentration which was prepared by mixing 40g of NaOH and 50ml of distilled water.

The electrical circuit was completed using the apparatus listed above, ensuring that the current flow from the anode (sample) to the cathode (Pt metal) via 10N [NaOH] electrolyte for a period of $\pm$30s, thus etching the specimen (anode) by means of selective corrosion. The etched specimens were instantly rinsed with demineralised water and then ethanol followed by air drying using a blow dryer before they were ready for the microstructural examination using light microscope and electron microscope.

3.6.2 Scanning Electron Microscope (SEM)

The scanning electron microscope (NovaNano SEM) was employed to generate surface images of the specimens at microscopic level employed at magnification greater than those achievable using light microscopy to analyse features such as microstructure, morphology and elemental composition.

3.6.2.1 Specimens preparation for scanning electron microscopy (SEM)

The specimens were cautiously removed from the mounting resin (unmounted) and cleaned with distilled water and acetone solvent to remove minute debris/dust or any extraneous materials, followed by drying before they were attached to the aluminium SEM specimen stubs. The prepared specimens were attached to the SEM specimen stubs with agar silver paint and or conductive carbon adhesive tape. The assembled specimens were sputter coated with a layer of conductive

carbon at 5-50nm, to provide a conduction path for the non-conductive phases that might be present within the microstructures, so that they can be imaged using scanning electron microscope technique.

3.6.3 Energy Dispersive X-ray Spectroscopy (EDX/ EDS) analysis

The type NovaNano SEM 230 microscope was employed to acquire information on the exposed specimen's elemental composition through the launch of energy dispersive X-ray spectroscopy detectors (SEM-EDS/EDX) collecting the emitted signals from the specimen's atoms and detecting the characteristics X-ray from the specimen to producing imaging at high resolution. The technique was used to identify the secondary phases formed as a result of welding and heat treatment within specimens' welded regions and to quantify the elemental compositions by pre-selecting the field of view or spot selection at the areas of interest. Compositional analysis is dependent on the electron interaction volume with the analysed specimen to emit X-ray excitation photon which has a wavelength that is characteristic for the element. The EDS characterisation effectiveness is mainly because of the fundamental principle that elements having a different atomic structure emitting a unique set of peaks on its electromagnetic emission spectrum, which is the principle of spectroscopy. For the excitation of characteristic X-rays from field of view, high energy beam at 20keV, charged with primary electrons was focused into the specimens pre-selected zone or point. The penetration depth of the X-ray beams is at few microns suggesting that chemical data obtained could possibly contain information beneath the surface layers.

CHAPTER 4 RESULTS AND DISCUSSION

4.1 Long term salt spray exposure tests

The inspections revealed the corrosion progression for SAF2205 and AISI304 specimens exposed under similar conditions and durations in the Q-FOG cyclic corrosion tester. The SCC tests using the Q-FOG salt chamber were only terminated when severe corrosion was observed on the apex of the bent specimens. Selective weekly visual inspections to quantify the effects of the cyclic corrosion exposure test on the exposed AISI304 and SAF2205 specimens was performed. The exposed specimen surface features were analysed to determine the corrosion extent and type. Specimens images were taken during inspections which are chronologically presented in Table 11: As-weld, Table 12: PWHT at 500℃/3h, Table 13: PWHT at 800℃/2h and Table 14: As-received BM. The tabulated results compare corrosion progression for the tested materials before exposure followed by selective weekly inspections. The affected surface was qualitatively analysed by comparing tested material surface texture and corrosion surface damage.

4.1.1 Salt chamber exposed materials in the as-weld condition

Table 11 demonstrates the inspected surface condition of exposed materials in the as-weld condition. It can be observed that AISI304 specimens started showing corrosion indications during week 11 with increasing deterioration during each inspection with extended exposure durations. During week 13 pitting corrosion had already initiated at the apex (weld filler metal) of the AISI304 bend specimens. With further exposures during week 27 to the final week of inspections corrosion pits had exacerbated revealing flaws of dark brown corrosion product patches, corrosion pits and passive film breakage [Figure 4-1 (c)].

SAF2205 specimens on the other hand illustrated corrosion resistance properties as there were no corrosion defects such as pits, cracks and corrosion products like the ones inspected in AISI304 specimens. The welded specimens of SAF2205 showed resistance to corrosion even after extended salt chamber exposure durations as illustrated in Table 11 and Figure 4-1.

4.1.2 Exposed materials in the PWHT at 500℃/3h condition

Table 12 illustrates the tabulated results for AISI304 and SAF2205 specimens that were PWHT at 500℃/3h prior to exposure in the salt chamber for the cyclic corrosion test. Observations showed that under this condition AISI304 specimens behaved like the specimens in the as-weld conditions. Corrosion flaws in the form of numerous micro-fissures and minute pits accompanied by red and

brown corrosion product were visible during week 6. With the extended exposures, during week 45 the flaws had progressed forming more pits and dark brown corrosion products which created a crust covering the metal substrate as demonstrated in [Figure 4-2 (c) and (e)]. Occlusion of corrosion products had propagated to the extent that it prevented observation of the pits on the metal surface. A cracked dark brown corrosion layer was cleaned using neutral activator and rinsed with distilled water and blow dried in order to analyse the crack origin. Light microscopy analysis confirmed that the crack was not from the metal substrate but instead it was breakage of the passive layer, see [Figure 4-2 (e)].

SAF2205 specimens revealed insignificant corrosion product at the apex during inspections. From the initial inspection during week 6 to the final inspections during week 45, it can be observed that the NaCl containing solution had selectively precipitated and accumulated the salt at the stress point and or flawed region leading to the insignificant red/brown corrosion products -Table 12.

4.1.3 Exposed materials in the PWHT at 800℃/2h condition

Inspections conducted on AISI304 specimens, which were PWHT at 800℃/2h and exposed to the cyclic corrosion test, revealed their susceptibility to the salt chamber exposure conditions. During week 6 corrosion was observed to have initiated at the apex and edges of AISI304 specimens. These are the stress regions whereby they become anodic leading to localised corrosion, and hence there was evidence of red/brown corrosion products at these regions. The corroded regions had propagated with exposure durations forming corrosion pits growing to week 43 of inspections -Table 13. During the final inspections in week 43 corrosion products had developed to a dark brown colour with cracks. In order to inspect the specimen surfaces, the oxide film was cleaned using neutral activator as described in the preceding section (§ 4.1.2). The cleaned AISI304 specimens were analysed further, whereby the broken oxide was removed or cleaned and not mistaken for cracked metal substrate. A significant number of pits was also witnessed [Figure 4-3 (c) and (e)].

On the other hand, the exposed SAF2205 specimens in the conditions of PWHT800℃/2h were analysed to be insufficiently affected by the cyclic corrosion test exposures in comparison to the AISI304 specimens exposed to comparable heat treatment conditions, see Table 13. SAF2205 specimens had crystallised NaCl selectively on the specimens which could be easily wiped or rinsed off with water [Figure 4-1 (b), (d) and (f)].

4.1.4 Exposed materials in the as-received conditions

Table 14 sequentially tabulates the cyclic corrosion exposure test results for AISI304 and SAF2205 during selective weekly inspections. Observations on the exposed AISI304 revealed corrosion initiating between week 3 and 8 of exposure, with the evidence of minor red corrosion products at

the specimen's apex and edges where there is high stress concentration. The inspected region becomes more saturated with corrosion product with the extended exposure durations that initiated minute pits selectively covering the specimen.

SAF2205 specimens had no indications of corrosion flaws until final inspections during week 43, as can be seen in [Figure 4-4 (b), (d), and (f)]. The white NaCl crystals observed on SAF2205 specimens can be easily removed by swabbing with a cloth or rinsing with water leaving the specimen surfaces like before exposure tests.

4.1.5 Summary of exposure tests for SAF2205 and AISI304

In summary the imaging results can be concluded that in the first week of exposure, both materials had no defects or indications of corrosion products or rust. However, with the extended exposure durations the deposition of red/brown corrosion products started to initiate at the apex of AISI304 specimens in the heat treated and untreated specimen conditions, whereas the SAF2205 specimens were not affected by similar conditions. Cyclic corrosion exposure test results were interpreted using light microscope surface imaging at acceptable magnification as presented in Figure 4-1, Figure 4-2, Figure 4-3 and
Figure 4-4.

SAF2205 specimens demonstrated trends of not being susceptible to salt chamber cyclic corrosion exposures in two specimen conditions namely; as-weld and as-received. Whereas the SAF2205 specimens that were PWHT at 800℃/2h and 500℃/3h demonstrated insignificant degree of proneness to corrosion after minor corrosion products were observed. The PWHT at 800℃/2h SAF2205 specimens had no traces of iron oxide (Fe_2O_3)/ rust for more than 15 weeks of cyclic corrosion exposure test. Instead there were deposits of white NaCl crystals from the crystallised fog and humidity of NaCl moisture created within the salt chamber [Figure 4-1, Figure 4-2, Figure 4-3 and
Figure 4-4, see (b), (d) & (f)].

The noticeable trend for the exposed AISI304 specimens was the early appearance of defect such as corrosion products which formed a cracked crust of rust and pitting during the extended exposure durations. Contrarily, the corrosion products on SAF2205 specimens was not as prompt compared to AISI304 specimens.

The onset of corrosion products was visible in week 11 to week 13 of the as-weld AISI304 specimens, but only became visible in week 6 for the specimens that were PWHT. On the other hand, the as-weld SAF2205 specimens had no corrosion products on them. The onset of corrosion was only visible on SAF2205 specimens PWHT at 800℃/2h and 500℃/3h during week 20 and week 45 respectively.

Table 11: Cyclic corrosion exposure results for AISI304 and SAF2205 specimen in the as-weld condition

Welded specimens (represented by white dashed lines) in the as-weld condition		
Duration	**AISI304**	**SAF2205**
Before exposure		
Week 11		
Week 12 06 July		
Week 13 19 July		
Week 15 09 August		
Week 21 13 September		
Week 23 27 September		
Week 27 18 October		
Week 35 13 December		
Week 39 13 January		
Week 43 13 February		

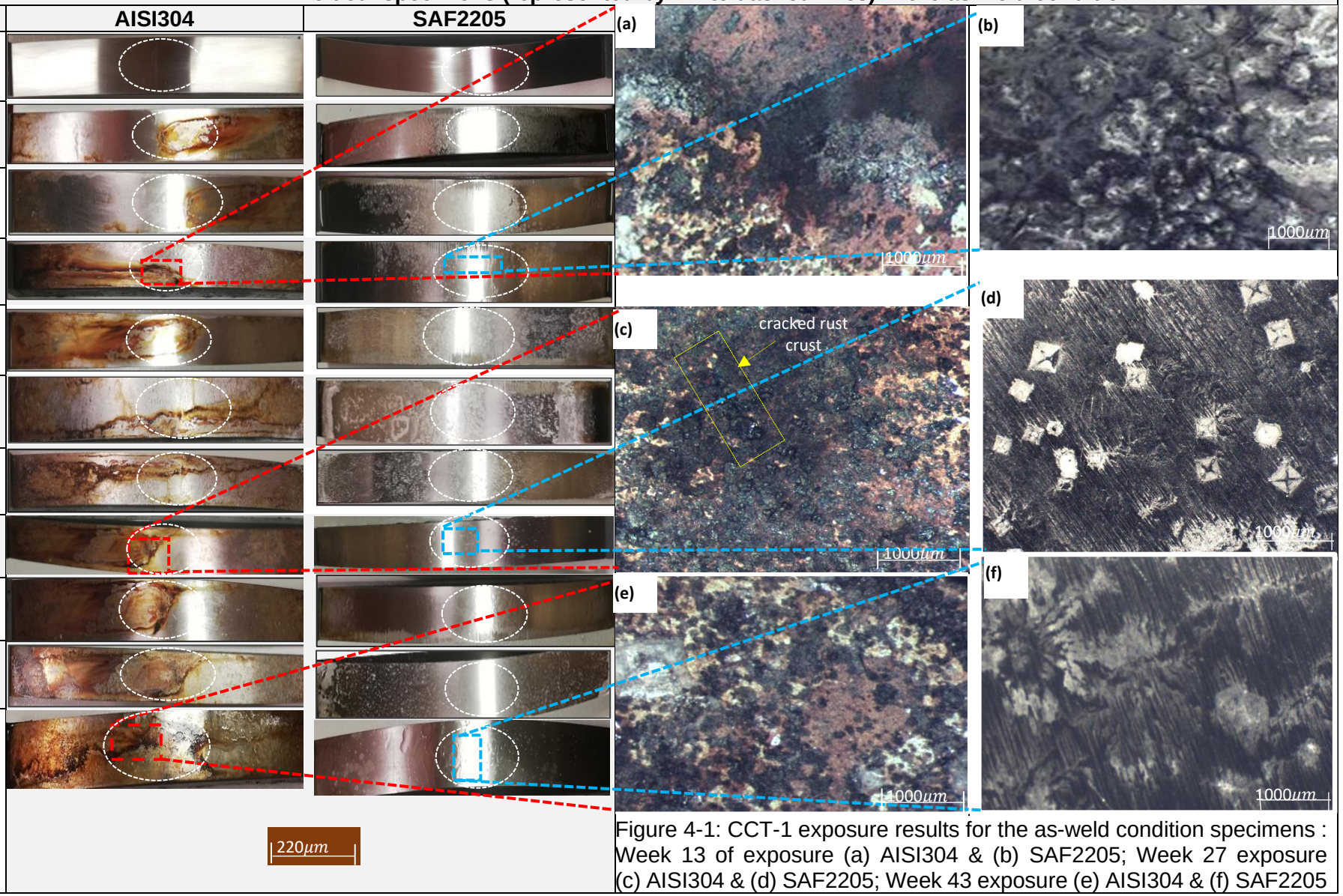

Figure 4-1: CCT-1 exposure results for the as-weld condition specimens : Week 13 of exposure (a) AISI304 & (b) SAF2205; Week 27 exposure (c) AISI304 & (d) SAF2205; Week 43 exposure (e) AISI304 & (f) SAF2205

Table 12: Cyclic corrosion exposure results for AISI304 and SAF2205 specimen in the PWHT condition of 500°C for 3 hours

Welded specimens (represented by white dashed lines) and then heat treated at 500℃ for 3h		
Duration	**AISI304**	**SAF2205**
Before exposure		
Week 6 12 July		
Week 8 26 July		
Week 10 09 August		
Week 15 13 September		
Week 17 27 September		
Week 18 04 October		
Week 20 18 October		
Week 35 13 December		
Week 39 13 January		
Week 45 13 February		

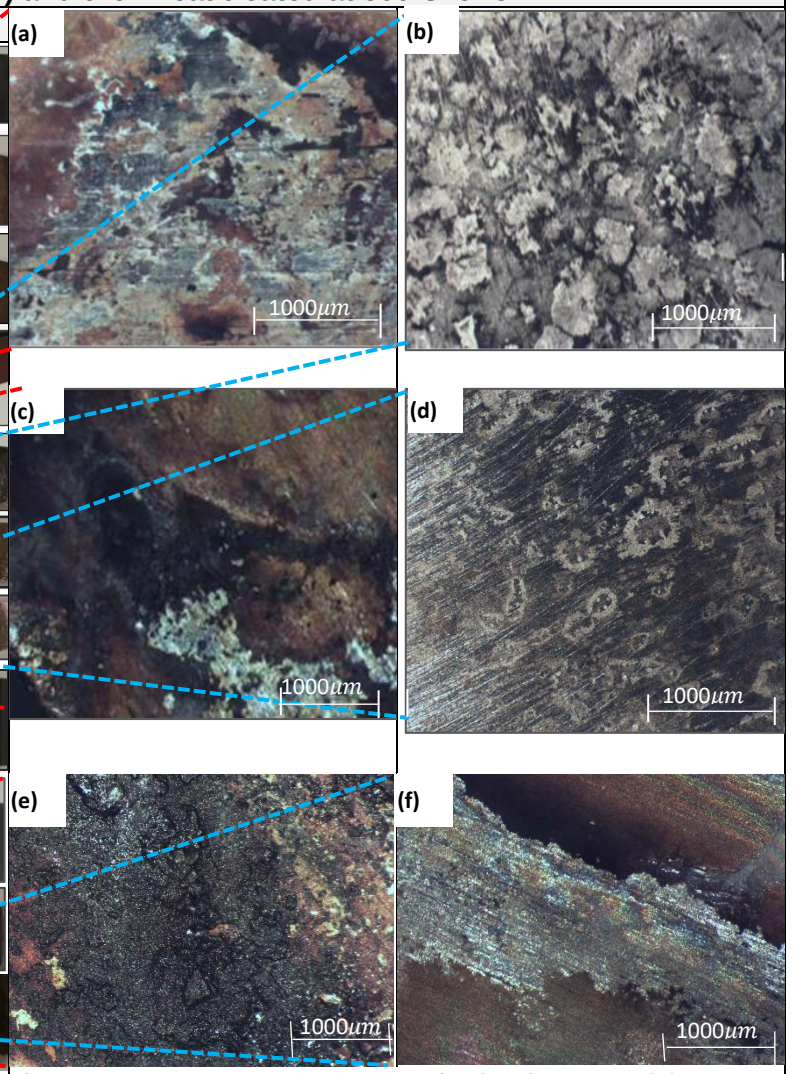

Figure 4-2: CCT-1 exposure results for the 500℃/3h PWHT specimens; 15 weeks of exposure (a) AISI304 & (b) SAF2205 (c); AISI304 at week 17 (d) SAF2205 at week 18; 45 weeks of exposure (e) AISI304 and (f) SAF2205

Table 13: Cyclic corrosion exposure results for AISI304 and SAF2205 specimen in the PWHT condition of 800°C for 2 hours

Welded specimens (represented by white dashed lines) and then Heat treatment at 800℃ for 2h		
Duration	**AISI304**	**SAF2205**
Before exposure		
Week 4.5	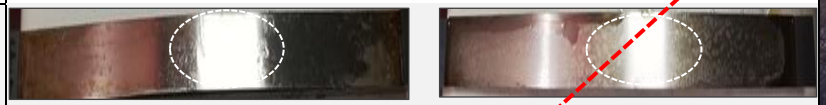	
Week 6 12 July		
Week 8 26 July		
Week 10 09 August		
Week 15 13 September		
Week 17 27 September	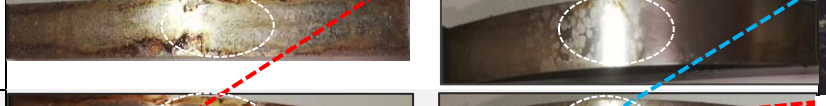	
Week 20 18 October		
Week 35 13 December		
Week 39 13 January	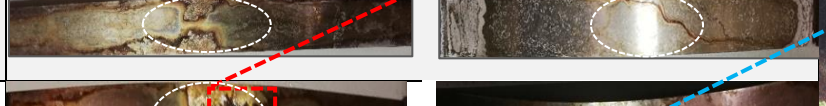	
Week 43 13 February		

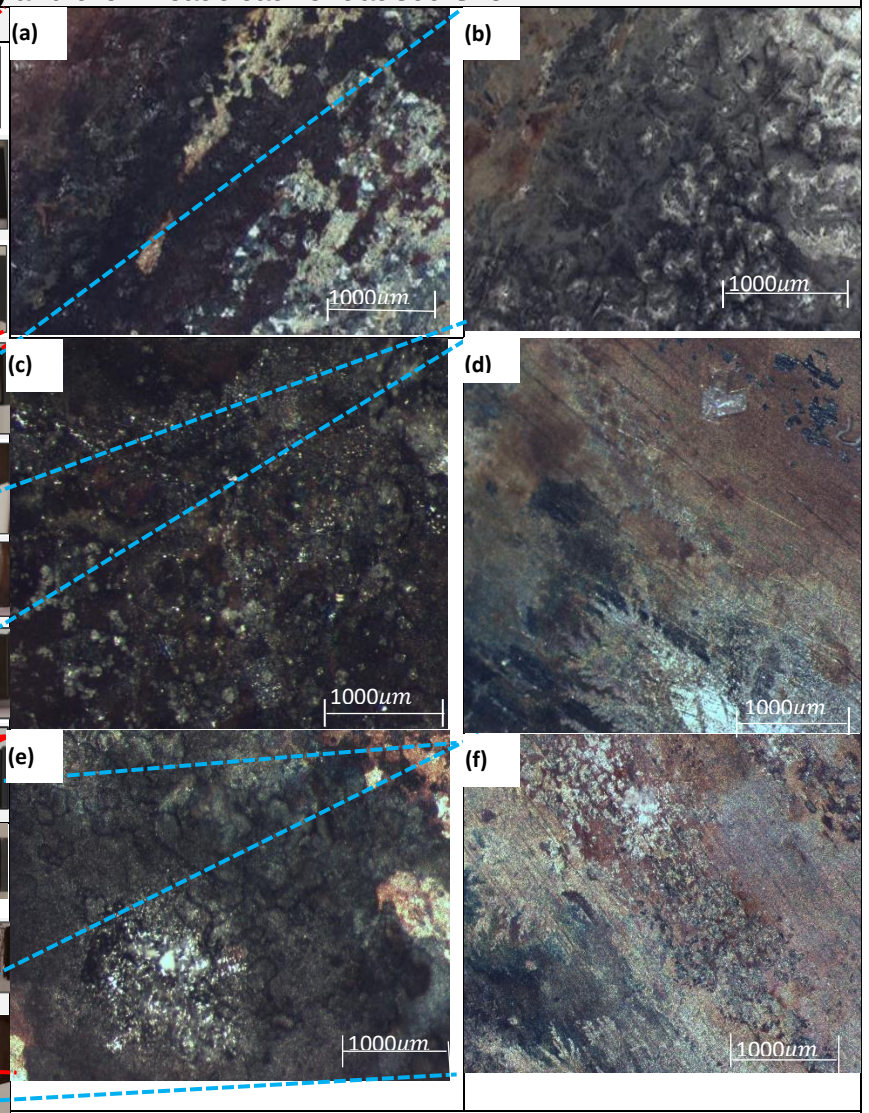

Figure 4-3: CCT-1 exposure results for the 800℃/2h PWHT specimen after 15 weeks (a) AISI304 & (b) SAF2205; After 20 weeks of exposure (c) AISI304 & (d) SAF2205; After 43 weeks of exposure (e) AISI304 and (f) SAF2205

Table 14: Cyclic corrosion exposure results for AISI304 and SAF2205 specimen in the as-received condition

As-received condition (Not welded)		
Duration	**AISI304**	**SAF2205**
Before exposure		
Week 3 6 July		
Week 8 26 July		
Week 10 09 August		
Week 15 13 September		
Week 17 27 September		
Week 28 18 October		
Week 35 13 December		
Week 39 13 January		
Week 43 13 February		

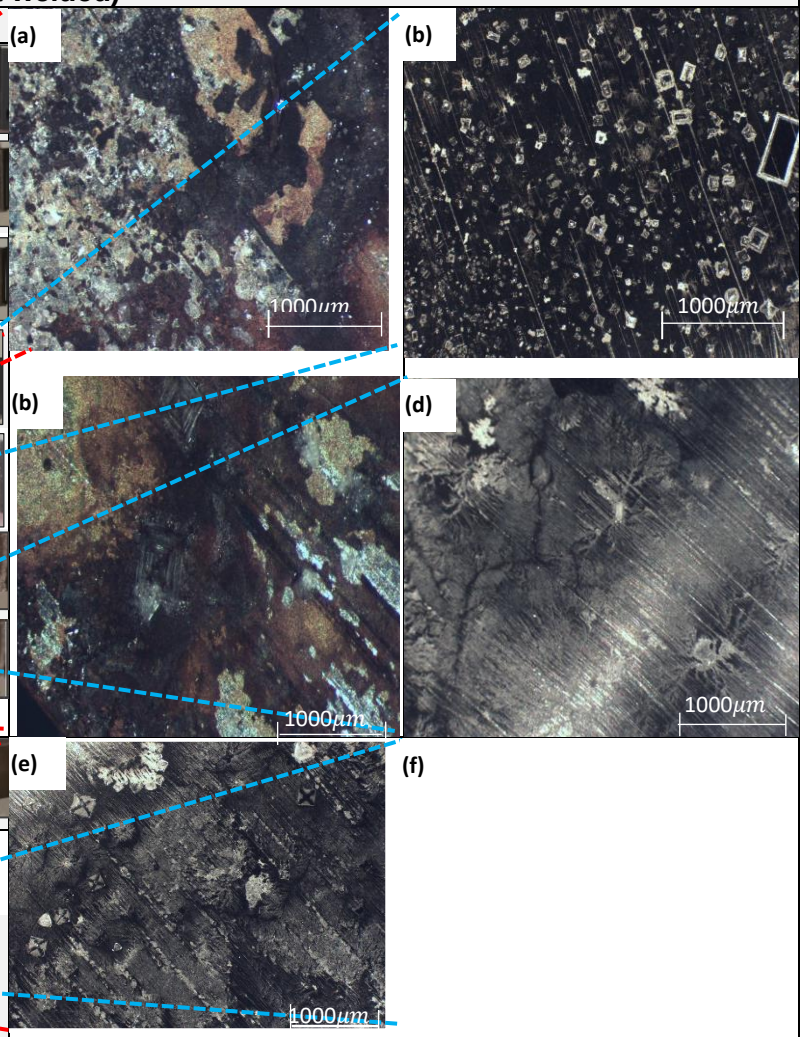

Figure 4-4: CCT-1 exposure results for as-received specimen after 15 weeks (a) AISI304 & (b) SAF2205; After 28 weeks (c) AISI304 & (d) SAF2205; After 43 weeks (e) AISI304 & (f) SAF2205

4.2 Exposure in boiling Cu-$CuSO_4$-16% H_2SO_4 solution

Following the different specimen treatment by immersion test in boiling Cu-$CuSO_4$-16%H_2SO_4 solution, the bend test was performed to qualify the susceptibility to intergranular attack. The bend specimens were examined with light microscopy at the apex of the bent region at low magnification. The bright field light illumination microscope of type Leica DFC 280 stereo and Nikon optiphot was used to complete the topographic examination of the outer radius of the bend specimens in accordance to ASTM A262. The surface features after the bend test were evaluated using the following criteria; smooth surface [Figure 4-5 (a)] implies the absence of intergranular attack, whereas presence of the indications such as those of fissures or cracks denoted presence of intergranular attack [Figure 4-5 (b)]. When evaluation results are ambiguous with the analysis revealing surface ductility properties i.e. wrinkles, deformation lines, dimples etc., then these defects are disregarded as they do not indicate intergranular attack failure mode [Figure 4-5 (c)].

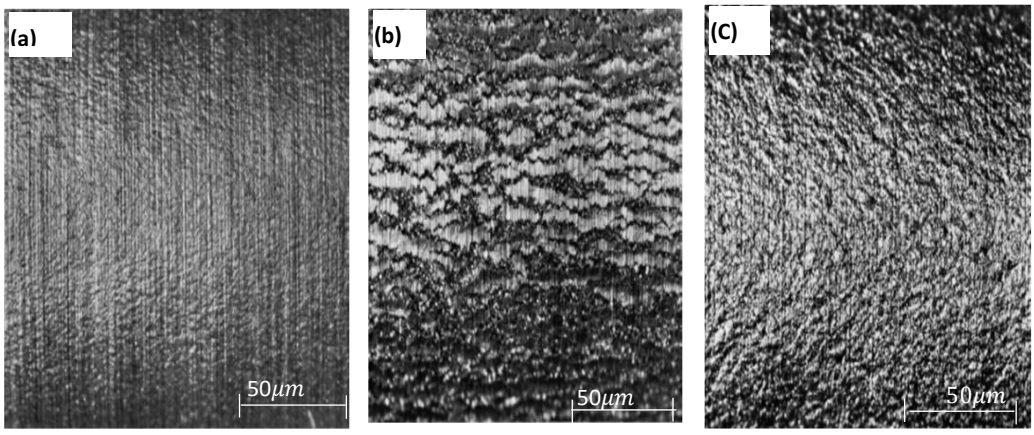

Figure 4-5: (a) Passing test specimen, (b) Failing test specimen, (c) Unclear but passing results

The appearance of deformation lines on the bend specimen surface i.e. wrinkles and or “orange peel” without accompanying fissures or cracks, was considered to be free from intergranular attack [50].

4.2.1 Intergranular attack test results and discussion

After exposure in the boiling Cu-$CuSO_4$-16%H_2SO_4 solution, the region of interest, namely FZ, BM and HAZ, were marked in order to ensure that maximum deformation occurred at these regions during the post-exposure bending test marked as points “B”, “A” and “C” respectively shown in Figure 3-21 (a).The weld regions were bend and extended at 1mm displacement intervals or until failure occurs by cracking. These are comparative tests and hence the exposed specimens were bent at increasing angles until cracking was identified on either AISI304 or SAF2205 specimens at a region of interest viz. FZ, HAZ and BM shown in Table 15, Table 16 and Table 17 respectively.

4.2.1.1 Fusion zone (FZ) analysis

The acidified Cu-$CuSO_4$ treated FZ specimens of AISI304 and SAF2205 were gradually bent at 1mm displacement intervals at which the bend angle was measured in between the bending intervals. The FZ of less ductile material (SAF2205 - PWHT at 800℃/2h) cracked when the specimens were bent at 27° after 10mm displacement. Thus, the measured bent angle of 27° was was used as the reference to bend all the FZ marked specimens. Two of AISI304 and SAF2205 specimens that were initially exposed in the boiled acidified Cu-$CuSO_4$ solution were precisely marked at the FZ, followed by bending of the marked region as explained above. The apex of the 27° bend FZ specimens were examined using light microscopy thereafter. The analysed FZ for both tested materials in the conditions of as-weld and PWHT at 500℃/3h revealed wrinkles and deformation lines without significant defects or indications of fissures and or cracks. The observed surface features of wrinkles and deformation lines are normally disregarded, following evaluation criteria stipulated in ASTM A262 as discussed in the previous section. Thus, the analysed weld region (FZ) for both tested materials under specified conditions were found to be free from intergranular attack. PWHT at 800℃/2h AISI304 FZ-specimens bent at 27° followed comparable trends. Conversely, SAF2205 FZ-specimens PWHT at 800℃/2h exposed to similar test conditions displayed crack defects of less ductile nature which could be seen with the naked eye. Thus the SAF2205 material in the PWHT at 800℃/2h condition was confirmed to be susceptible to intergranular attack under the specified Cu-$CuSO_4$ conditions [Table 15-(f)].

Table 15: Intergranular attack bent test results conducted on FZ bent at 27°

FZ at 27°bend angle				
Condition	**AISI304**	**AISI304 Comments**	**SAF2205**	**SAF2205 Comments**
As-weld	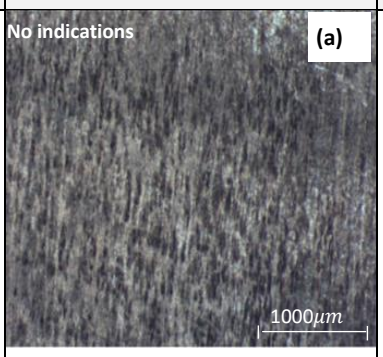	Presence of minute deformation lines. No intergranular attack	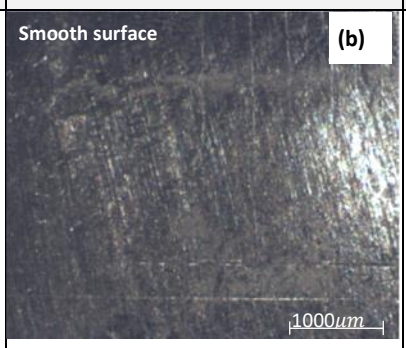	Presence of wrinkles and deformation lines. No intergranular attack.
500℃ PWHT at 3hours	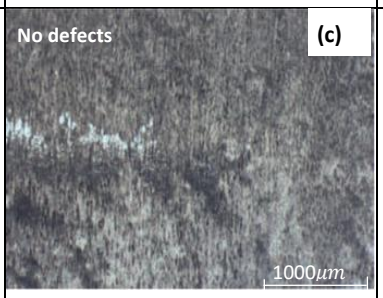	Presence of deformation lines. No intergranular attack.	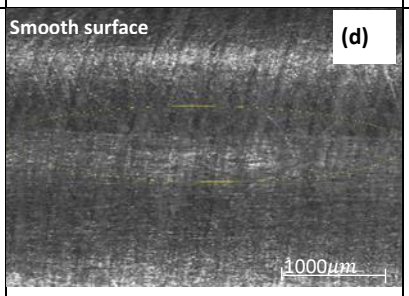	Presence of wrinkles and deformation lines. No Intergranular attack.
800℃ PWHT at 2hours	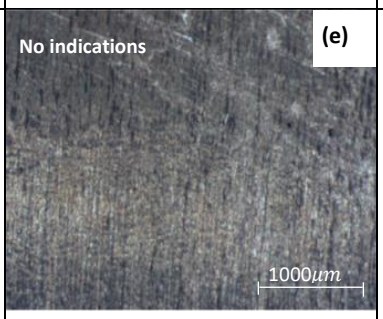	Presence of deformation lines. No intergranular attack.	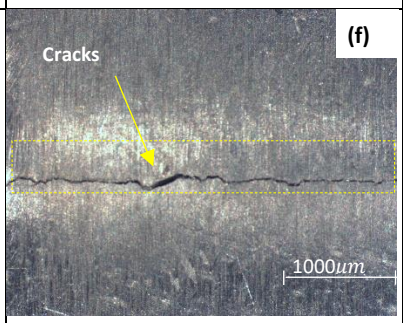	Appearance of a crack. Presence of intergranular attack.

4.2.1.2 Heat affected zone (HAZ) analysis

The bend test was completed on the marked region ”C” representing specimens HAZ as demonstrated in [Figure 3-21 (a)]. The bending angle at the HAZ was performed using a similar procedure for bending the FZ as cited in § 4.2.1.1. The measured bend angle of HAZ at which the less ductile specimen (SAF2205 PWHT at 800℃/2h) crack failed was at 40°. HAZ specimens of AISI304 and SAF2205 were bent at 1mm displacement intervals until 40° bend was measured. The apex of the bend specimens was analysed for surface defects between the bending intervals. The 40° bend results for the HAZ specimens in the conditions of as-weld, PWHT at 800℃/2h and 500℃/3h are tabulated in Table 16 below. AISI304 HAZ specimens followed comparable trends with the FZ specimens displaying indications that are disregarded for intergranular attack (i.e. surface-

dimples, uneven surface, fissures etc.). Thus 40° bending of HAZ for AISI304 and SAF2205 specimens in the conditions of as-weld and PWHT at 500℃/3h, confirmed the absence of intergranular attack. Conversely, SAF2205 HAZ specimens at the PWHT at 800℃/2h condition that was initially exposed to Cu-$CuSO_4$ solution and then 40° bent showed visible cracks as demonstrated in [Table 16 (f)], whereas the AISI304 specimens that was exposed to similar conditions demonstrated minute fissures that are typically disregarded for intergranular attack evaluation as shown in [Table 16 (e)].

Table 16: Intergranular attack bent test results conducted at the HAZ bent at 40°

HAZ at 40°Bend angle				
Condition	**AISI304**	**AISI304 Comments**	**SAF2205**	**SAF2205 Comments**
As-weld	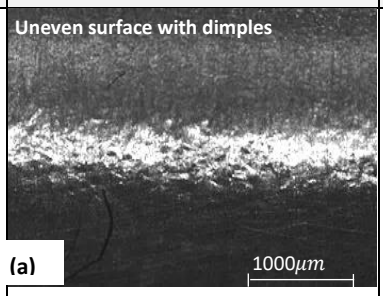	Minute fissures and deformation lines. No intergranular attack	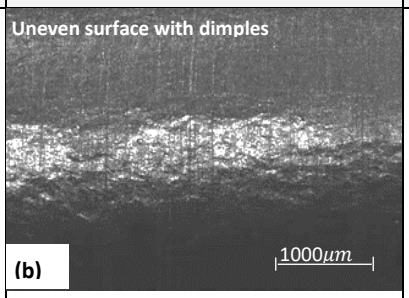	Minute dimples and deformation lines. No intergranular attack.
500℃ PWHT at 3hours	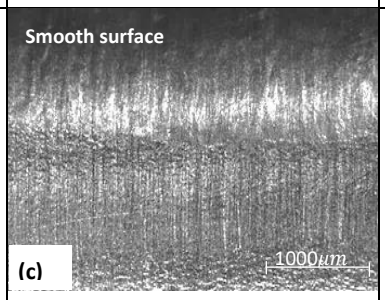	Minute Deformation lines. No intergranular attack.	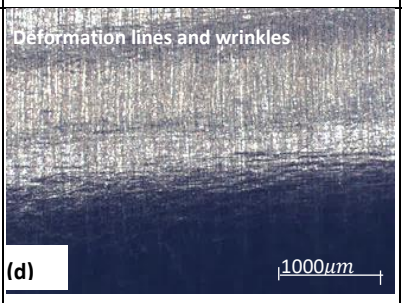	Minute deformation lines & wrinkles. No Intergranular attack.
800℃ PWHT at 2hours	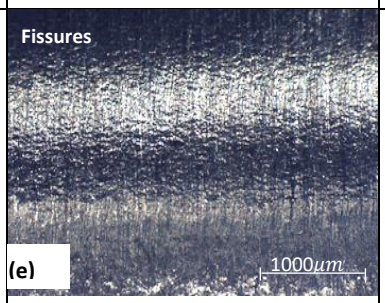	Fissures & orange peels. No intergranular attack.	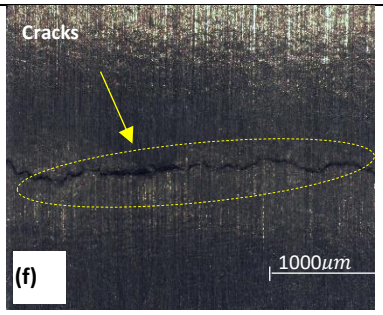	Presence of Cracks. Presence of intergranular attack.

4.2.1.3 Base metal (BM) analysis

The marked BM specimens were bent at 1mm displacement intervals and analysed using light microscopy with the bend angle measured in-between intervals. Intergranular qualification bend test results presented in Table 17 were achieved by 60° bending of BM marked as “A” in Figure 3-21 for tested SAF2205 and AISIS304 specimens in the conditions of as-weld-BM, PWHT at 800℃/2h and 500℃/3h. The inspected apex for the BM bent surface revealed surface features such as deformation

lines, wrinkles, dimples and minute fissures which are generally disregarded for intergranular attack evaluation since these are features caused by plastic deformation of the near surface microstructure. The analysis can be concluded that the BM for both tested materials under treatment conditions of as-weld BM, PWHT at 800℃/2h and 500℃/3h are not prone to intergranular attack even when bent to higher angles of 60°, see Table 17 below.

Table 17: Intergranular attack bent test results conducted at the BM bent at 60°

BM at 60°Bend angle				
Condition	**AISI304**	**AISI304 Comments**	**SAF2205**	**SAF2205 Comments**
As-weld	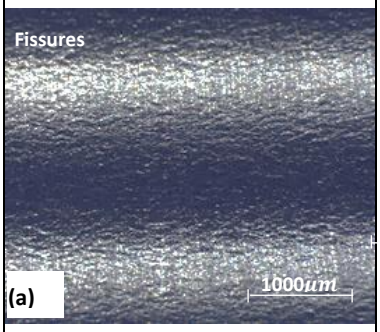	Minute fissures and or orange peels. No intergranular attack	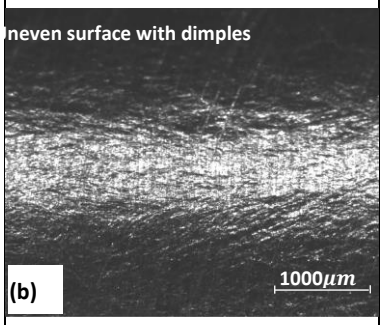	Deformation lines and wrinkles. No intergranular attack
500℃ PWHT at 3hours	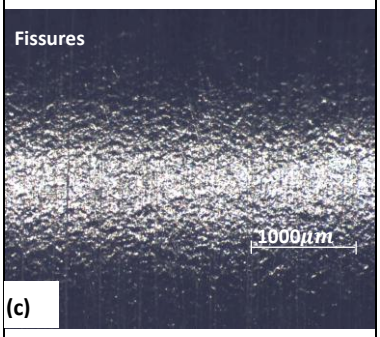	Minute fissures and or orange peels. No intergranular attack	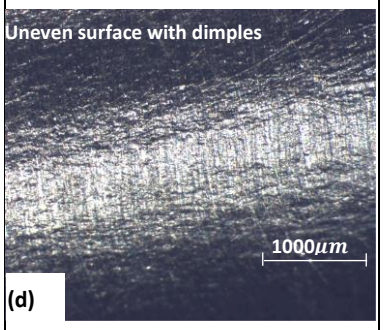	Deformation lines and wrinkles. No intergranular attack
800℃ PWHT at 2hours	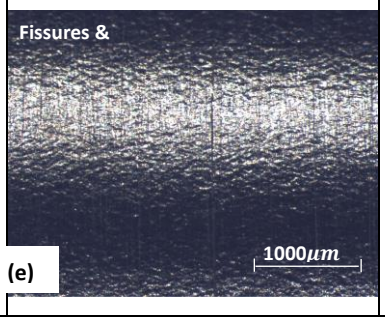	Minute fissures or orange peels. No intergranular attack	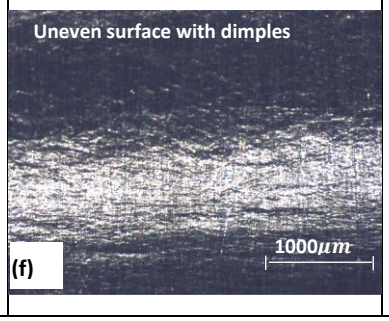	Deformation lines and wrinkles. No intergranular attack

Intragranular attack results presented in Table 15, Table 16 and Table 17 can be summarised to highlight that the welded material of SAF2205 PWHT at 800℃/2h was found to be less ductile in comparison to AISI304 PWHT at 800℃/2h due to the brittle crack formation. The material also demonstrated to be prone to intergranular attack at the weld regions of FZ and HAZ because of its crack failure mode during the bend testing.

Parent metals for both tested materials demonstrated their ductile properties at the conditions of as-weld, PWHT at 8000℃/2h and 500℃/3h. The SAF2205 parent metal in all of exposure conditions demonstrated some level of ductility through uneven surface with minute dimples and deformation lines that were observed (Table 17). This type of surface topography is usually disregarded as failure criteria for evaluating intergranular attack for metals. Thus, the parent metal for both studied materials were inspected not to be susceptible to intergranular attack under the specified conditions. The specimens of AISI304 in the conditions of as-weld, PWHT at 800℃/2h and 500℃/3h revealed surface topography associated with surface plastic deformation, and consequently they were disregarded for proneness to intergranular attack, and it can be concluded that this material at the specified conditions does not suffer intergranular attack.

4.3 Microstructural Characterization results

Optical light microscopy was applied to reveal the microstructures of etched AISI304 and SAF2205 welded specimens in the as-weld condition and in the PWHT at 800℃/2h. The two specimens' conditions were analysed using light microscopy techniques to characterise any transformed intermetallic phases that might have precipitated at the areas of interest. The studied specimens were prepared in accordance to the ASTM E3 "Standard guide for preparation of metallographic specimens". Light optical microscopy was initially used to evaluate the evolution of the base metal microstructure owing to thermal effects during the welding process. Metallographic study was also carried out for the imaging of topographical and or general microstructural features at the regions of HAZ, FZ and BM as shown in Figure 4-6 and Figure 4-7 in § 4.3.1–2.

4.3.1 Optical light microscope microstructures of welded SAF2205 in the as-weld condition

Microstructural evolution of welded SAF2205 material in the condition of as-weld, and PWHT at 800℃/2h was studied to characterise the anticipated dual phases present in BM and the transformed intermetallic phases that might have nucleated at the regions of interest due to high thermal exposure introduced by the welding procedure, and subsequently exaggerated by the applied post weld heat treatment. Microstructural evolution of the BM to HAZ and the solidified welding consumables (FZ) were initially evaluated using the light illumination microscopy to assess the resultant micrographs at the specified regions of interest before and after 800℃/2h PWHT.

The analysed SAF2205 specimen, in the as-weld condition revealed the anticipated dual phase microstructure of austenite-γ comprising of twinning and ferrite-δ specifically at the region that was not thermally affected by welding operations–BM, as seen in [Figure 4-6 (a)]. The revealed microsructure of austenite-γ and ferrite-δ phases within the BM matrix comprised of elongated

grains, having approximately 50/50 percent ratio (δ/γ), thus denoting a well-balanced duplex structure.

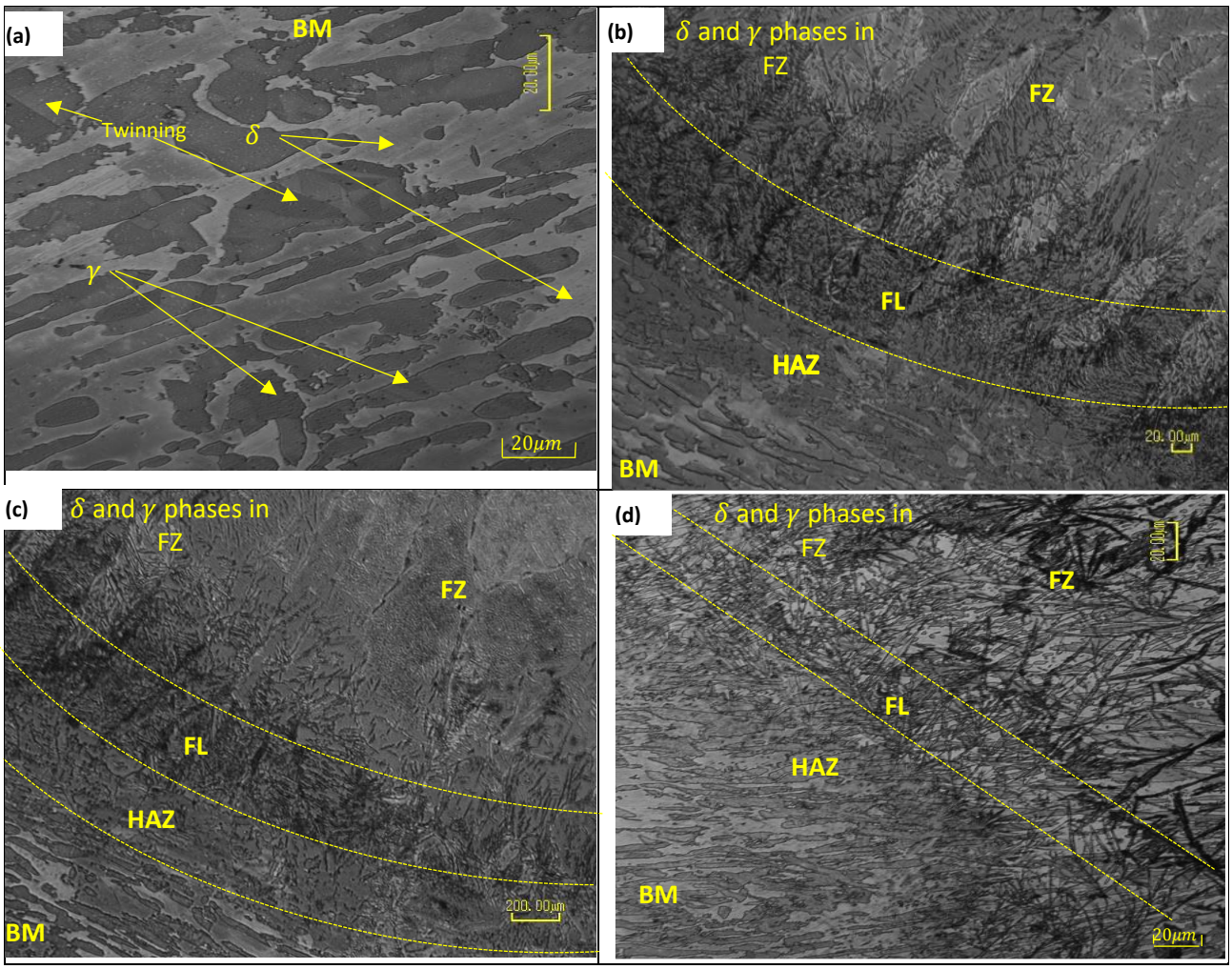

Figure 4-6: As-weld results (a) BM Microstructure–SAF2205: $\boldsymbol{\delta}$-Ferritic phase and $\boldsymbol{\gamma}$-Austenitic phase, (b) HAZ Microstructure– SAF2205, (c) FZ Microstructure–SAF2205, (d) BM, HAZ and BM microstructure–SAF2205

The SAF2205 weld metal – FZ micrographs was revealed using light microscopy and exhibited significant difference from those of the HAZ and BM as shown in [Figure 4-6 (b), (c) & (d)]. The weld microstructure at the FZ followed the ferrite-austenite solidification mode by forming ferrite-δ in the matrix immediately after the solidification promoted by the ferrite-δ forming elements (Cr, Mo and Si) within the weld metal. As the weld cools down to room temperature the austenite (γ)-precipitate nucleates in the ferrite (δ)-matrix in three forms of Widmanstätten structure of austenite-γ, grain boundary austenite-γ and intragranular austenite-γ grains. The elongated Widmanstätten structure of austenite (γ)-phase and the intragranular austenite-γ microstructure are presented at high magnification shown in [Figure 4-7 (b) & (e)] and [Figure 4-7 (c) & (f)] at the FZ. Solidified FZ comprised of varying grain sizes of dendritic nature.

4.3.2 Optical light microscope microstructures of welded SAF2205 PWHT at 800℃ for 2 hours

Post weld heat treated SAF2205 specimens in the conditions of 800℃ for 2 hours were tested to be prone to intergranular attack particularly at the weld regions of FZ and the HAZ, whereas the BM showed some level of ductility and not prone to intergranular attack during the bend qualification test, discussed in § 4.2.1. The FZ, HAZ and BM of SAF2205 specimen, PWHT at 800℃/2h, were examined further alongside the specimens that were in as-weld condition to compare the microstructural evaluation under the specified conditions, as seen in Figure 4-7 below.

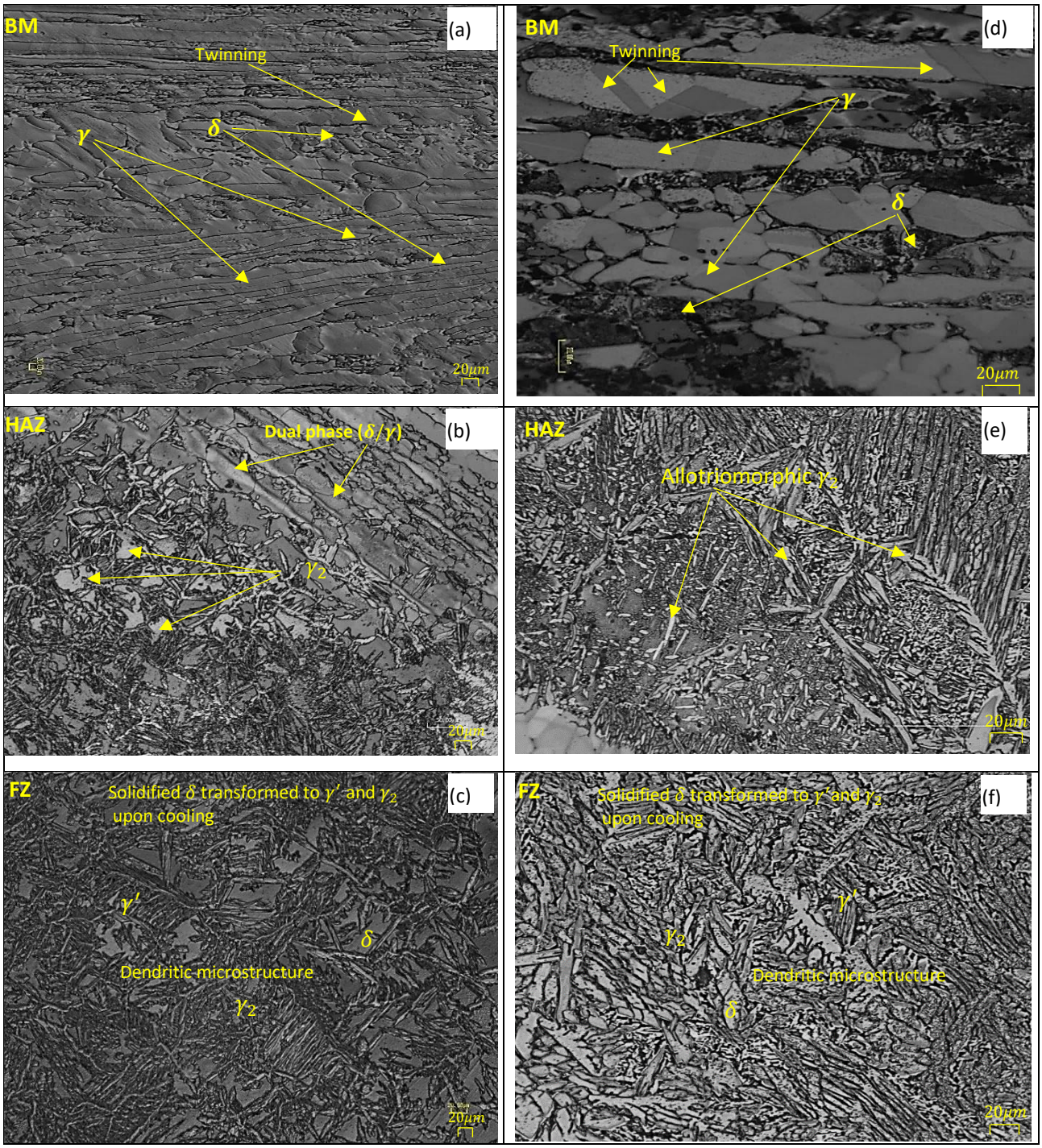

Figure 4-7: (a) BM Microstructure – SAF2205 in the as-weld condition showing δ-ferritic phase and γ-austenitic phase, (b) HAZ Microstructure – SAF2205 in the condition of as-weld, (c) FZ Microstructure – SAF2205 in the condition of as-weld, (d) BM Microstructure – SAF2205 PWHT at 800℃/2h, (e) HAZ Microstructure – SAF2205 PWHT at 800℃/2h, (f) FZ Microstructure – SAF2205 PWHT at 800℃/2h.

SAF2205 FZ specimens revealed microstructure comprising of primary austenite (γ') islands in ferritic (δ)-matrix shown in [Figure 4-7 (c)]. Whereas [Figure 4-7 (e)] exposed the allotropic austenite (γ') forming needle like morphology nucleated heterogeneously at ferrite-δ grain boundaries [Figure 4-7 (f)]. Secondary austenite (γ_2) nucleated and grew from the primary austenite (γ') which is known to take place through the following phase transformation: $\delta \rightarrow \gamma' \rightarrow \gamma_2$ was revealed in the form of solidified dendritic microstructure in the FZ.

4.3.3 Light microscopy analysis of AISI304 in the as-weld condition

Figure 4-8 presents the micrographs of the AISI304 weldment regions (FZ, HAZ and BM), revealed using the Nikon inverted metallurgical light microscope-ECLIPSE MA200, equipped with Nikon DS–L3 camera control unit for live imaging and image capturing. Microscope images were captured to distinguish the detailed microstructure of the specimens' field of view. The metallurgy of the AISI304 welded joint can be categorized into the evolving regions viz. FZ, HAZ and the unaffected BM, with Figure 4-8 clearly demonstrating the microstructural evolution of these specific regions.
The AISI304 BM microstructure revealed the single equiaxed austenite (γ)-phase and twinning shown in [Figure 4-8 (a) and (d)] below. The grains within the BM matrix of AISI304 specimen have uniform size not affected by thermal energy introduced at the FZ during welding. Adjacent to the BM is the regions that are affected by high temperature input during welding i.e. HAZ, Fusion Line (FL) and the solidified FZ. The FZ in the welded AISI304 specimen generally comprises of austenite-γ matrix and interspersed ferrite-δ precipitates from non-equilibrium rapid solidification condition (high cooling rate) causing incomplete transformation of ferritic-δ to austenite-γ. Thus, small amounts of ferrite-δ will remain within the weld microstructure at room temperature. The retained ferrite-δ is known to prevent solidification and hot cracking and it improves ductility, toughness and corrosion resistance of the weldments.

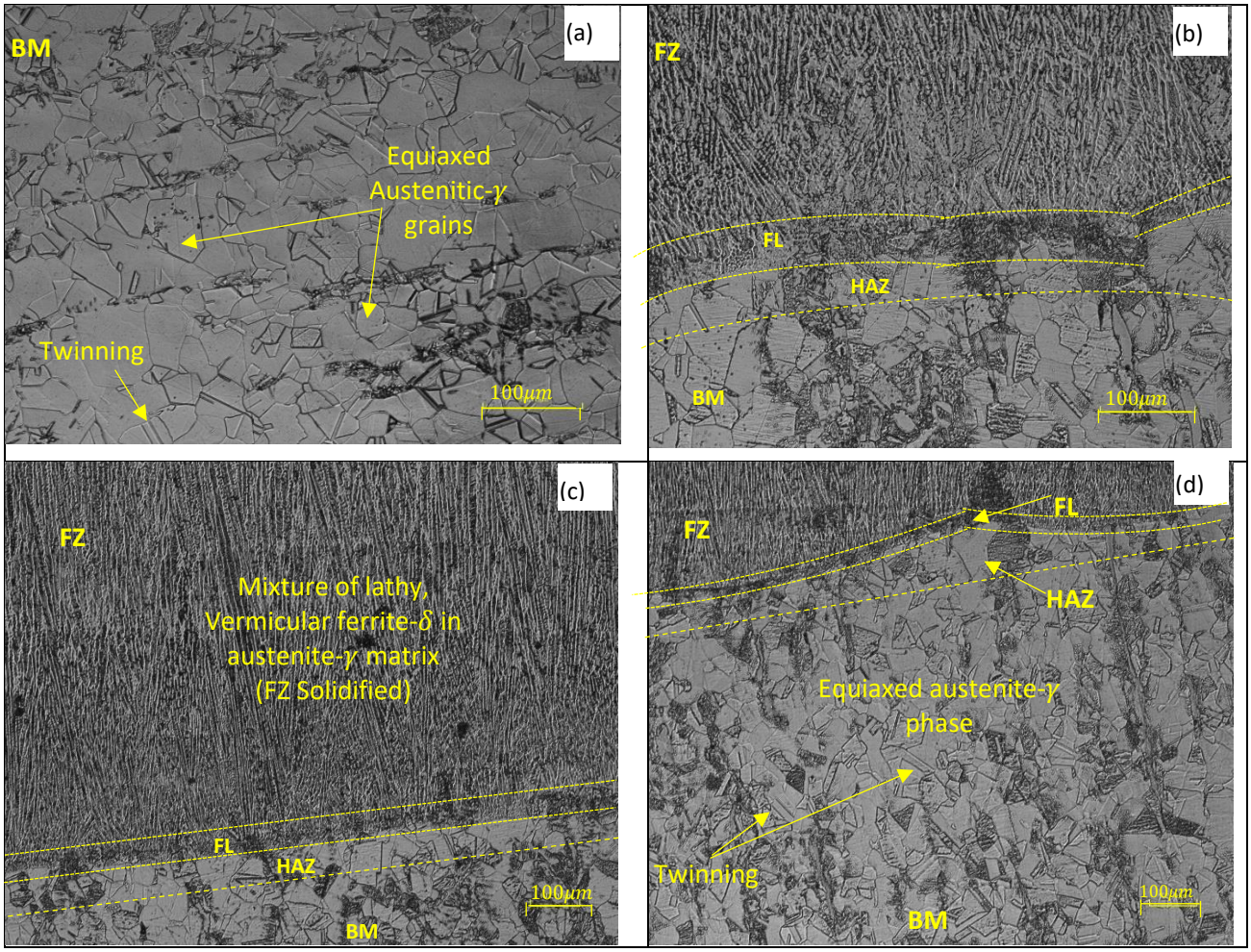

Figure 4-8: (a) BM Microstructure – austenitic single phase of AISI304, (b) HAZ Microstructure – AISI304, (c) FZ Microstructure – AISI304, (d) Evolution of AISI304 microstructure – FZ, BM and HAZ

4.3.4 Light microscopy analysis of AISI304 in the PWHT at 800℃/2h condition

The AISI304 specimens were further assessed for the conditions of as-weld and PWHT at 800℃/2h to analyse the consequence that the applied PWHT and welding thermal effect had on the material. The imaging results for AISI304 specimen in the specified conditions at the FZ, HAZ and the BM is shown in Figure 4-9 below.

As anticipated, the BM revealed a single-phase austenite-γ microstructure having the equiaxed grains of intermediate size and twinning as shown in [Figure 4-9 (a) and (d)]. The AISI304 specimens at the conditions of as-weld and PWHT revealed comparable microstructures within the BM matrix without any noticeable deviations that can be imaged by light microscopy.

The FZ can be considered as a mini casting forming columnar dendrites derived from the super-cooling taking place at the solid/liquid interface (BM-FZ interface) growing in the direction perpendicular to the BM [Figure 4-9 (e)]. The FZ microstructure in both conditions of as-weld and PWHT at 800℃/2h constitute mainly of austenite-γ under equilibrium solidification conditions. There was no obvious difference identified between the examined specimens at the FZ when analysed using light microscopy. However, the HAZ interface with the FZ (HAZ-FZ interface) and the FL could

be distinguished [Figure 4-9 (e)]. The FZ microstructure for AISI304 grade also showed lamellar mixture of vermicular/skeletal ferrite-δ morphology and lathy ferrite-δ morphology (Figure 4-8 and Figure 4-9). The anticipated carbides ($Cr_{23}C_6$) transformation at the AISI304 specimens' HAZ, in the conditions of as-weld, and 800℃/2h PWHT intended to exaggerate segregation to take place could not be characterised or identified using light microscopy technique (Figure 4-9).

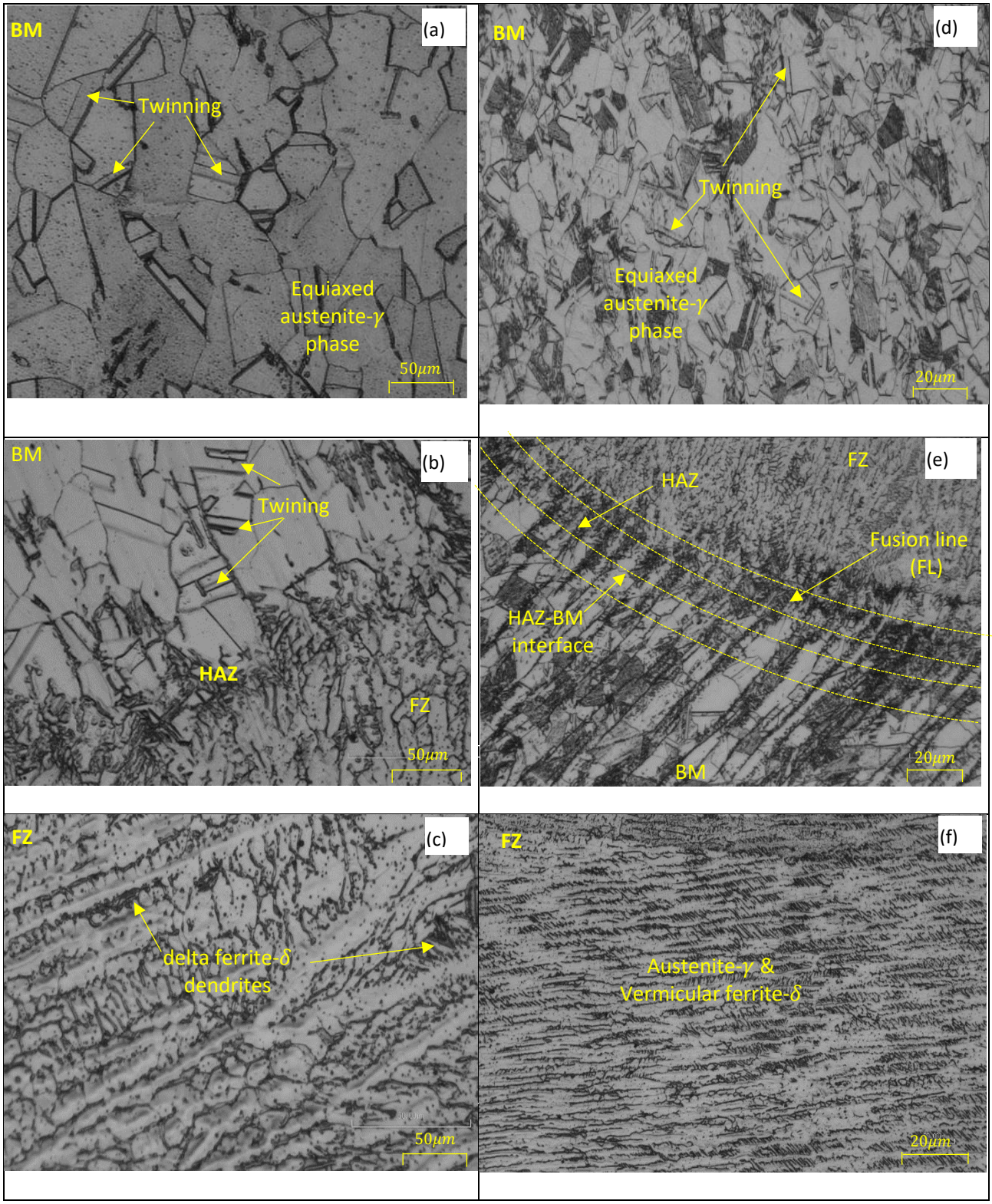

Figure 4-9: (a) AISI304 specimens in the As-weld condition (a) BM microstructure, (b) HAZ microstructure and (c) FZ Microstructure, AISI304 specimens that are PWHT at 800℃/2h (d) BM Microstructure, (e) HAZ Microstructure and (f) FZ Microstructure.

The AISI304 material demonstrated the ductile properties during the intergranular attack tests without crack failure but showed to be prone to corrosion during cyclic corrosion test showing pits and corrosion products, whereas the SAF2205 material behaved differently to AISI304 material in both corrosion tests. The SAF2205 material, PWHT at 800℃/2h demonstrated crack failure at the FZ and HAZ proving to be susceptible to intergranular attack, at the same time this material illustrated

good corrosion resistance properties during the long-term exposure in the salt chamber. The SAF2205 specimens at specified conditions were tested to be susceptible to intergranular attack informed by the material sudden crack failure, whereas the AISI304 grades demonstrated ductile properties when exposed to similar conditions. A detailed analysis for the failed SAF2205 specimens at the FZ and HAZ were further carried out using SEM-EDS and SEM-BSE technique.

4.3.5 Scanning electron microscopy (SEM) microstructure analysis of 800℃/2h PWHT SAF2205

The SEM approach using BSE and EDS was applied to analyse the SAF2205 specimens that were PWHT at 800℃/2h to reveal more information about material composition contrast and evolution of microstructural features for the welded regions (FZ, HAZ and BM) at a higher magnification than it was possible with the use of the light microscope technique. The SAF2205 specimens PWHT at 800℃/2h were evaluated to be prone to intergranular attack at the FZ and HAZ, as can be seen in Table 15 (f) and Table 16 (f) respectively. These regions are known to have had secondary phases nucleated due to thermal energy introduced at the FZ during welding operations and the PWHT intended to exaggerate transformation of these phases.

There was minor corrosion indications on the SAF2205 specimens PWHT at 800℃/2h during the cyclic corrosion exposure test (Table 13: Figure 4-3), but not as severe compared to the AISI304 specimens exposed to similar conditions. Thus, further analysis of SAF2205 specimens PWHT at 800℃/2h using SEM technique was necessary to acquire finer details i.e. elemental compositions, material composition contrast and topographic information at the areas of interest.

The SEM technique was accomplished by scanning the specimen's surface with a focused beam at the beam accelerating voltage of 20keV. By virtue of its smaller wavelength electrons can resolve finer features of the analysed specimens to a much greater extent compared with visible light. The electron beam interacts with the specimen producing various signals detected by the SEM-BSE and or SEM-EDS detectors for topographic information, elemental composition and composition contrast of the compound. The position of the beam and the intensity of the detected signal generate an image with different atomic number contrast enabling the identification of phases present within SAF2205 specimens' field of view i.e. the formed secondary phases and dual phases.

4.3.5.1 SEM-BSE analysis of 800℃/2h post weld heat treated SAF2205 specimen

The scanning electron microscopy launched with back scatter electron detectors (SEM-BSE) was initially used to analyse SAF2205 etched specimens. The SEM-BSE examination for the 800℃/2h PWHT SAF2205 specimens was conducted on the 10N NaOH electro-etched specimen to expose

the revealed microstructural information at a higher magnification than it was plausible with the use of light illuminated microscope specifically at the regions described in the preceding section.

Specimens were initially prepared by thinly coating with the electrically conductive film of carbon layer using Balzer's sputter coater before to them being analysed using SEM-BSE. The revealed micrographs at the weld regions of BM, FZ and HAZ are presented in [Figure 4-10 (a)-(f)].

The SEM-BSE base metal (BM) images presented in [Figure 4-10 (a) & (b)], revealed composition contrast between microstructure of the anticipated dual phases of austenite-γ and ferrite-δ. The revealed microstructure comprises of elongated islands and small clusters of austenite-γ in ferrite-δ matrix, having highly contrasted grains and grain boundaries. As stated previously that the welds (FZ) first solidifies as ferrite-δ and upon further cooling the austenite-γ phase precipitate at the ferrite-δ grain boundaries by means of solid phase transformation to develop the duplex structure. The FZ [Figure 4-10 (e) and (f)] could not reveal much detailed information regarding the specifics of the solidified and the formed phases constituents within the analysed zone when SEM-BSE is deployed, although combination of columnar and equiaxed dendrites were observed to have been developed from the weld metal solidification process. The HAZ region [Figure 4-10 (c) and (d)] revealed twinning contrast within the austenitic-γ microstructure. The secondary phases (sigma-σ and chi-χ) were identified to nucleate heterogeneously at the grain boundaries. The sigma σ-phase were observed to preferentially nucleate at the ferrite/ferrite/austenite ($\delta/\delta/\gamma$) triple points or grow along ferrite/ferrite (δ/δ) boundaries and the phase-χ precipitate on ferrite/ferrite (δ/δ) grain boundaries [Figure 4-10 (d)]. The chi χ-phase is present in smaller quantities than the sigma σ-phase as it is a metastable phase consumed during sigma σ-phase transformation. Although the formed secondary phases could be identified using SEM-BSE at the nucleating site and through the variation of material composition contrast or atomic number contrast the SEM-EDS/EDX analysis was further deployed to provide finer details for the analysed regions in order to validate the identified secondary phases chemical compositions.

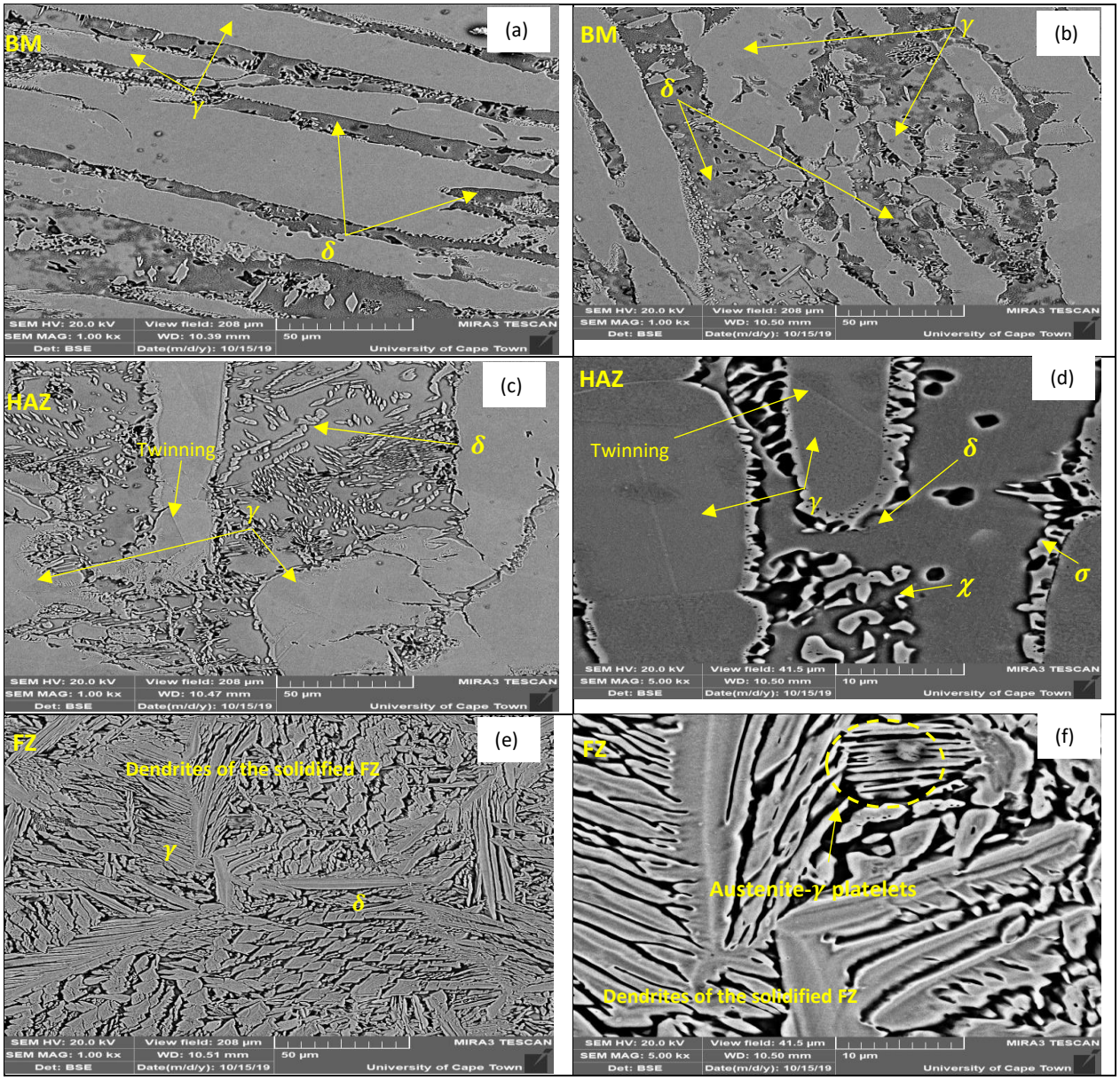

Figure 4-10: SEM-BSE images after PWHT at 800℃ for 2 hours: (a) & (b) BM showing the balanced phases of γ-phase with twinning and δ-phase, (c) & (d) HAZ showing the growth of intermetallic at the grain boundary growing into the δ-phase, (e) & (f) Dendritic solidification of filler metal forming.

4.3.5.2 Energy dispersive X-ray spectroscopy (SEM-EDS) for 800℃/2h PWHT SAF2205 specimens

Energy Dispersive Spectroscopy (SEM-EDS) was employed to evaluate and characterise the dual phases of austenite-γ and ferrite-δ and to identify and characterise the secondary phases (chi-χ and sigma-σ), non-metallic inclusions and other distinguishable features which transformed during welding operations and were exaggerated by post-weld thermal aging treatments of SAF2205 at 800℃/2h. SEM-EDS analysis technique was preferred because of its built-in capability to rapidly evaluate considerable field of view and also the specimen preparation to complete this type of analysis was found to be much simpler in comparison to transmission electron microscopy (TEM).

4.3.6 Determination of SEM-EDS operational settings for SAF2205 analysis

The accuracy of SEM-EDS, both qualitative and quantitative analysis is a direct function of combination of several factors such as the adequate operational control of parameters and EDS spectrum characteristics. Apart from the SEM instrument capability, the quality of EDS spectrum and the machine accuracy can be improved by manipulating operable parameters such as acquisition time, dead time and beam current [51]. In order to establish SEM-EDS settings for correct and accurate operational control of parameters, SAF2205 specimen in the as-received condition was analysed at a pre-selected field of view to obtain the overall elemental composition of the base metal [Figure 4-11 (a)]. The alloying elemental compositions for SAF2205 BM in the as received condition was analysed by varying the acquisition times from 30s at the time incremental of 30s until 240s. The alloying elemental compositions of 23.3wt.%Cr, 5.3wt.%Ni, 2.0wt.%Mn, 3.5wt.%Mo, 0.5wt.%Si and 65.5wt.%Fe were analysed and demonstrated to be consist and accurate at 90s acquisition time as can be seen in [Figure **4-12** (b)-(g)]. The operational control of parameters of 90s acquisition time, 4.5 spot size and 12-15% dead time at the accelerating voltage of 20keV was set in order to analyse the elemental composition range of SAF2205 BM (as-received) dual phases of ferrite-δ and austenite-γ, as shown in Appendix D: Austenite-γ,1-4 and ferrite-δ, 5-8.

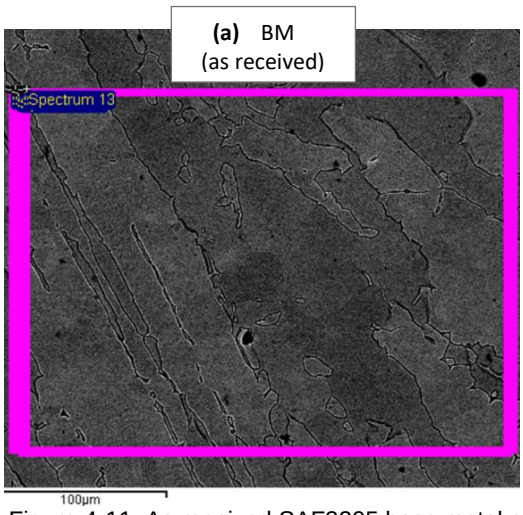

Spectrum	Si (wt.%)	Cr (wt.%)	Mn (wt.%)	Fe (wt.%)	Ni (wt.%)	Mo (wt.%)	Time (s)
6	0.5	23.4	1.7	65.7	5.2	3.5	30
7	0.5	23.3	2.0	65.4	5.3	3.6	60
8	**0.5**	**23.3**	**2.0**	**65.5**	**5.3**	**3.5**	**90**
9	0.5	23.3	1.9	65.5	5.3	3.5	120
10	0.5	23.3	2.0	65.4	5.4	3.5	150
11	0.5	23.3	2.0	5.5	5.3	3.5	240
Average	**0.5**	**23.3**	**1.9**	**65.5**	**5.3**	**3.5**	

Figure 4-11: As-received SAF2205 base metal elemental composition analysis

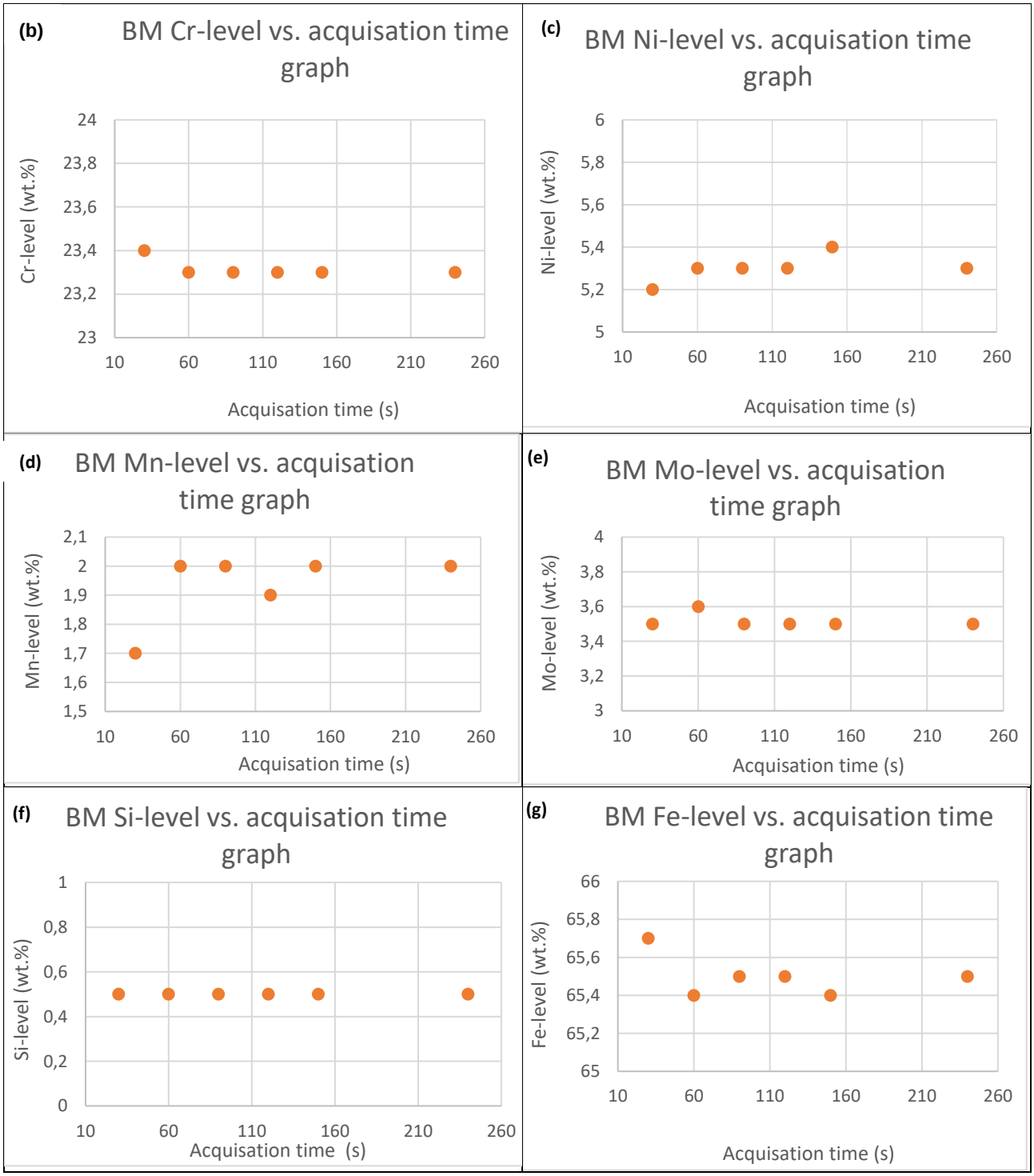

Figure 4-12: SAF2205 as-received base material acquisition time for individual alloying elements of Cr, Ni, Mn, Mo, Si and Fe in (wt.%)

4.3.6.1 SEM-EDS results for determination of elemental compositions for dual structure of austenite-γ and ferritic-δ phases

SEM-EDS operational control settings cited in the preceding section (§ 4.3.6) were employed on the as-received SAF2205 BM to determine the specimen alloying element compositional range within the duplex structure; this is to be used as the basis to identify the formation of other secondary phases (see Appendixes D: 1 to 8). The alloying elemental data was statistically gathered from each

phase (δ and γ) and analysed by means of confidence interval determination of the obtained set of data. Statistical analysis for the elemental composition range within the austenite-γ and ferrite-δ phase is presented in Appendix D:1-4 for austenite-γ and 5-8 for ferrite-δ, summarised in Table 18 below. The determined elemental range was used as a guide to identify and categorise the formed secondary phases by comparing the statistical elemental range of the dual phases (ferrite-δ and austenite-γ) with the elemental compositions of the secondary phases (Sigma-σ and Chi-χ). The identified secondary phases were further distinguished as σ-phase and χ-phase by comparing Mo-element and Cr-element compositions, whereby the ferrite-δ former elements viz. Mo, Cr and Si, rapidly leads to the formation of the intermetallic phases, with χ-phase having high Mo-element content (15-19wt.%Mo) in comparison with the σ-phase (6-10wt.%Mo). The content of Cr-element in χ-phase ranges between 24-25wt.%Cr, and in σ-phase is between 25-29wt.%Cr. The Ni-element content in χ-phase was analysed to be 3wt.%Ni and in σ-phase was analysed to be at a range of 3-4wt.%Ni

Table 18: SAF2205 as received BM elemental compositions range of SAF2205 PWHT at 800℃/2h

Cr-element range (wt.%)	**Ni-element range (wt.%)**	**Mo-element range (wt.%)**	**Mn-element range (wt.%)**
Austenite (γ)-phase			
21.6–22	6.40–6.7	2.6–3.2	2.0–2.1
Ferrite (δ)-phase			
24.2–24.8	4.10–4.6	4.2–4.4	1.7–1.8

4.3.6.2 EDS results for SAF2205 heat treated material

Energy Dispersive Spectroscopy (EDX/EDS) was completed on the 800℃/2h heat treated SAF2205 comparing the elemental composition information with that of SAF2205 BM in the as received condition, for analysis of the different microstructural phases and compounds which may have been transformed during welding operations and thermal aging in the BM, HAZ and FZ.

SEM-EDS microstructural imaging in the BM (Figure 4-13) revealed the dual phase contrast of ferrite-δ and austenite-γ comparable with the optical microscopy and SEM-BSE imaged results [Figure 4-7 (a) and (d)]. The specimens were initially surface prepared using electro etching technique with the electrolyte of NaOH at a concentration of 10N. This procedure could not reveal the anticipated intermetallic phases that might have nucleated at the weld zones during SEM-EDS analysis. Thus the usage of NaOH solution to electro etch preferentially dissolved the intermetallic phases without affecting the duplex phases of ferrite-δ and austenite-γ (Figure 4-11), hence the latter phases were successfully imaged. The specimens were then re-polished to restore the surface to its original unetched state, as per ASTM E3 “standard guide for preparation of metallographic specimens”. The as-polished unetched specimens were unmounted from the resin mount for SEM-EDS analysis preparation as explained in § 3.6.2.1. This action was followed by repeating SEM-EDS analysis whereby the intermetallic phases were successfully revealed with the alloying elemental

compositions that are not within (δ and γ) phases range (Table **18**). Figure 4-13–BM, Figure 4-15–FZ and Figure 4-17–HAZ, demonstrate the sites where the bright secondary phases have preferentially nucleated at the weld regions of SAF2205 that was PWHT at 800℃/2h. The EDS-maps for the welded regions (Figure 4-14–BM, Figure 4-16–FZ, Figure 4-18–HAZ) showed the high intensity atomic number contrast of Ni, Cr and Mo elements within the pre-selected field of view. The base metal SEM-EDS micrographs (Figure 4-13) revealed the anticipated dual phases of ferrite-δ and austenite-γ similar to the light microscope and SEM-BSE results. The SEM-EDS technique provided additional information for elemental composition analysis. The compositional information for the SAF2205 base metal PWHT at 800℃/2h revealed the austenite γ-phase having compositions of 6wt.%Ni and 3wt.%Mo that are within the γ-phase range (Table **18**), whereas the δ-phase was analysed to have 24wt.%Cr content and relatively higher Mo-element (5wt.%Mo) as they are ferrite-δ forming elements (Figure 4-13).

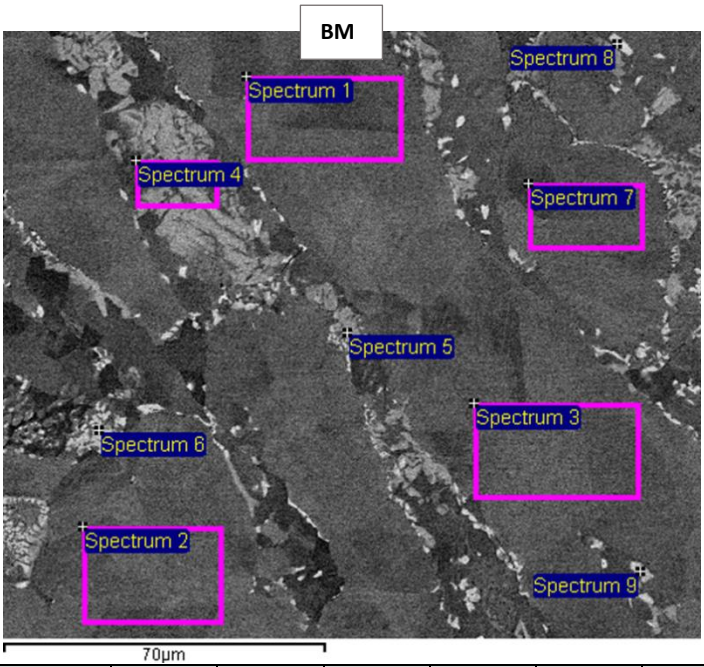

Spectrum	Si (wt.%)	Cr (wt.%)	Mn (wt.%)	Ni (wt.%)	Mo (wt.%)	Phase ID.
1	0.50	22.18	2.2	6.21	2.89	γ
2	0.41	21.81	2.23	6.22	2.88	γ
3	0.44	22.02	2.12	6.32	2.80	γ
4	0.49	25.88	1.71	3.74	5.48	δ
5	0.56	27.40	2.03	4.10	6.74	σ
6	0.53	21.51	2.10	5.96	4.95	δ
7	0.39	22.00	2.03	6.20	2.77	γ
8	0.55	25.39	1.85	3.49	3.58	δ
9	0.55	26.51	2.08	4.39	6.63	σ

Figure 4-13: Microstructural analysis of the post weld heat treated SAF2205 BM specimen at 800℃/2h: SEM-BSE image (Top) and elemental composition analysis of the dual phases of ferrite ($\boldsymbol{\delta}$) and austenite($\boldsymbol{\gamma}$) at the BM (Bottom)f

SEM-BSE micrographs revealed compositional contrast or atomic number contrast representing the phases present in the analysed field of view. The SEM-BSE imaging produced from atomic number contrasting was significant to identify any developed intermetallics or secondary phases at the pre-selected field of view within the SAF2205 specimens which was previously PWHT at 800℃/2h. The atomic number contrast effect allowed the identification of secondary phases at the specific regions of HAZ–FZ and HAZ–BM interfaces, grain boundaries and triple points nucleating sites. The formed secondary phases (sigma-σ and ferrite-χ) were detected to be saturated at the nucleating sites and at the points of defects, comprising of a distinct atomic number contrast from the BSE (Figure 4-14). The varying atomic number contrast within the secondary phases (sigma-σ and ferrite-χ) and the dual phases (ferrite-δ and austenite-γ) is caused by the presence of high-levels of heavy metals with high atomic numbers causing great backscattering effect of BSE. The analysed secondary phases (chi-χ and sigma-σ) demonstrated to comprise of high atomic number elements (Mo, Cr and Ni) with different concentrations. The chi (χ) phase contain: 15-19wt.%Mo, 24-25wt.%Cr and 2.8-3wt.%Ni and the sigma (σ)-phase contains: 6-10wt.%Mo, 24-29wt.%Cr and 3-5wt.%Ni. The Mo-element is the heaviest alloying element followed by Ni-element and then Cr-element within the SAF2205 material. The compositions of Mo-element, Cr-element and Ni-element in chi-χ phase cause this phase to have a high degree of elastic scattering resulting in high angles of deflection and large backscattering effect [52]. Since the analysed phases (chi-χ, sigma-σ, austenite-γ and ferrite-δ) contains varying compositions of heavy metals with different atomic numbers, the phases will also exhibit different values of backscatter coefficient. As a result the contrasting effect of the secondary phase (chi-χ and sigma-σ) appears to be relatively brighter due to a larger number of backscatter electrons ejecting out of these phases, while the phases with a low atomic number (austenite-γ and ferrite-δ) will appear relatively dark.

The SEM-EDS maps revealed the nonuniform compositional contrast owing to the difference in heavy metals compositions within the analysed field of view. The high elemental atomic number contrast has effected regions with high Mo-element , Ni-element and Cr-element level associated with the transformed phases of Chi-χ and Sigma-σ.The formed phases (Chi-χ and Sigma-σ) are revealed by SEM-EDS maps distinctly showing their nucleation sites viz. ferrite/ferrite/austenite ($\delta/\delta/\gamma$) triple point and ferrite/austenite (δ/γ) grain boundaries as seen in Figure **4**-**14** (a) to (d).

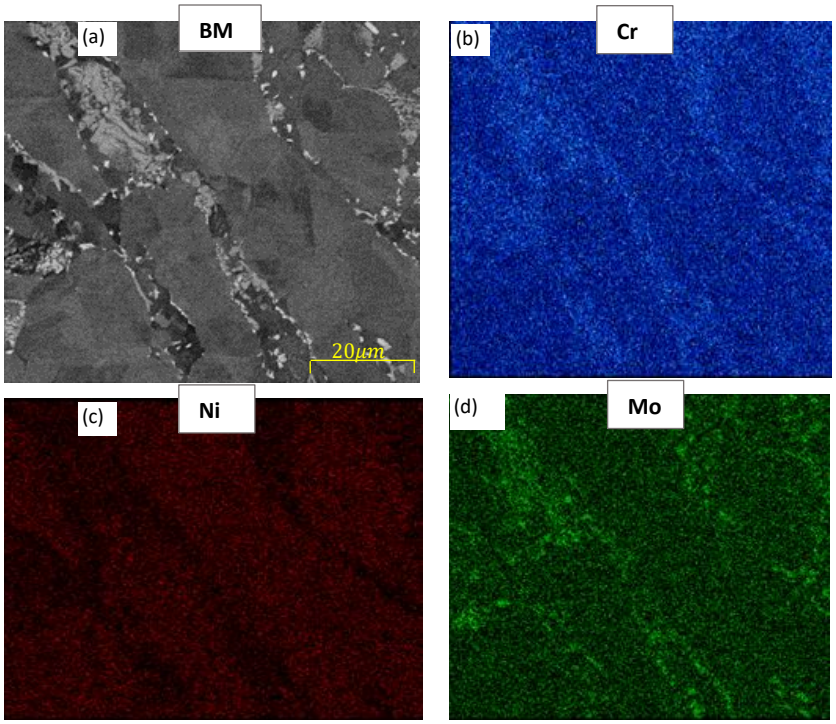

Figure 4-14: (a) Field of view for SAF2205 and PWHT800℃/2h at the BM, (b) Cr-elemental SEM-EDS map, (c) Ni-elemental SEM-EDS ma (d) Mo-elemental SEM-EDS map

The microstructural analysis for SAF2205 FZ specimens PWHT at 800℃/2h successfully revealed the austenite (γ)-phase as predominant than the ferrite (δ)-phase, thus demonstrating to have unbalanced dual structure within the FZ matrix (Figure 4-15). The weldments of SAF2205 solidify as ferrite-δ because of high diffusivity of Cr-element and Mo-element in the ferrite (δ)-phase [53].The austenite (γ)-phase is transformed upon further cooling of solidified ferritic (δ)-phase to room temperature during the weld thermal cycle. The sigma (σ)-phase was also identified at the highly energised nucleation sites of austenite-γ and ferrite-δ grain boundaries. The secondary phase (sigma-σ) was identified comprising of high Cr and Mo levels which analysed to be outside of γ-phase and δ-phase elemental composition range (Table 18). The Chi-χ could be not be detected at the preselected spot or field of view. The solidified weld metal microstructure (FZ) exposed also the surface defects of minute voids scattered on the SAF2205 FZ specimen surface, as seen in Figure 4-15 and Figure 4-16 (a).

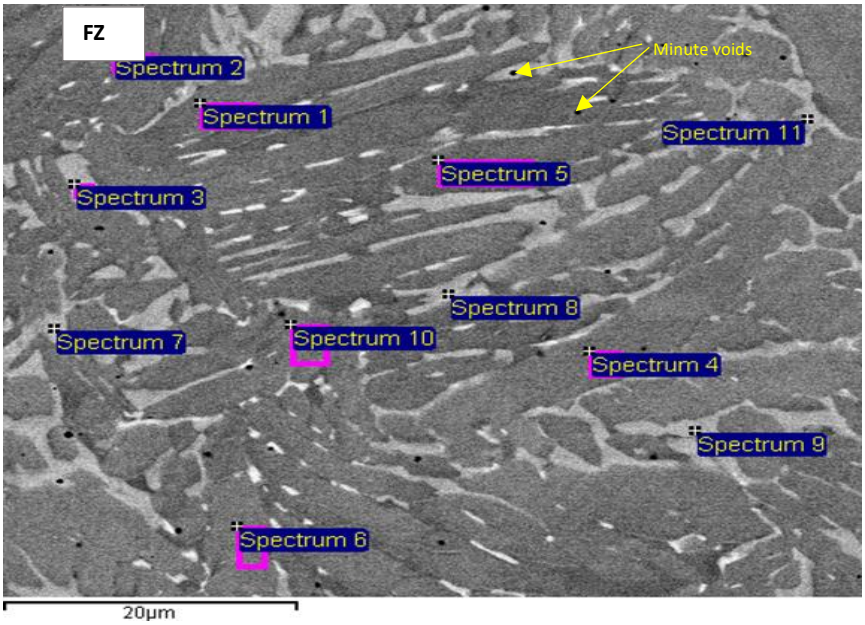

Spectrum	Si (wt.%)	Cr (wt.%)	Mn (wt.%)	Ni (wt.%)	Mo (wt.%)	Phase ID.
1	0.59	23.29	1.38	8.09	2.88	γ
2	0.65	23.55	1.42	7.72	3.42	γ
3	0.89	29.69	1.22	3.79	8.38	σ
4	0.61	23.27	1.40	7.96	3.49	γ
5	0.58	22.76	1.39	8.82	3.33	γ
6	0.64	23.29	1.35	7.95	3.57	γ
7	0.87	29.25	1.26	4.10	7.53	σ
8	0.56	24.10	1.90	4.34	4.22	δ
9	0.52	24.30	1.80	4.40	3.99	δ
10	0.67	23.26	1.45	7.59	3.57	γ
11	0.50	24.50	1.77	4.35	4.30	δ

Figure 4-15: SEM-EDS analysis of the SAF2205 FZ, PWHT800℃/2h (Top) and the elemental analysis (Bottom)

The solidified SAF2205 weld metal–FZ PWHT at 800℃/2h has not revealed the presence of Chi (χ)-phase; rather the presence of sigma (σ)-phase in small amounts which preferentially nucleated at the grain boundary of the solidified dendritic and restructured Widmanstätten plates of γ-phase. The identified austenite (γ)-phase was characterised to be within the defined elemental composition range with less amount of ferrite (δ)-phase detected.

SEM-EDS elemental maps showed the intensity of heavy metals found in the analysed phases (austenite-γ, sigma-σ and ferrite-δ) of the 800℃/2h post weld heat treated SAF2205 FZ, shown in Figure 4-16: (b) Cr-element, (c) Mo-element and (d) Ni-element. The elemental intensity within the analysed field of view illustrated inhomogeneous contrasting effect distributed evenly within the solidified weld consumables, but because of the predominate austenitic (γ)-phase having small amount of the ferritic (δ)-phase other formed phases i.e. sigma (σ)-phase could not be contrasted, as seen in elemental SEM-EDS map [Figure 4-16 (c), (b) and (d)]

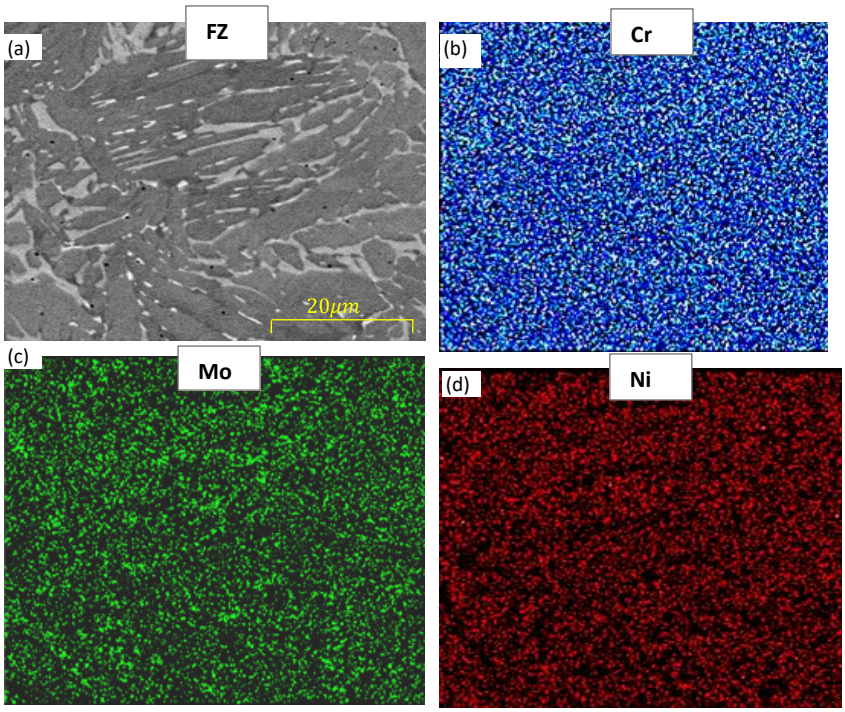

Figure 4-16: (a) Field of view for the SAF2205 and PWHT800℃/2h at the FZ, (b) Cr-elemental SEM-EDS map, (c) Mo-elemental SEM-EDS map, (d) Ni-elemental SEM-EDS map

The micrographs of the SAF2205 HAZ that was isothermally aged at 800℃ for 2 hours is presented in Figure 4-17 and Figure 4-18 (a), showing the high effect of compositional contrast or atomic number contrast of intermetallic sigma (σ)-phase precipitating at the highly energised grain boundary of ferrite/austenite (δ/γ) and of chi (χ)-phase at the ferrite/sigma (δ/σ) growing by expanding exclusively in the ferrite (δ)-matrix. The Chi (χ)-phase is also identified at the triple points and within the ferrite (δ)-grains at which it adopts a very bright contrasted hexagonal shape as illustrated in Figure 4-17 and Figure 4-18 (a).

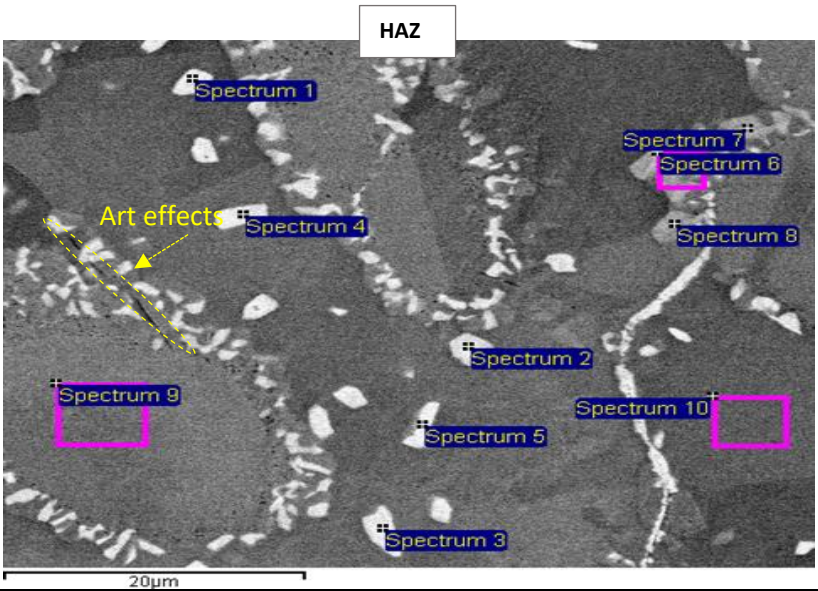

Spectrum	Si (wt.%)	Cr (wt.%)	Mn (wt.%)	Ni (wt.%)	Mo (wt.%)	Phase ID.
1	0.68	24.91	1.97	2.87	18.52	χ
2	0.63	24.91	1.77	2.80	15.98	χ
3	0.67	24.6	2.01	2.80	17.89	χ
4	0.55	24.78	1.82	3.40	10.82	σ
5	0.60	24.92	1.70	2.90	15.16	χ
6	0.55	25.06	2.00	4.40	6.19	σ
7	0.44	21.99	2.16	6.36	3.16	γ
8	0.54	24.62	2.1	4.35	7.24	σ
9	0.46	21.99	2.11	6.31	2.75	γ
10	0.45	25.32	1.87	3.86	3.67	δ

Figure 4-17: SEM-EDS spectrum analysis showing the HAZ of the welded SAF2205, PWHT800℃/2h (Top), elemental analysis (Bottom)

The sigma (σ) and chi (χ) phases – Figure 4-17 are enriched with Cr and Mo having lower Ni-element when compared to the duplex structure of austenitic-γ and ferritic-δ . The ferrite-δ stabilizing elements (Cr and Mo) were altered during welding followed by isothermal aging at 800℃/2h affecting weld joint properties and the adjacent weld zones (HAZ). High levels of Mo-element (chi-χ:17wt.%Mo and sigma-σ: 8wt.%Mo) was analysed particularly at the grain boundary with elemental composition matching those of secondary phases, growing towards the ferrite (δ)-phase and some within the grains as seen in Figure 4-18 (a). The Chi (χ)-phase was identified by the brighter contrast effected by the atomic number contrast [Figure 4-18 (a) and (d)] due to the high concentration of heavier Mo-element. The sigma (σ)-phase was also identified as having Ni-element content that is higher (4wt.%Ni) than Chi (χ)-phase (3wt.%Ni), and high Mo-element but not as high as in the chi (χ)-phase. The varying elemental concentrations of the transformed secondary phases created different contrast permitting the phase identification during microstructural analysis. The different contrast of the duplex phase (austenite-γ and ferrite-δ) and secondary phases (sigma-σ and chi-χ) can also be seen from SEM-EDS map [Figure 4-18 (b), (c) & (d)]. The SEM-EDS map show the austenite(γ)-grains with high level of Ni-element, whereas the ferrite (δ)-grains contain high Cr-element with minor variation in Mo-element level as it can be seen with the inhomogeneous contrast intensity within the

grains [Figure 4-18 (a) to (d)]. As mentioned previously, sigma (σ)-phase and chi-(χ) phase are enriched with elements of ferrite-δ formers (Cr and Mo).

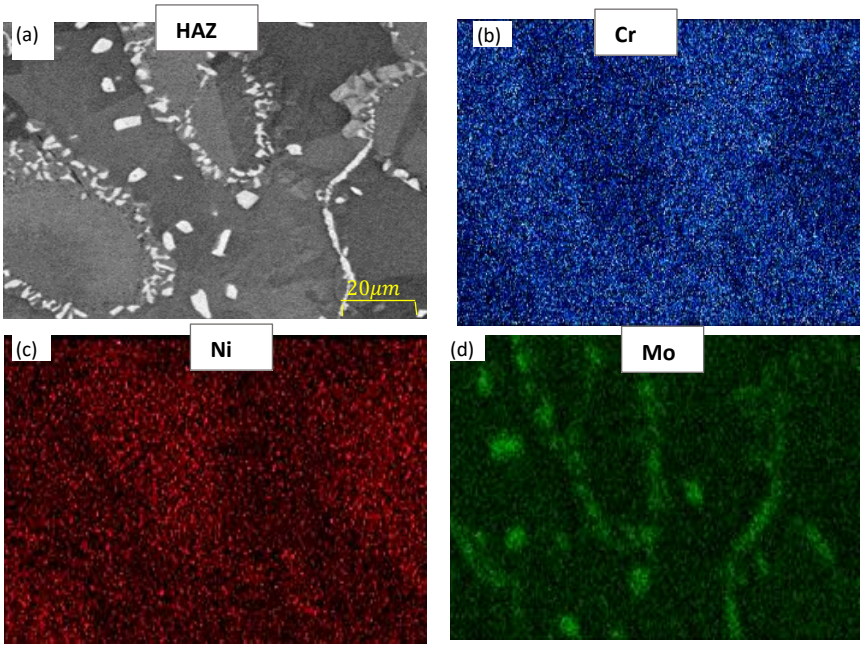

Figure 4-18: (a) Field of view for the SAF2205 that was PWHT800℃/2h at the HAZ, (b) Cr-elemental SEM-EDS map, (c) Ni-elemental SEM-EDS map, (d) Mo-elemental SEM-EDS map

CHAPTER 5 : CONCLUSIONS AND FINDINGS

1. The SCC salt spray exposure test results confirmed that when AISI304 and SAF2205 weldments are exposed to similar accelerated laboratory conditions simulating saline conditions the electro-chemical reaction is faster in AISI304 grades than in SAF2205 grades because of the minute cracks and corrosion pits accompanied by corrosion products that were detected for the AISI304 grades. The indications of pitting and corrosion products manifested during the first three to four months of corrosion exposure tests and initiated at the welded stressed regions of the isothermally aged (800℃/2h and 500℃/3h) and as-weld AISI304 specimens with no indications of such defects on SAF2205 specimens.
2. The welded regions (FZ) of SAF2205 grades in the as-weld and 500℃/3h PWHT condition demonstrated no indications of corrosion, neither in a form of pits nor cracks and associated corrosion products, throughout the cyclic corrosion testing period of ten months. Conversely, the 800℃/2h PWHT SAF2205 specimens revealed minor corrosion products during the fifth month of being exposed to similar conditions, degrading the material at the slowest rate until the termination of the tests after month ten.
3. The welded regions (HAZ and FZ), including the unaffected BM for AISI304 grade, did not suffer intergranular attack in the material conditions of as-weld, heat treatment at 500℃/3h and 800℃/2h, as demonstrated by the excellent ductile property at the conclusion of the intergranular attack qualification test. The tested weld regions did not suffer sensitisation
4. The SAF2205 welded regions of HAZ and FZ which were heat treated at 800℃/2h demonstrated to be susceptible to Intergranular attack, which was different to the base metal (BM). During the Intergranular attack qualification test (bend test) the SAF2205 specimens (HAZ and FZ) PWHT at 800℃/2h crack failed without demonstrating plastic deformation. Instead the crack failure for the tested FZ and HAZ was of a brittle fracture, owing to the ferrite matrix which undergoes decomposition process when aged at 800℃/2h, thus forming the brittle intermetallic phases at the HAZ extending to the HAZ-FZ interface. On the other hand, the SAF2205 BM exposed to similar conditions did not suffer similar defects.
5. The use of light microscopy to examine the SAF2205 base metal, PWHT at 800℃/2h only revealed the anticipated balanced dual phase microstructure of ferrite-δ and austenite-γ within the BM matrix, hence it did not suffer the intergranular attack. The intergranular affected weld region of FZ demonstrated the heterogeneous dendritic and columnar grains owing to the solidification nature of the weld metal. This analysing technique (light microscopy) was not beneficial in revealing other phases i.e. the brittle secondary phases within the HAZ and FZ matrix.

6. SEM-BSE was employed with the intent to reveal the resultant detrimental/brittle secondary phases at the HAZ and FZ weld region for the SAF2205 specimen that was PWT at 800℃/2h and electro etched using 10N NaOH. The SEM-BSE techniques successfully revealed the duplex structure (ferrite-δ and austenite-γ), without exposing the transformed intermetallic phases. The etching technique preferentially dissolved the intermetallic phases without affecting the duplex microstructure which was effectively imaged. The SEM-BSE was able to reveal the single austenite equiaxed grains comprising of twinning within the AISI304 BM matrix without any additional information of the sensitised region constituents.
7. Unetched specimens (as-polished) were analysed using SEM-EDS technique, revealing the detrimental/ brittle intermetallic phases (sigma-σ and chi-χ) at the highly energised nucleation sites of the grain boundaries, triple point and incoherent twin boundaries. The intermetallic phases were also identified to be growing within the ferrite-δ matrix thus depleting the grain boundaries from crucial elements (Mo and Cr) added to improve mechanical properties and corrosion resistance. The secondary phases were revealed in the SAF2205 specimen weld zones viz. HAZ and FZ that were subjected to the heat treatment of 800℃/2h. The HAZ was analysed to have the χ-phase identified to contain high concentrations of Mo and Cr elements. The detected σ-phase was identified having high level of Cr and Ni elements. The intermetallic compounds (chi-χ and sigma-σ) enriched with the ferrite-δ stabilising elements (Mo and Cr) themselves are brittle, and because of their presence, they initiated brittle cracks of the material.

CHAPTER 6 : RECOMMENDATIONS FOR FURTHER RESEARCH

1. When time is not a factor the longer specimens exposure durations exceeding 10 months should be applied to increase the prospect of deteriorating the tested materials (AISI304 and SAF 2205) even further in order to demonstrate the SCC defects of cracks at the sensitised regions, differently other methodologies for accelerated laboratory testing should be considered.
2. Assessment of the extend at which the intermetallic phases of sigma (σ)-phase and chi (χ)-phase will affect stainless steel intergranular attack should be investigated separately for each of secondary phase contribution towards the brittle effect resulted from aged SAF2205 HAZ.
3. The effect of other phases such as nitrides (Cr_2N, CrN) should be further studied or assessed in order to understand their effect on the embrittlement characteristic of the welded duplex stainless steel, as they also contribute deterioration of corrosion resistance and mechanical properties of these material.

BIBLIOGRAPHY

[1] C., Örnek and D.,L., Engelberg, "T*owards understanding the effect of deformation mode on stress corrosion cracking susceptibility of grade 2205 duplex stainless steel*.," Materials Science and Engineering:A 66 (2016): 269-279.

[2] R., Gunn "*Duplex stainless steels: microstructure, properties and applications*", Cambridge England: Abington Publishing, 1997.

[3] O., A., Olaseinde, "*Comparative study of the effect of temperature on the corrosion behaviour of 2205 duplex stainless steel and 316 austenitic stainless steel in acidic chloride environment*", Advances in Materials Physics and Chemistry*,*Vol 32, p. 155*,* 2015.

[4] Z., Y., Liu, C., F., Dong, X., Li, G., Q., Zhi, and Y., F., Cheng, "S*tress corrosion cracking of 2205 duplex stainless steel in H_2S–CO_2 environment*", Springer, 14 June 2009.

[5] A., F., M. Perez, M., Breda, I., Calliari, G., Y., P., Medina and R., sandstrom, "*Detrimental Cr-rich phases precipitation on SAF2205 duplex stainless steels welds after heat treatment*", Sweden , 04 April 2016.

[6] K., Wang Chan and S., Chin Tjong, "*Effect of secondary phase precipitation on the corrosion behavior of duplex stainless steels*"Materials 2014, 7, 5268-5304; doi:10.3390/ma7075268, 22 July 2014

[7] R., H., Jones and R., E., Ricker, "Mechanisms of stress-corrosion cracking", Pacific Northwest National Laboratory and GT Engineering: *ASM International,* 1992.

[8] B., Messer, A.,Wright, V., Oprea "*Duplex stainless steel welding best practices*", Canada: Stainless steel world , Vol. 53, November 2007.

[9] I., H., Toor.,H., Daraghma, M., A., Samad, F., M., Abdallah and F., Patel "*Development of high Mn–N duplex stainless steel for automobile structural components*", Republic of Korea: Elsevier, Vol. 50, February 2008.

[10] D., P., Rowlands, "*The mechanical properties of stainless steel-How these are determined, and the factors which influence their values"*, Johannesburg: South Africa Stainless Steel-SASSDA- development association, *Stainless steel information,* p. 8.

[11] A., Vinoth, L., Jebaraj, C., R., Ajaykumar, K., V., Deepak and V., Aditya, *"Weldability, machinability and surfacing of commercial duplex stainless steel SAF2205 for marine applications*", Journal of advanced research, Vol. 8, Issue No.3, p. 183-199, 2017.

[12] J., Fourie and F., Robison, "*The influence of weld heat inputs on the mechanical and corrosion properties of duplex stainless steels*", *J. S. Afr. Inst. Min. Metall,* 1990.

[13] T., Prosek, T., Iverse, A., Taxén and C., Thierry, "Low-temperature stress corrosion cracking of stainless steels in the atmosphere in the presence of chloride deposit", Sweden: Corrosion. 2009;65(2):105-117, 2008.

[15] A., Hemaid, T., Tawfeek and O., A., Gaheen, "*An Investigation in to effect of butt welding parameters on weldment mechanical properties*", Cairo Egypt: American Journal of Mechanical Engineering, Vol. 4, p. 93-98, 2016.

[16] P., Paulraj and R., Garg, "*Effect of intermetallic phases on corrosion behaviour and mechanical properties of duplex stainless steels and super duplex stainless steel"*, Advances in science and technology research journal, Vol. 9, No. 27, p. 87-105, September 2015.

[17] R., Padilha, "*Stainless steel heat treatment metallurgy and technologies",* Boca Raton, Florida: Taylor and Francis Group, LLC, September 2006.

[18] G., R., Mohammed, M., Ishak, S., N., Aqida and H., A., Abdulhadid, *"Effects of heat input on microstructure, corrosion and mechanical characteristics of welded austenitic and duplex stainless steels*", Metals, 7(2), 39, 2016.

[19] R., Ding , Y., Yao, B.,Sun, G., Liu, J., He, T., Li, X., Wan, Z., Dai, D., Ponge, D., Raabe, C., Zhang, A., Godfrey, G., Miyamoto, T., Furuhara, Z., Yang , S., van der Zwaag and H., Chen, *"Chemical boundary engineering: A new route toward lean, ultra-strong yet ductile steels ",* Ding et al., Sci. Adv. 2020; 6 : eaay1430, 27 March 2020 .

[20] S., M., Khafagy, M., A., Morsy, F., M., Molleda and J.,C., Suarez, "*Heat treatment of Duplex stainless steel SAF2205 welded joints"*, Journal of American Science, p. 2-5, 2012.

[21] Z., Kubon, Š., Stejskalova and L., Kander, "*Effect of sigma phase on fracture behaviour of steels and weld Joints of components in power industry working at supercritical conditions*" Austenitic Stainless Steels: New Aspects, 63, December 2017.

[22] J., Sing and N., Goswami, "*Welding of Duplex stainless steel*," IJSRD-International Journal for Sientific research and Development, vol. 1, Issue No. 4, p. 920-923, 2013.

[23] T., Khuenkaew and K., Kanlayasiri, "*Resistance Spot Welding of SUS316L Austenitic/SUS425 ferritic stainless steels: weldment characteristics, Mechanical Properties, Phase Transformation and Solidification*", Bangkok, Thailand: Metals, 9, 710*,* 2019.

[24] A., V., Jebaraj, L., Ajaykumar, C., R., Deepak and K., V., V., Aditya, "Weldability, machinability and surfacing of commercial duplex stainless steel AISI2205 for marine applications," India: CrossMark, Vol. 8, Issue No. 3, p. 185-196, May 2017.

[25] S., Chaudhuri, "*Heat treatment of stainless steels*", Jamshedpur 831007, National metalurgical laboratory.

[26] A., D., Jones, *"Principles and prevention of corrosion"*, 2nd Edition, New Jersey: Prentice-Hall, Inc, 1996.

[27] H., S., Khatak, G., George, F., Schneider and K., Mummert, *" Stress corrosion crack growth studies on nitrogen added AISI type 316 stainless steel and its weld metal in boiling acidified sodium chloride solution using the fracture mechanics approach"*, Pangbourne & Canridge England: Woodhead Publishing Limited & Alpha Science International LTD, 2000.

[28] D., H., Kumar and A., S., Reddy, "*Study of mechanical behaviour in Austenitic stainless steel 316 LN welded joints*" International Journal of Mechanical Engineering and Robotics Research, 2013 IJMERR, Vol. 2, Issue No. 1, January 2013*.*

[29] A., Nen and H., Hanninnem, *“Chloride-induced stress corrosion cracking of powder metallurgy duplex stainless steels”*, Houston Taxes, USA: Corrosion Journal, Vol. 52, Issue No. 4, 1996.

[30] M., McGurie, *"Stainless steel for design engineers"*, Columbus, Ohio, USA: ASM International, 2008.

[31] R., K., Singh and W., H., Siew, *“Role of nitrite addition in chloride stress corrosion cracking of a super duplex stainless steel*”, Melbourne Australia: Elsevier, Corrosion Science Journal, Vol.52, Issue No.1, p. 113-117, 23 August 2009.

[32] A., F., Padilha and P., R., Rios," *Decomposition of Austenite in Austenitic Stainless Steels",* Brazi: ISIJ International, Vol. 42, No. 4, pp. 325–337, 18 January 2002.

[33] L., L., Shreir, G., T., Burstein and R., A., Jarman, *“Metal/environment reactions”*, London: Butterworth-Heinemann, Corrosion-Vol.1, 1994.

[34] H., Liou, R., Hsieh and W., Tsai, *“Microstructure and stress corrosion cracking in simulated heat-affected zones”*, Kaohsiung, Taiwan: Pergamon, Corrosion Science 44, 2841–285, 2002.

[35] SASSDA: South Africa Stainless Steel Development Association, *“Stainless steeels and corrosion information series*”, SAASDA, South Africa, 3 May 2016.

[36] J., Johansson, M., Oden and X., H., Zeng, *“Evolution of the residual stress state in a duplex stainless steel during loading*”, Journal - Acta materialia, Volume 47, Issue No. 9, P. 2669-2684, 9 July 1999.

[37] American iron and Steel Institute, “*Welding of stainless steels and other joining methods*”, Washington DC: American Iron and Steel Institute, *Designers' handbook series No. 9002*, p. 47, 1988.

[38] ASTM G39-99, "*Standard practice for preparation and use of bend-beam stress corrosion test specimens",* West Conshohocken: ASTM International, 2011.

[39] M., J., Povich, "*Low temperature sensitisation of type 304 stainless steel",* Corrosion - The Journal of Science and Engineering, Volume 34, Issue No. 2, p. 39-72, February 1978.

[40] ASTM 1237-20, "*Standard guide for installing bonded reistance strain gages",* West Conshohocken: ASTM international, 2014.

[42] ASTM E8/E8M-16a, "*Standard test methods for tension testing of metallic materials",* West Conshohocken: ASTM internaltional, 2016.

[43] J., Kospiczewicz, "*UNS S32205 material certificate No. 2016-305127", ArcelorMittal,* 2016.

[44] ASTM A484/ A484M - 20b, "*Standard specification for general requirements for stainless steel bars, Billets, and Forgings",* West Conshohocken: ASTM International .

[45] Casting SA, "*A special journal covering the technology, procedd and materials field for casting",* Brynston, South Africa, BA Crawford Specialised Publications (Pty) Ltd, Vol. 13, Series No. 6, April 2013.

[46] ASTM B117-18, "*Standard practice for operating salt spray (Fog) apparatus",* West Conshohocken: ASTM international, 2009.

[47] C., H., Simpson, C., J., Ray and B., S., Skerry, "*Accelerated corrosion testing of industrial maintenance paints using a cyclic corrosion weathering method*", Journal of Protective Coatings and Linings, Volume 8, Issue No. 5, p. 28-36, May 1991,

[48] B., S., Skerry, A., Alavi and K., I., Lindren, *"Environmental and electrochemical test methods for the evaluation of protective organic coatings*", Journal of Coatings Technology, Volume 60, Issue No. 765, pp 97-106, October 1988.

[49] ASTM G44-99, *"Standard practice for exposure of metals and alloys by alternate immersion in neutral 3.5% sodium chloride solution",* West Conshohocken: ASTM International, 2005.

[50] ASTM D1193-06, *"Standard specification for reagent water",* West Conshohocken: ASTM International, 2018.

[51] ASTM-*A262, "Standard practice for detecting susceptibilty to intergranular attack in Austenitic stainless steels",* West Conshohocken: ASTM International, 2019.

[52] G., Ali, "P*recipitation Study in a High Temperature Austenitic Stainless Steel using Low Voltage Energy Dispersive X-ray Spectroscopy*", Stockholm, Sweden, p. 83, 2012.

[53] A., Ul-Hamid, "*A beginners' guide to scanning electron microscopy",* Switzerland: Springer, 1st Edition, 2018.

[55] A. G30-97, "*Standard practice for making and using U-Bend stress- corrosion test specimens ",* West Conshohocken: ASTM International, 2016.

[56] W., Dutzel and A., Turnbull, "S*tress Corrosion Cracking-Fracture of materials from Nano to Macro*", GKSS, Geesthacht, Germany and National Physical Laboratory, Teddington, UK: Elsevier, ISBN 978-0-0804-3749-4, Vol. 11, pp. 43-74, 2007.

[57] ASTM D1141, "*Standard practice for the preparation of substitute ocean water",* West Conshohocken: ASTM International, 2013.

[58] ASTM E92-17, "*Standard test method for Vickers hardness and Knoop hardness of metallic materilas",* West Conshohocken: ASTM International, 2017.

[59] J., Goldstein, D., E., Newbury, D., C., Joy, C., E., Lyman, P., Echlin, E., Lifshin, L., Sawyer and J., R, Michael**,** *"Scanning Electron Microscopy and X-Ray Microanalysis",* Springer, Third Edition, 2003.

[60] S., Wessman, A., Wilson, S., Hertzman and R., Pettersson, *"An experimental and theoretical evaluation of microstructure coarsening in duplex stainless steels*", Steel Research International, 84(11), 1126-1137, 2013.

[61] R., K., S., Raman, *"Interplay of microbiological corrosion and alloy microstructure in stress corrosion cracking of weldments of advanced stainless steels*", Journal - Sadhana, 28(3-4), 467-473, 2003.

[62] H., Y., Liou, W., T.,Tsai, Y. , T., Pan, and R., I., Hsieh, "*Effects of alloying elements on the mechanical properties and corrosion behaviours of 2205 duplex stainless steels*", Journal of materials engineering and performance, Vol.10, Issue No.2, p. 231-241, 2001.

[63] Y., Jing, S., Wang, Y., Chen, M., Bao and I., Liu *"Effect of corrosion product films induced by tensile stress on P110 casing steels induced in CO_2 Environment*" Sichuan, China: Int. J. Electro-chem. Sci, Vol. 13, p. 7629-7642, 5 July 2018.

[68] ASTM E3-11, *"Standard guide for preparation of metallographic specimens"*, West Conshohocken: ASTM International, 2001.

[70] ASTM A240, *"Standard specification for chromium and chromium-nickel stainless steel plate, sheet, and strip for pressure vessels and for general application",* West Conshohocken: ASTM International, 2018.

[71] ASTM A923, *"Standard test methods for detecting detrimental intermetallic phase in Duplex Austenitic/Ferritic Stainless Steels",* West Conshohocken: ASTM International, 2014.

[72] L., Lorca-Isern, N., López-Luque, H., López-Jiménez, I., and M., V., Biezma, "*Identification of sigma and chi phases in duplex stainless steels",* Elsevier, Materials Characterization, 112, 20-29, 2016.

CHAPTER 7

Appendixes A- Calculations

a) Holder span (H) calculations at measured strain (ε) of AISI304: 1249-1250$\mu strain$ and SAF2205: 2250$\mu strain$

Table 19: AISI304 and SAF2205 Holder span (H) measurement

AISI304	SAF2205
$H_{measured} = L - H_{Exp}$ equation 13 Where: Specimen length (L) = $250mm$ Difference between L and distance between both ends of the specimen (H_{Exp}) after bended to produce measured strain (ε) = $2mm$ and $6mm$ for both AISI304 and SAF2205 respectively.	
$H_{AISI304} = 250mm - 2mm$ $H_{AISI304} = 248mm$	$H_{SAF2205} = 250mm - 6mm$ $H_{SAF2205} = 244mm$

b) According to ASTM G39, the relationship between length and holder specimen is given by $\left(\frac{L-H}{H}\right)$, where; L: Specimen length and H: Holder span measurement

$$0.01 \leq \frac{L - H}{H} \leq 0.50 \qquad \text{Equation 14}$$

$For\ AISI304: (\ 250mm - 248mm)/248mm = 0.01$
$For\ SAF2205: (\ 250mm - 244mm)/244mm = 0.02$

APPENDIXES B – DRAWINGS

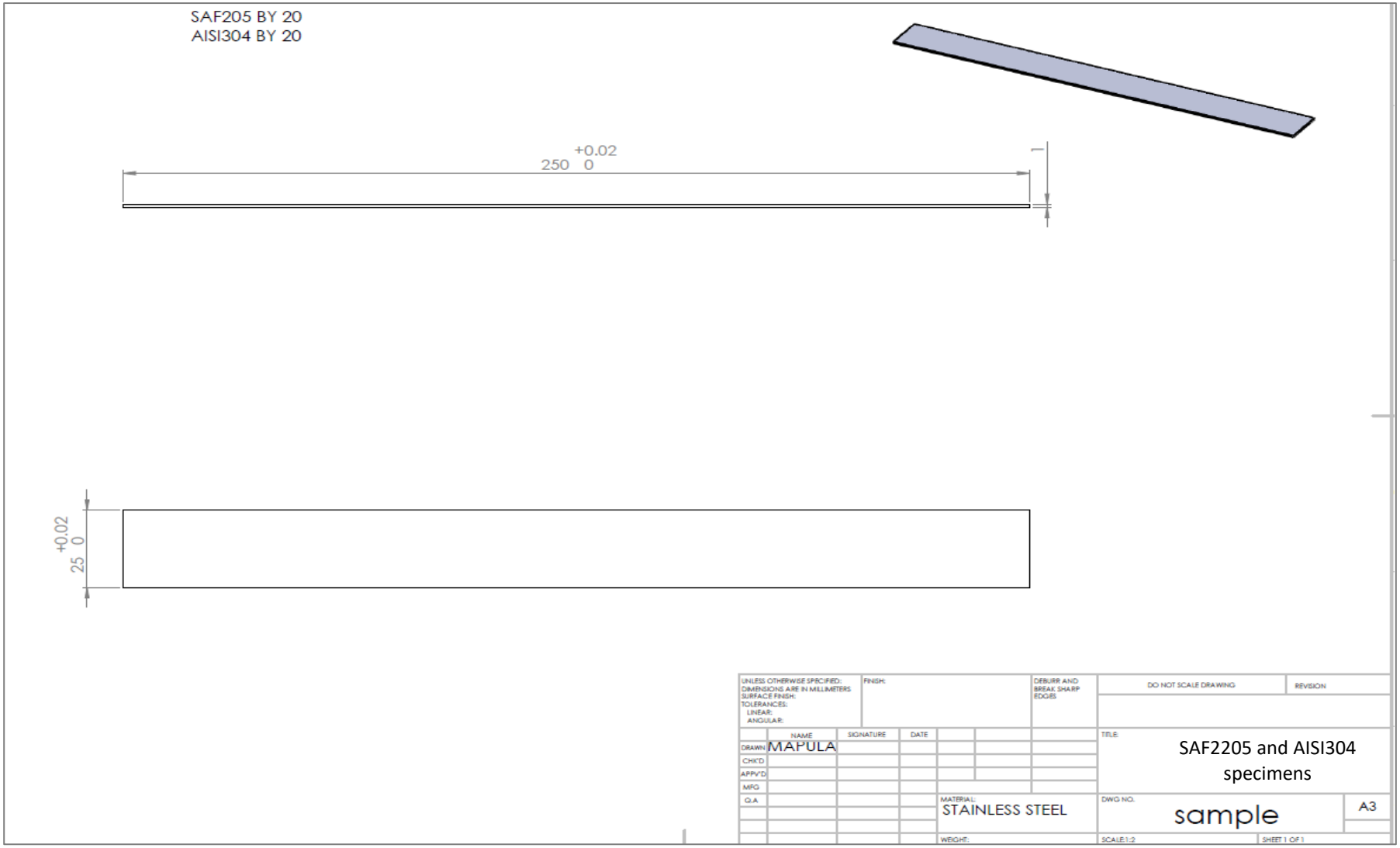

Figure 7-1: AISI304 and SAF2205 specimen geometry for cyclic corrosion test

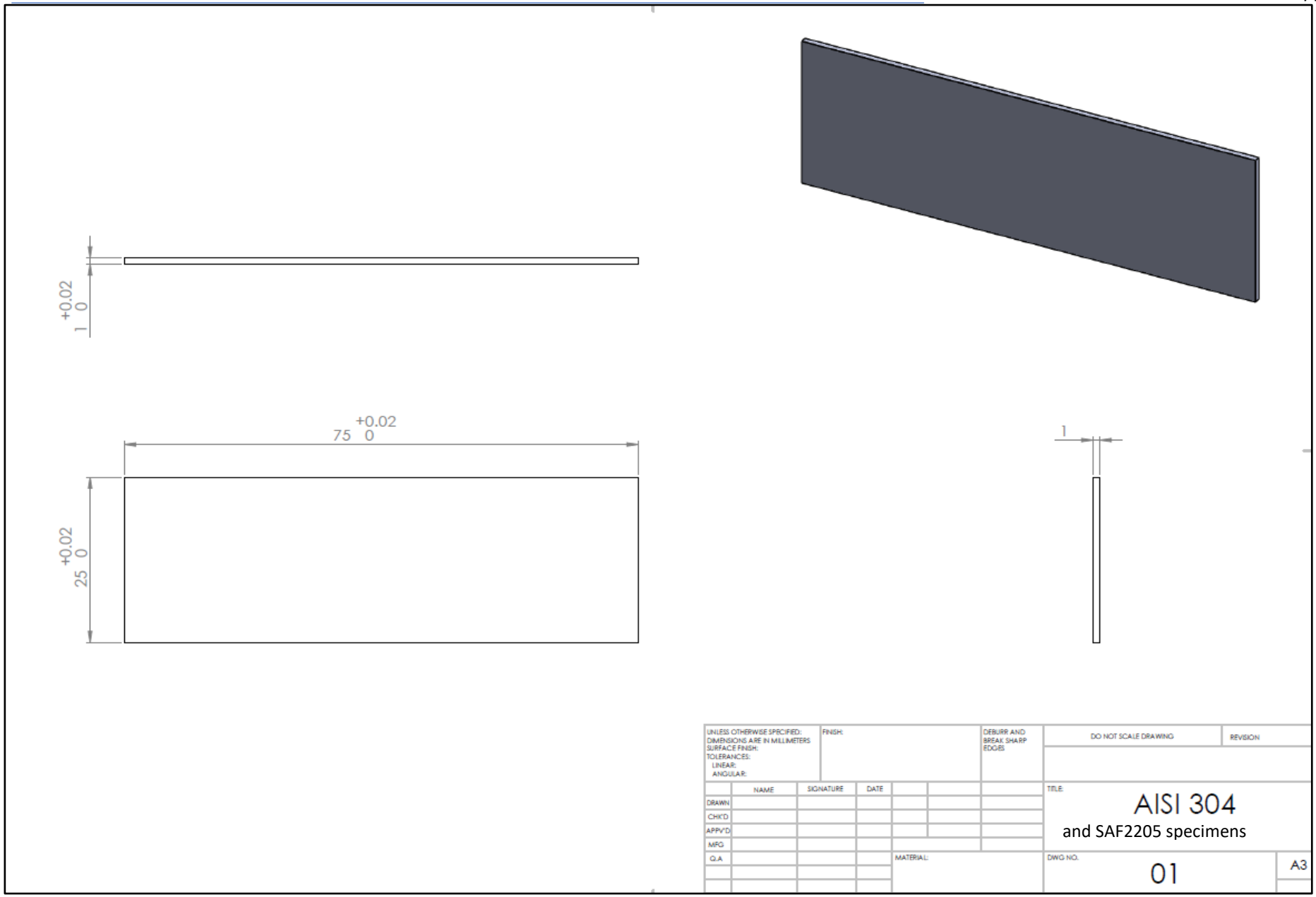

Figure 7-2: AISI304 and SAF2205 specimen geometry for intergranular attack testing

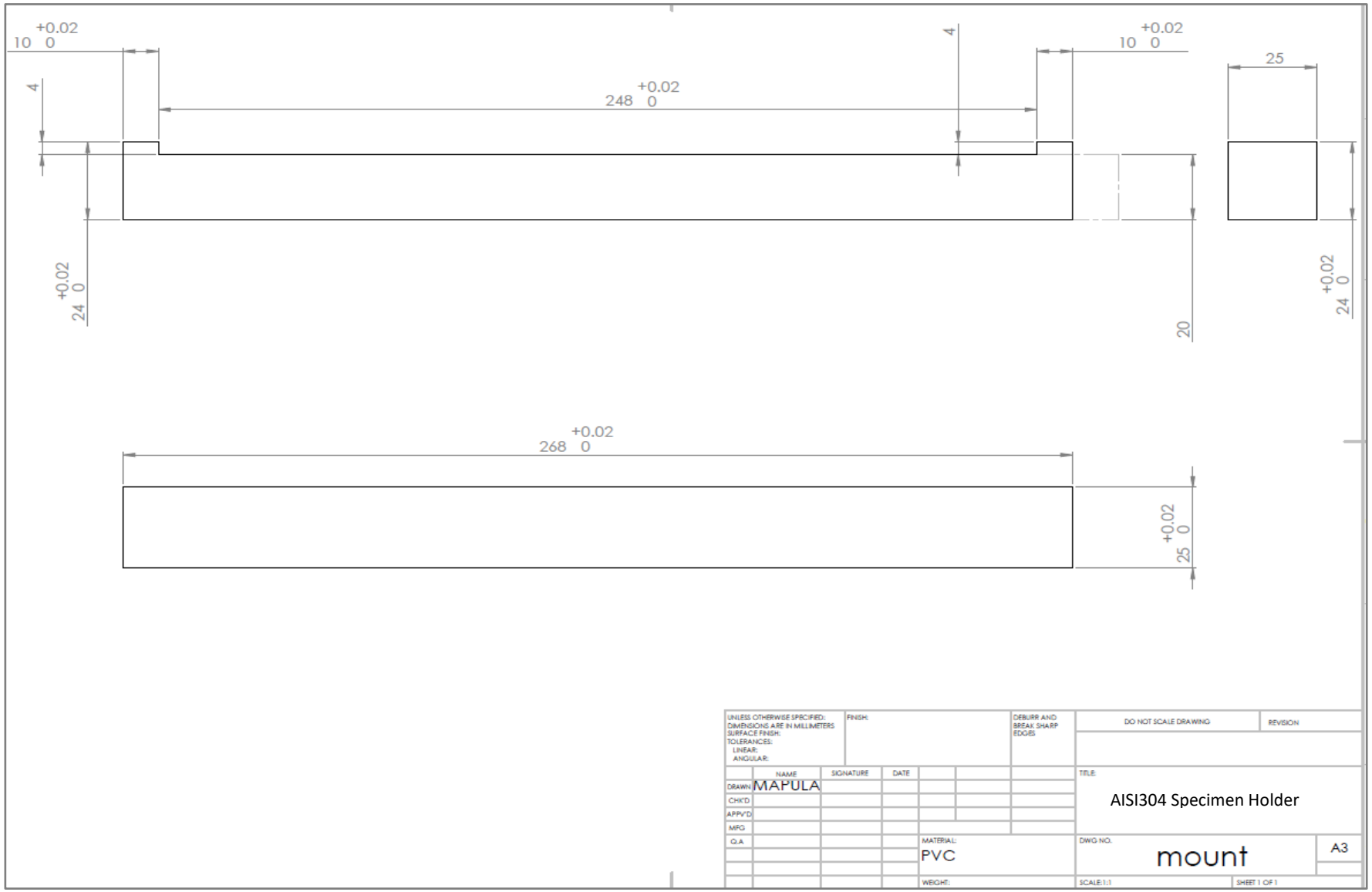

Figure 7-3:Two-point load specimen holder drawing for AISI304

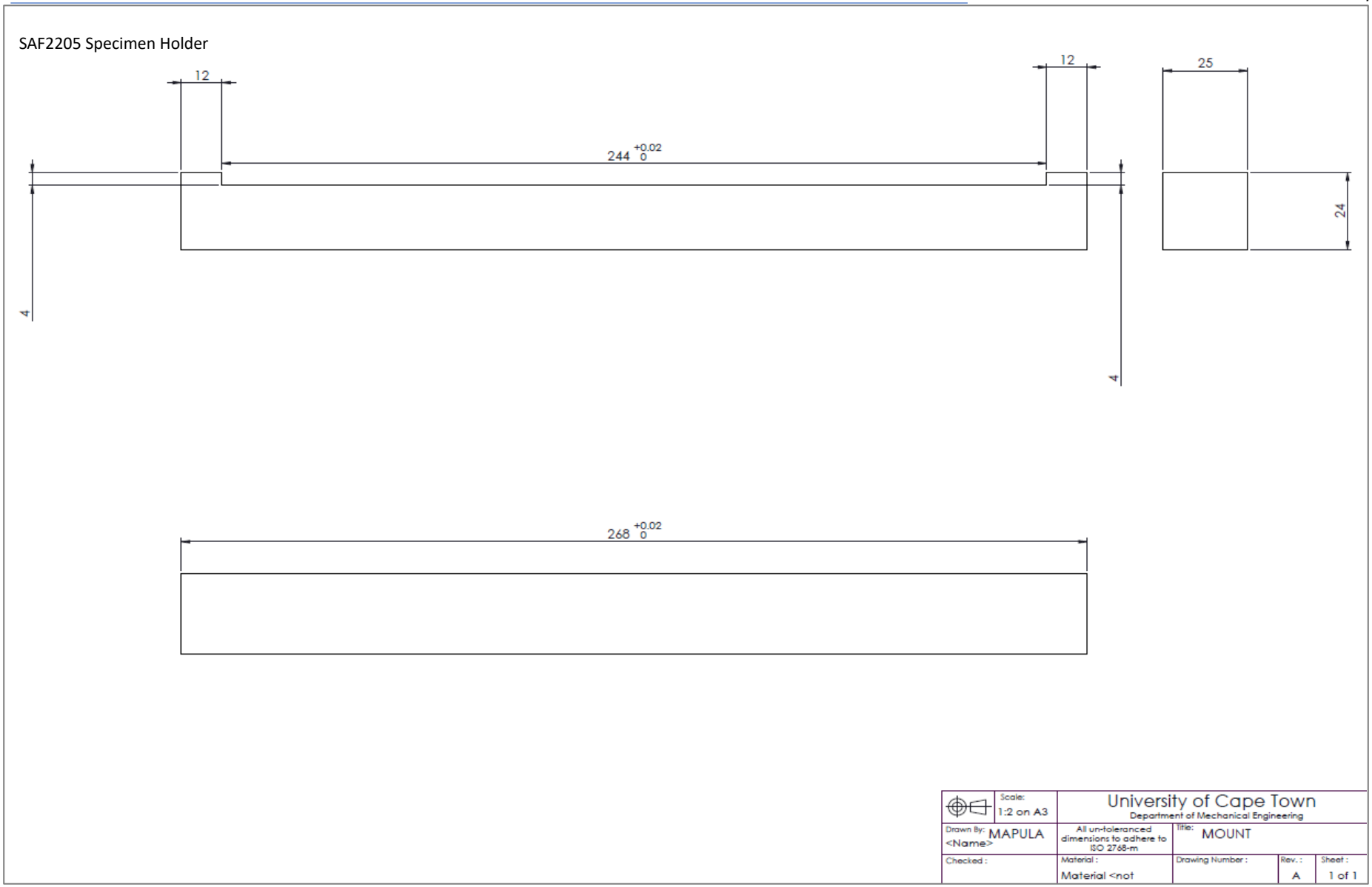

Figure 7-4: Geometry for SAF2205 bent-beam specimen holder

.

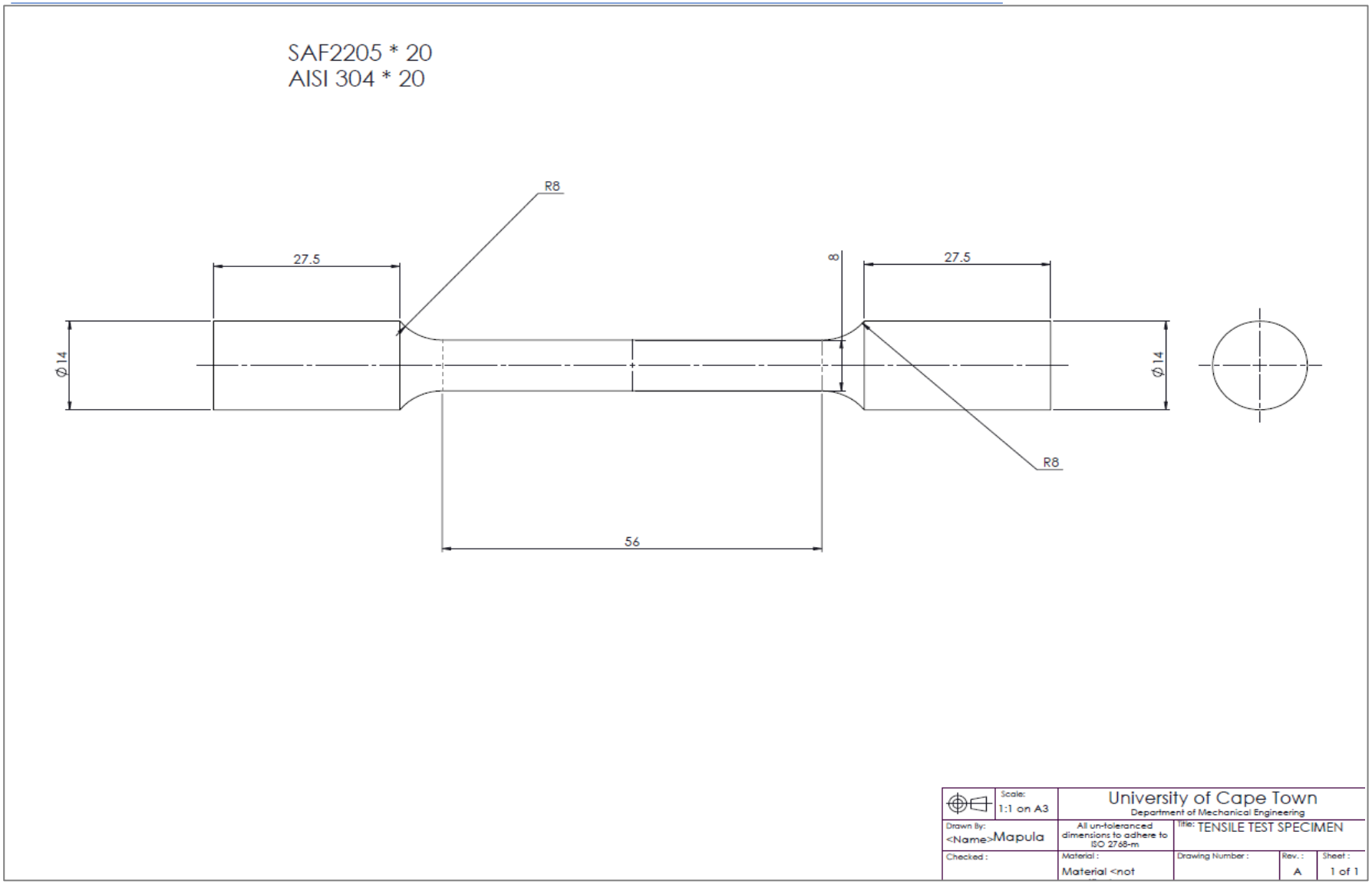

Figure 7-5: Tensile test specimen for AISI304 and SAF2205

APPENDIXES C – MECHANICAL PROPERTIES

1. SAF2205 mechanical properties test certificate from OEM (ArcelorMittal) [43]

Client - Purchaser - Besteller: WEUSTHOFF TRADING (PTY) LTD
2016-305127 Seite 007
Référence client - Purchase order - Kaufauftrag: WSA 9356/
Projet - Project - Projekt
INDUSTEEL France
Site : Le Creusot 56 RUE CLEMENCEAU 71200 LE CREUSOT
ArcelorMittal
Produit - Product - Erzeugnis
Commande / Poste - Internal order - Werksbestellung
Plate(s)
Bordereau de livraison - Delivery note - Lieferungsdokument
1316799 / 000060
83082542

072 ESSAIS MECANIQUES - MECHANICAL TESTS - MECHANISCHE PRÜFUNGEN

URETE SUR COUPON - HARDNESS ON SAMPLE - HÄRTE AUF COUPON

DURETE BRINELL 10
Test description - Prüfbeschreibung

N° lot QM	Etat	Loc	Epr.	T°	Uni	Mac	Uni	HB10 Ind Brinell	HB10 Ind Brinell	HB10 Ind Brinell	HB10 Aver Brinell
							Min				
							Max				270
885639.11-P.RI	000	PRI	PSS	20	°C	001		223	223	217	221

andard ASTM A240/M / ASME SA-240/M
strument M12 LEON BOLLEE

ICTION A L' AMBIANTE - ROOM TEMPERATURE TENSILE TEST - ZUGVERSUCH BEI RT

TRACTION CYLINDRIQUE
Test description - Prüfbeschreibung

lot QM	Etat	Loc	Epr.	T°	Uni	Mac	Uni	Rp 0,2% N/mm2	Rm N/mm2	A Lo=2" %
							Min	450	620	25
							Max			
885639.11-P.RI	000	PRI	1/2ST	20	°C	001		581	745	36

andard ASTM A240/M / ASME SA-240/M

Figure 6: SAF2205 Material Test Certification showing the hardness and tensile tests as supplied by ArcelorMittal

Table C-1.1: Summary of SAF2205 tensile test data, extracted from Material Test Cert. in Figure 57

Room temperature tensile test summarised data from Material Test Cert.		
Units	**Yield strength 0.2% MPa**	**Tensile strength MPa**
Min	450	620
Max	581	745

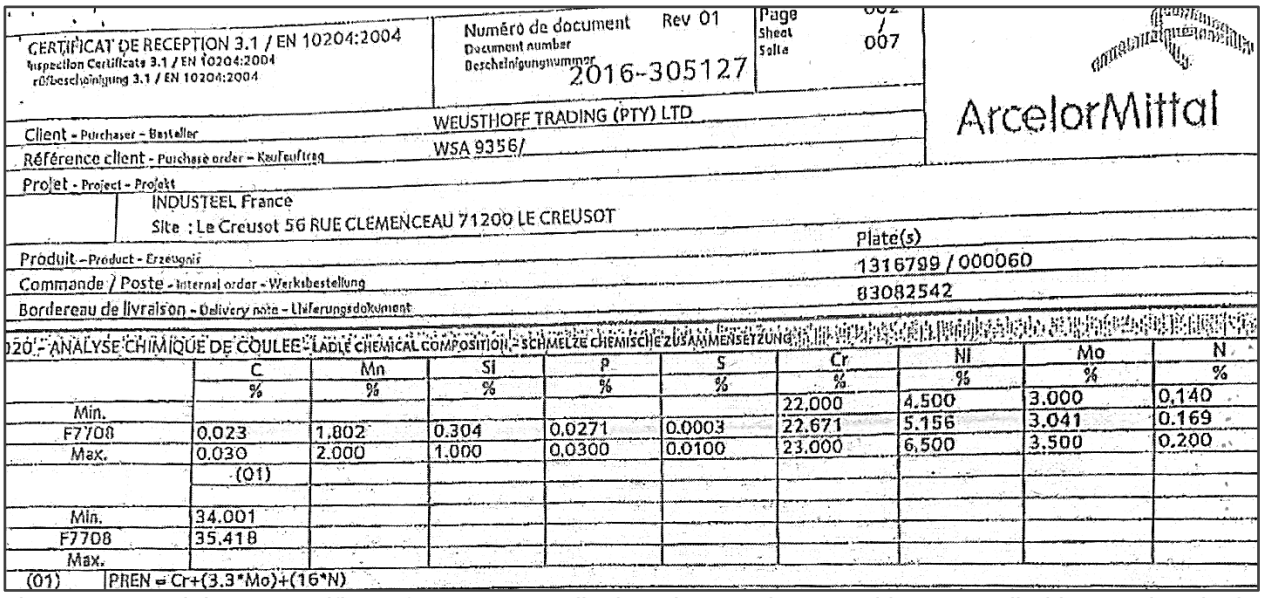

CERTIFICAT DE RECEPTION 3.1 / EN 10204:2004
Inspection Certificate 3.1 / EN 10204:2004
Abnahmeprüfzeugnis 3.1 / EN 10204:2004

Numéro de document / Document number / Bescheinigungsnummer: 2016-305127 Rev 01
Page / Sheet / Seite: 007

ArcelorMittal

Client - Purchaser - Besteller: WEUSTHOFF TRADING (PTY) LTD
Référence client - Purchase order - Kaufauftrag: WSA 9356/
Projet - Project - Projekt: INDUSTEEL France
Site : Le Creusot 56 RUE CLEMENCEAU 71200 LE CREUSOT
Produit - Product - Erzeugnis: Plate(s)
Commande / Poste - Internal order - Werksbestellung: 1316799 / 000060
Bordereau de livraison - Delivery note - Lieferungsdokument: 83082542

020 - ANALYSE CHIMIQUE DE COULEE - LADLE CHEMICAL COMPOSITION - SCHMELZE CHEMISCHE ZUSAMMENSETZUNG

	C %	Mn %	Si %	P %	S %	Cr %	Ni %	Mo %	N %
Min.						22.000	4.500	3.000	0.140
F7708	0.023	1.802	0.304	0.0271	0.0003	22.671	5.156	3.041	0.169
Max.	0.030	2.000	1.000	0.0300	0.0100	23.000	6.500	3.500	0.200
	(01)								
Min.	34.001								
F7708	35.418								
Max.									

(01) PREN = Cr+(3.3*Mo)+(16*N)

Figure 7: Material Test Certificate for SAF2205 alloying elemental compositions, supplied by ArcelorMittal

Table C-1.2:SAF2205 Alloying elements compositions extracted from Material Test Cert. (Figure 58) supplied by ArcelorMittal

SAF2205 Alloying elements	**C (wt.%)**	**Mn (wt.%)**	**Si (wt.%)**	**P (wt.%)**	**S (wt.%)**	**Cr (wt.%)**	**Ni (wt.%)**	**Mo (wt.%)**	**N (wt.%)**
Min.						22.00	4.50	3.00	0.14
F7708	0.02	1.80	0.30	0.02	0.01	22.67	5.15	3.04	0.17
Max	0.03	2.00	1.00	0.03	0.01	23.00	6.50	3.50	0.20
PREN =Cr+(3.3*Mo) + (16N)									
Min	34.00								
F7708	35.42								

2. Material mechanical properties of Austenitic stainless steel-AISI304L and AISI304

Table C-2.1: AISI304 Mechanical properties at room temperature **[27]**

Grade AISI	**Yield strength (YS) (MPa)**	**Tensile strength (UTS) (MPa)**	**Elongation El%**	**Hardness Vickers**
304L	215	470-670	45	129
304	≥205	≥515	≥40	129

APPENDIXES D: COMPOSITION RANGE OF DUPLEX PHASE (γ AND δ)

1. The range of Cr-element compositions in SAF2205 austenitic (γ)-phase

	wt.%Cr in austenite phase			
	F.O.V-1	**F.O.V-2**	**F.O.V-3**	**F.O.V-4**
	21,53	21,46	21,82	22,11
	21,77	21,53	21,85	22,02
	21,78	21,77	22,05	21,77
	21,84	21,78	22,18	21,85
	21,59	21,84	22,06	21,91
	21,45	21,59	22,17	21,74
	21,45	21,45	21,88	
	21,81	21,45	21,91	
	21,78	21,81	21,68	
		21,78	21,67	
			21,69	
			21,64	
Sample size (n)	9	10	12	6
Sample mean	21,67	21,65	21,88	21,90
Std. Dev	0,16	0,16	0,20	0,14
Confidence coefficient	0,95	0,95	0,95	0,95
Significance level	0,05	0,05	0,05	0,05
Margin of error	0,051	0,047	0,053	0,056
Point estimate	21,67	21,65	21,88	21,90
Lower limit	21,62	21,60	21,83	21,84
Upper limit	21,72	21,69	21,94	21,96

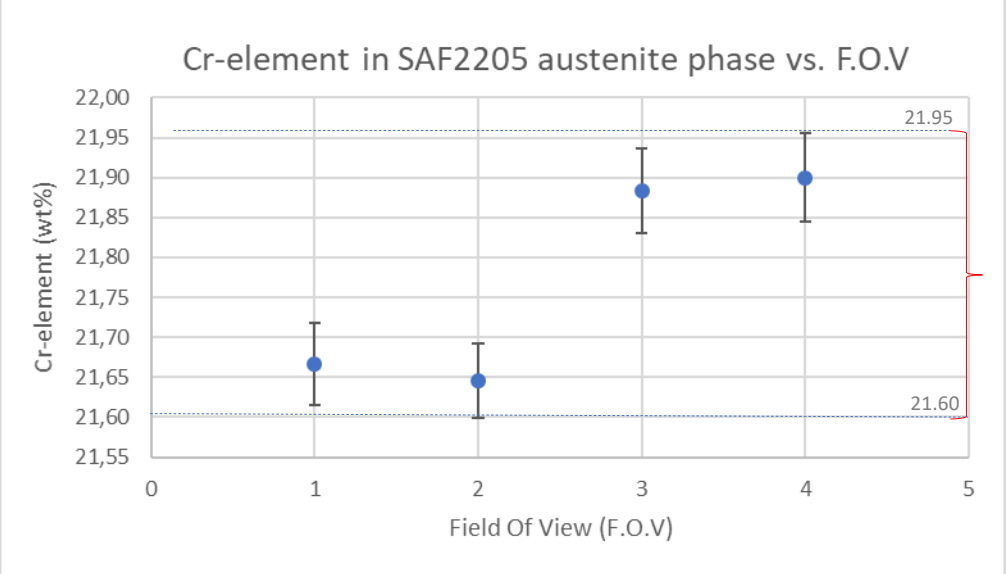

2. The range of Ni-element compositions in SAF2205 austenitic (γ)-phase

	wt.%Ni in austenite phase			
	F.O.V-1	**F.O.V-2**	**F.O.V-3**	**F.O.V-4**
	6,52	6,65	6,5	6,31
	6,57	6,57	6,43	6,28
	6,68	6,65	6,57	6,55
	6,51	6,63	6,41	6,54
	6,74	6,75	6,34	6,6
	6,74	6,6	6,35	6,56
	6,68	6,59	6,37	
	6,72	6,69	6,56	
		6,47	6,51	
		6,52	6,52	
			6,52	
			6,22	
Sample size (n)	8	10	12	6
Sample mean	6,65	6,61	6,44	6,47
Std. Dev	0,10	0,08	0,11	0,14
Confidence coefficient	0,95	0,95	0,95	0,95
Significance level	0,05	0,05	0,05	0,05
Margin of error	0,03	0,02	0,03	0,05
Point estimate	6,65	6,61	6,44	6,47
Lower limit	6,61	6,59	6,41	6,42
Upper limit	6,68	6,64	6,47	6,53

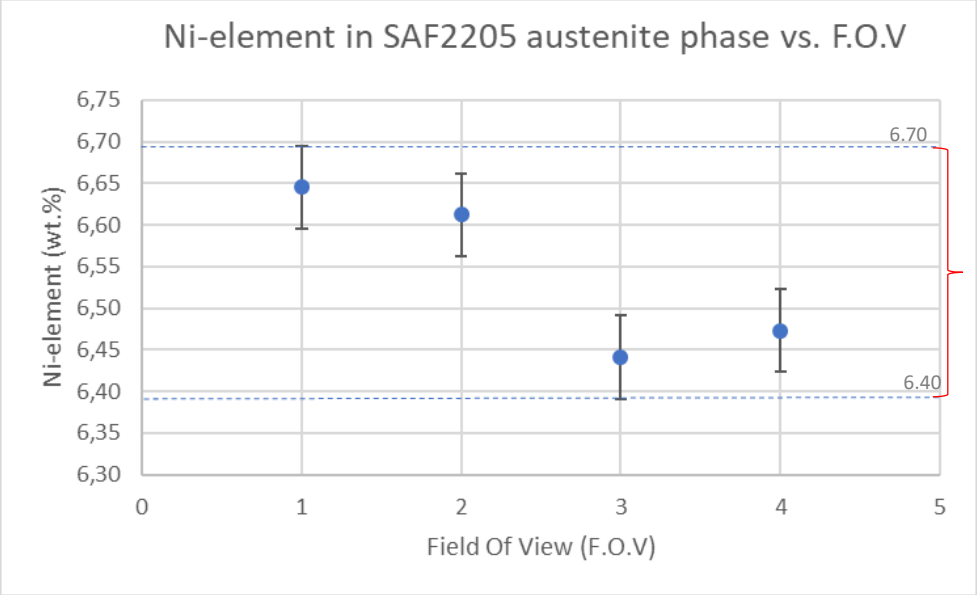

3. The range of Mo-element compositions in SAF2205 austenitic (γ)-phase

	wt.%Mo in austenite phase			
	F.O.V-1	**F.O.V-2**	**F.O.V-3**	**F.O.V-4**
	2,74	2,68	2,75	2,72
	2,73	2,6	2,81	2,79
	5,64	2,71	2,78	2,78
	2,77	2,69	2,72	2,81
	2,72	2,66	2,78	2,78
	2,67	2,68	2,72	2,82
	2,65	2,7	2,68	
	2,7	2,64	2,57	
		2,74	2,88	
		2,82	2,76	
			2,76	
			2,77	
Sample size (n)	8	10	12	6
Sample mean	3,08	2,69	2,75	2,78
Std. Dev	1,04	0,06	0,08	0,04
Confidence coefficient	0,95	0,95	0,95	0,95
Significance level	0,05	0,05	0,05	0,05
Margin of error	0,35	0,02	0,02	0,01
Point estimate	3,08	2,69	2,75	2,78
Lower limit	2,73	2,67	2,73	2,77
Upper limit	3,43	2,71	2,77	2,80

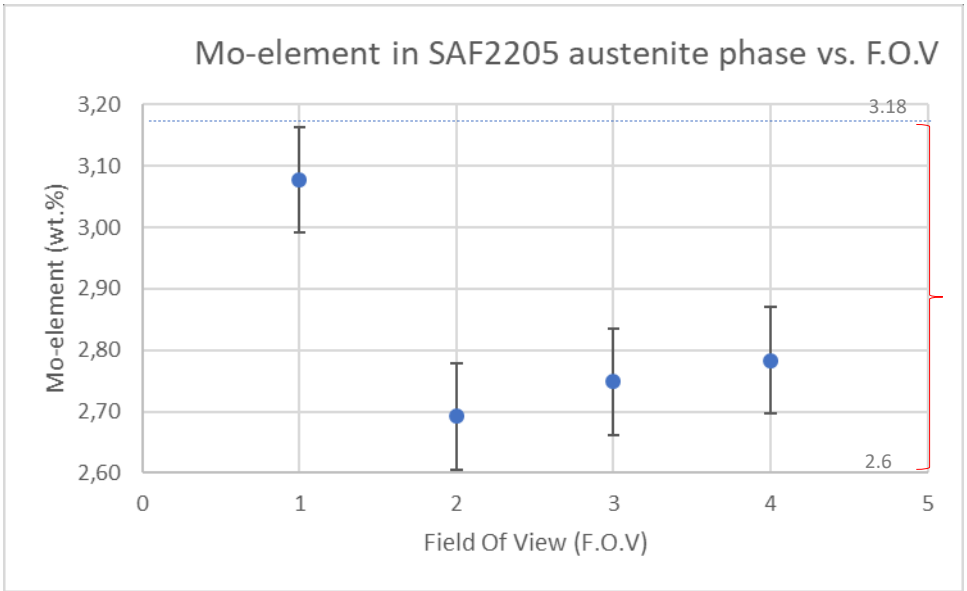

4. The range of Mn-element compositions in SAF2205 austenitic (γ)-phase

	wt.%Mn in austenite phase			
	F.O.V-1	**F.O.V-2**	**F.O.V-3**	**F.O.V-4**
	2,04	1,95	2,02	1,97
	1,95	2,1	2,1	2,08
	2,03	1,96	1,95	2,11
	2,06	2,03	2,03	2,12
	1,95	2,08	2,07	1,94
	2,06	2,07	2	2,07
	2,14	2,15	1,12	
	2,06	2,14	2,05	
		2,06	2,03	
		2	2,09	
			1,99	
			2,09	
Sample size (n)	8	10	12	6
Sample mean	2,04	2,05	1,96	2,05
Std. Dev	0,06	0,07	0,27	0,08
Confidence coefficient	0,95	0,95	0,95	0,95
Significance level	0,05	0,05	0,05	0,05
Margin of error	0,02	0,02	0,07	0,03
Point estimate	2,04	2,05	1,96	2,05
Lower limit	2,02	2,03	1,89	2,02
Upper limit	2,06	2,07	2,04	2,08

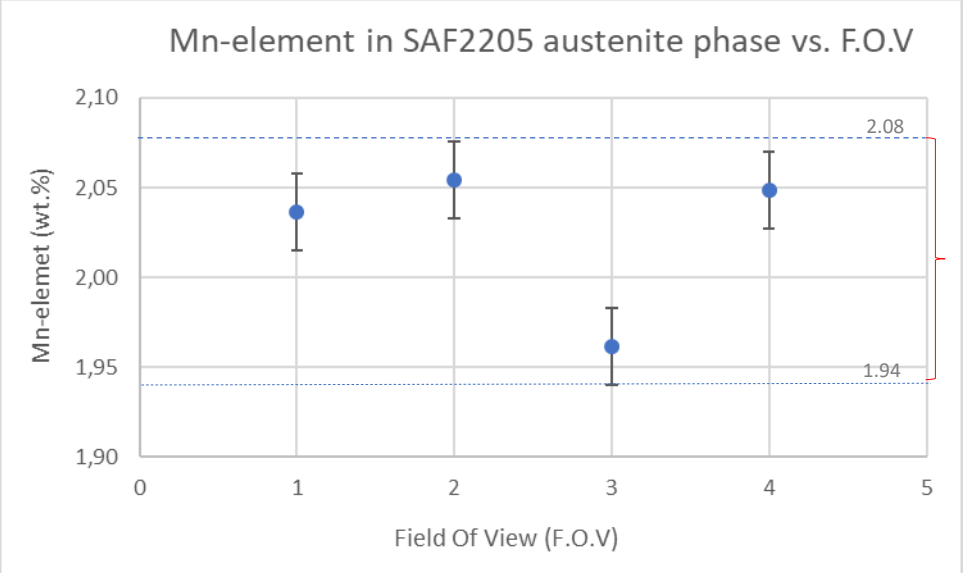

5. The range of Cr-element compositions in SAF2205 ferrite (δ)-phase

	wt.%Cr in ferrite phase			
	F.O.V-1	**F.O.V-2**	**F.O.V-3**	**F.O.V-4**
	24,48	24,36	24,32	24,56
	24,42	24,45	24,3	24,43
	24,29	24,41	24,47	24,62
	24,42	24,27	24,42	24,73
	24,49	24,45	24,2	25,15
	24,41	24,49	24,29	
		24,43	24,17	
		24,43	24,36	
		24,31	24,26	
		24,49	24,18	
		24,23	24,25	
			24,41	
Sample size (n)	6	11	12	5
Sample mean	24,42	24,39	24,30	24,70
Std. Dev	0,07	0,09	0,10	0,27
Confidence coefficient	0,95	0,95	0,95	0,95
Significance level	0,05	0,05	0,05	0,05
Margin of error	0,03	0,03	0,03	0,12
Point estimate	24,42	24,39	24,30	24,70
Lower limit	24,39	24,37	24,28	24,58
Upper limit	24,45	24,42	24,33	24,81

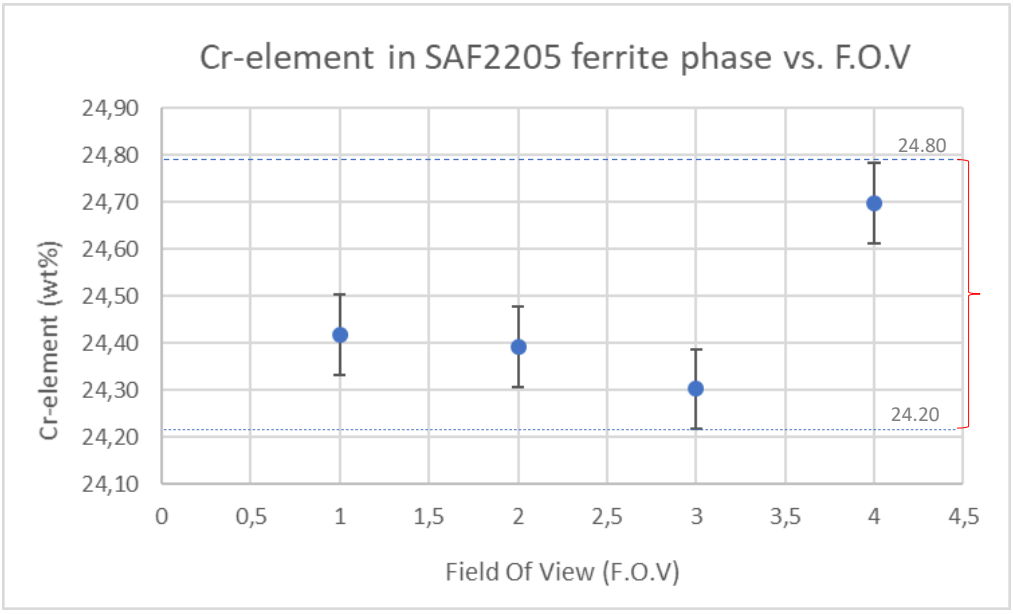

6. The range of Ni-element compositions in SAF2205 ferrite (δ)-phase

	wt.%Ni in ferrite phase			
	F.O.V-1	**F.O.V-2**	**F.O.V-3**	**F.O.V-4**
	4,47	4,46	4,43	4,42
	4,37	4,67	4,44	4,34
	4,59	4,44	4,45	4,21
	4,5	4,62	4,4	4,17
	4,39	4,36	4,54	3,9
	4,52	4,42	4,43	
		4,51	4,52	
		4,36	4,5	
		4,5	4,39	
		4,37	4,39	
		4,55	4,39	
			4,42	
			4,48	
Sample size (n)	6	11	13	5
Sample mean	4,47	4,48	4,44	4,21
Std. Dev	0,08	0,10	0,05	0,20
Confidence coefficient	0,95	0,95	0,95	0,95
Significance level	0,05	0,05	0,05	0,05
Margin of error	0,03	0,03	0,01	0,08
Point estimate	4,47	4,48	4,44	4,21
Lower limit	4,44	4,45	4,43	4,12
Upper limit	4,44	4,45	4,43	4,12

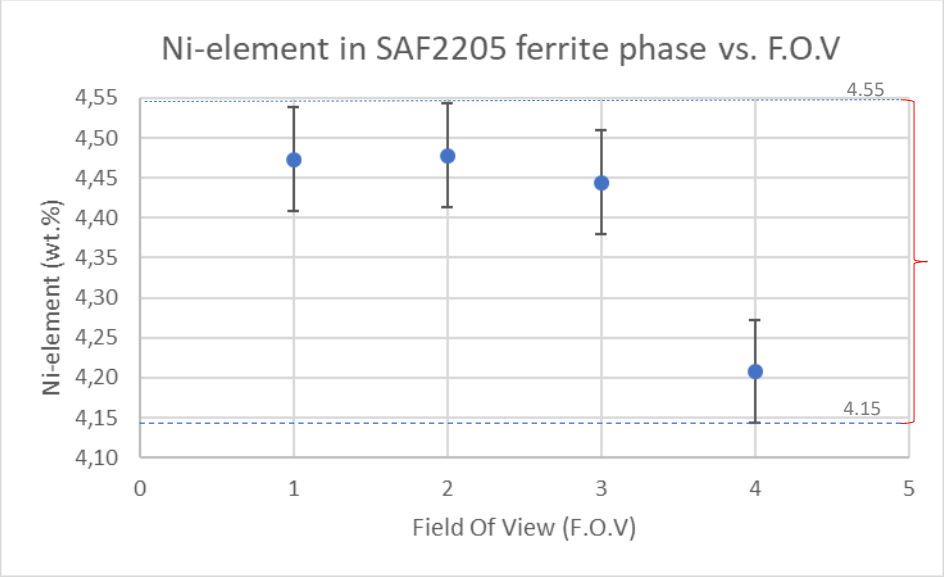

7. The range of Mo-element compositions in SAF2205 ferrite (δ)-phase

	wt.%Mo in ferrite phase			
	F.O.V-1	**F.O.V-2**	**F.O.V-3**	**F.O.V-4**
	4,32	4,24	4,22	4,19
	4,32	4,13	4,32	4,42
	4,14	4,42	4,25	4,44
	4,23	4,05	4,26	4,29
	4,08	4,24	4,27	
	4,4	4,24	4,19	
		4,11	4,22	
		4,35	4,15	
		4,32	4,37	
		4,11	4,3	
		4,13	4,37	
			4,25	
Sample size (n)	6	11	12	4
Sample mean	4,25	4,21	4,26	4,34
Std. Dev	0,12	0,12	0,07	0,12
Confidence coefficient	0,95	0,95	0,95	0,95
Significance level	0,05	0,05	0,05	0,05
Margin of error	0,05	0,03	0,02	0,06
Point estimate	4,25	4,21	4,26	4,34
Lower limit	4,20	4,18	4,25	4,28
Upper limit	4,30	4,25	4,28	4,39

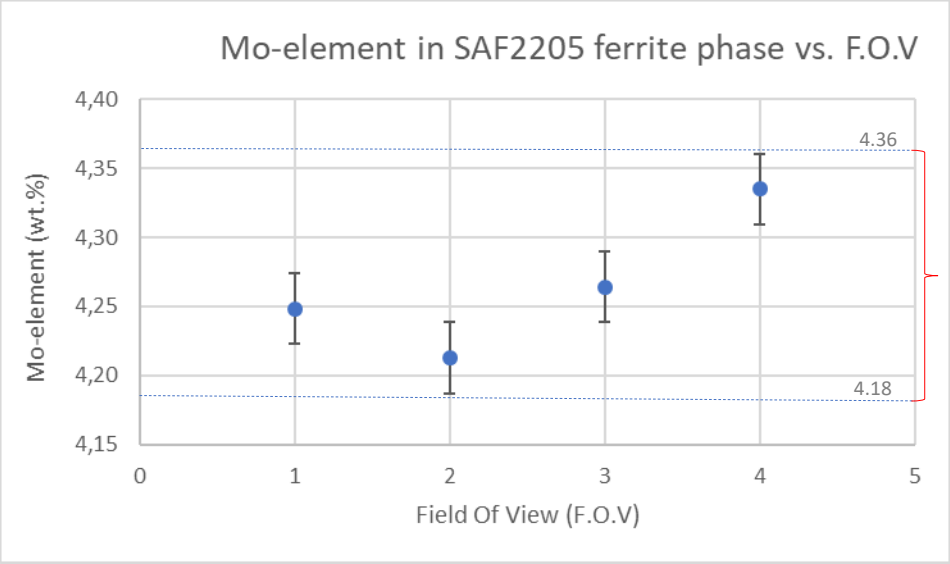

8. The range of Mn-element compositions in SAF2205 ferrite (δ)-phase

	wt.Mn in ferrite phase			
	F.O.V-1	**F.O.V-2**	**F.O.V-3**	**F.O.V-4**
	1,81	1,79	1,83	1,74
	1,79	1,81	1,81	1,83
	1,75	1,77	1,87	1,85
	1,77	1,76	1,76	1,77
	1,73	1,76	1,84	1,85
	1,74	1,75	1,77	
		1,88	1,8	
		1,74	1,79	
		1,72	1,84	
		1,79	1,85	
		1,82	1,87	
			1,73	
Sample size (n)	6	11	12	5
Sample mean	1,77	1,78	1,81	1,81
Std. Dev	0,03	0,04	0,04	0,05
Confidence coefficient	0,95	0,95	0,95	0,95
Significance level	0,05	0,05	0,05	0,05
Margin of error	0,01	0,01	0,01	0,02
Point estimate	1,77	1,78	1,81	1,81
Lower limit	1,75	1,77	1,80	1,79
Upper limit	1,78	1,79	1,83	1,83